Mode Locking in Systems of Globally-Coupled Phase Oscillators

vorgelegt von
M. Sc.
Richard Sebastian Eydam
ORCID: 0000-0001-6132-3055

von der Fakultät II - Mathematik und Naturwissenschaften
der Technischen Universität Berlin
zur Erlangung des akademischen Grades
- Dr.rer.nat. -
genehmigte Dissertation

Promotionsausschuss:
Vorsitzender: Prof. Dr. Stephan Reitzenstein
Gutachterin: Prof. Dr. Kathy Lüdge
Gutachter: Ass. Prof. Dr. Igor Franović
Gutachter: Dr. Matthias Wolfrum

Tag der wissenschaftlichen Aussprache: 12. Juni 2019

Berlin 2019

Abstract

In systems of globally coupled phase oscillators with sufficiently structured natural frequencies, a new type of collective behavior is discovered that exists below the synchronization threshold. The solution type is distinguished by the appearance of sharp pulses in the mean field amplitude which imply a temporary high coherence among the phases. This is similar to a process known in lasers called *mode locking* that refers to the formation of optical pulsed by the interaction through a nonlinear optical medium. General features of mode-locked solutions of coupled phase oscillators are identified and a classification of the different solution types is provided. The ability of phase oscillator systems to perform mode locking is investigated with respect to the interaction function, the system size and the realization of the natural frequencies. It was found that higher harmonics in the Fourier series of the interaction function play an influential role in the self-organization of mode-locked solutions. For the simple sinusoidal coupling of the Kuramoto model, self-organized mode locking could not be observed, though, mode-locked solutions are found that coexist with phase turbulence. The chaotic transients that precede mode locking are examined with respect to the interaction function and the system size revealing a supertransient behavior of type-II, i.e. average transient length grows exponentially with the system size. The stability and bifurcation scenarios of mode-locked solutions are studied, displaying an involved picture of the local stability and revealing intermittency as the typical route from mode locking to phase turbulence. Close to the stability boundaries of mode-locked solutions, low-dimensional chaotic attractors can be found that maintain the pulsed behavior with a jittering of the inter-pulse intervals and pulse heights. In large oscillator ensembles with a modal structure in the natural frequencies, mode-locked solutions generally arise in a two-stage process of inner-modal synchronization and inter-modal locking. Aside from the modal dynamics, which is covered by the introduced modal order parameters, the mode-locked solutions in large ensembles are found to share the characteristics regarding transient behavior and mean-field dynamics. The notion of mode locking is applied to intuitively explain the occurrence of coherence echoes that stem from the application of two consecutive stimuli to a population of oscillators. It is shown that with repetitive periodic stimulation, fully mode-locked states can be established that depend substantially on the interaction function. The non-monotonic behavior of the magnitude of the echoes is revealed and explained by the evolution of the modal order parameters for a synthetic, fully mode-locked initial state.

Abstract

In Systemen von global gekoppelten Phasenoszillatoren mit hinreichend regelmäßigen natürlichen Frequenzen existiert eine kollektive Dynamik unterhalb der Synchonisationsschwelle. Die Lösungen sind durch scharfe Pulse in der Amplitude des Mean-Fields ausgezeichnet, was auf eine ausgeprägte Phasenkohärenz hindeutet. Dies ähnelt dem Prozess der Modenkopplung aus der Laserphysik, bei dem es um die Entstehung von Lichtpulsen in nichtlineare optischen Materialien geht. Die Eigenschaften von modengekoppelten Lösungen werden diskutiert und eine Klassifikation der verschiedenen Typen wird angeführt. Das Vermögen Moden zu koppeln wird im Hinblick auf die Wechselwirkung, die Systemgröße sowie die natürlichen Frequenzen untersucht. Es zeigt sich, dass höhere Harmonische in der Fourier-Entwicklung der Wechselwirkung entscheidend zur Selbstorganisation beitragen. Für die einfache sinusförmige Kopplung des Kuramoto-Modells wurde selbstorganisierte Modenkoppelung nicht beobachtet, dennoch konnte gezeigt werden, dass die selbigen Lösungen mit Phasenturbulenz koexistieren. Die Eigenschaften von chaotischen Transienten werden eingehend untersucht, wobei sich ein exponentielles Wachstum der mittleren Transientendauern bezüglich der Systemgröße zeigt und die Transienten als Type-II-Supertransienten klassifiziert werden. Außerdem wird gezeigt, dass die relative Stärke der zweiten Harmonischen einen erheblichen Einfluss auf die Transientendauern ausübt. Die Stabilität und die Bifurkationen von modengekoppelten Lösungen werden untersucht, wobei sich ein kompliziertes Verhalten der lokalen Stabilität zeigt und Intermittenz als typischer Übergang zur Phasenturbulenz identifiziert werden kann. Des Weiteren finden sich an den Stabilitätsgrenzen chaotische Attraktoren, welche sich durch Pulsation mit variablen Pulsabständen und Pulshöhen auszeichnen. In großen Ensemblen mit modalen Frequenzverteilungen bilden sich modengekoppelte Lösungen in einem zweistufigen Prozess heraus, der aus der Synchronisation innerhalb der Moden und der anschließenden Modenkopplung besteht. Neben der Dynamik innerhalb der einzelnen Moden, welche durch die eingeführten modalen Orderparameter beschrieben wird, erhalten die Lösungen ihr Verhalten bezüglich der Dynamik des Mean-Fields und der Transienten bei. Modenkopplung wird zur intuitiven Erklärung von Kohärenz-Echos herangezogen, welche allgemein durch Stimulation hervorgerufen werden. Es wird gezeigt, dass die Amplituden der Echos in nicht-monotoner Form abkligen was anhand der modalen Orderparameter verstanden werden kann. Durch periodische Stimulation wird eine Verbindung von partieller zu vollständiger Modenkopplung aufgebaut, wobei der Einfluss verschiedener Stimulustypen diskutiert wird.

Acknowledgemets

I would like to thank all my colleagues from the Laser Dynamics research group at WIAS for their interest in my research and the inspiring atmosphere during our workshops and seminars.

In particular, I would like to thank Oleh Omel'chenko, Serhiy Yanchuk, Igor Franović, and Stefan Ruschel for listening, asking question, and for their help in manifold ways.

I would like to thank my scientific adviser Matthias Wolfrum from whom I learned constantly and who supported me in every regard.

For their patience, forbearance and support I would also like to thank my family and my friends.

I would like to acknowledge the funding from the DFG in Collaborative Research Center 910: "Control of self-organizing nonlinear systems: Theoretical methods and concepts of application."

Versicherung an Eides statt

Hiermit versichere ich, die hier vorgelegte Dissertation mit dem Titel: "Mode Locking in Systems of Globally-Coupled Phase Oscillators" eigenständig und ohne Zuhilfenahme anderer Quellen als der im Literaturverzeichnis angegebenen angefertigt zu haben. Die vorgelegte Arbeit wurde bisher noch nicht zur Erlangung eines Abschlusses an einer anderen Hochschule vorgelegt.

Berlin, den_____ Unterschrift:_____

Contents

1 Introduction **1**
1.1 Preamble 1
1.2 Thesis Overview 2

2 Background **7**
2.1 Models of Coupled Phase Oscillators 7
2.1.1 Synchronization and the Adler Equation 8
2.1.2 Weakly-Coupled Oscillators and Phase Reduction . . . 8
2.1.3 The Kuramoto Model 11
2.1.4 Daido's Extension of the Coupling Function 12
2.1.5 Extensive Chaos Below the Synchronization Threshold 14
2.2 Circle Maps Mode Locking and Resonances 14
2.2.1 Arnold Circle Map 15
2.2.2 Globally-Coupled Circle Maps 16
2.3 The Coherence Echo Phenomenon 18
2.3.1 Stimulation of Ensembles of Phase Oscillators 19
2.3.2 Coherence Echoes in Kuramoto-Type Systems 19
2.4 Numerical Methods 20
2.4.1 Simulations 20
2.4.2 Lyapunov Spectra 23

3 Phase Oscillator Mode Locking **27**
3.1 Phase Oscillators with Equidistant Frequencies 27
3.1.1 System and Solution Symmetries 29
3.1.2 Effective Frequencies and Effective Frequency Combs . 31
3.2 Prototype Mode-Locked Solution 31
3.3 Definitions of Mode-Locked Solutions 32
3.3.1 Equidistant Mode-Locked Solutions 32
3.3.2 Harmonic Mode-Locked Solutions 34
3.3.3 Subharmonic Mode-Locked Solutions 35
3.4 Self-Organization of Mode-Locked Solutions 36

3.4.1 Mode Locking in the Kuramoto Model with Equidistant Natural Frequencies . . . 36
3.4.2 Mode locking in the Kuramoto Model with Second Harmonic Interaction . . . 43
3.5 Bifurcations of Mode-Locked Solutions . . . 47
3.5.1 Chaotically-Modulated Solution Through Torus Breakdown . . . 50
3.5.2 Transition to Phase Turbulence Through Intermittency 54
3.5.3 Classification of Chaotic Transients . . . 56
3.6 Detuned Combs of Natural Frequencies . . . 60
3.6.1 Frequency Combs with Quenched Disorder . . . 60
3.6.2 Frequencies with Systematic Detuning . . . 63
3.7 Mode Locking in Large Ensembles . . . 67
3.7.1 Multimodal Frequency Distributions and Modal Order Parameters . . . 67
3.7.2 Self-Organization to Mode-Locked Solutions . . . 69
3.7.3 Stability with Respect to the Spectral Width . . . 70
3.7.4 Coexistence of Mode-Locked Solutions and Modal Turbulence . . . 72
3.8 Mode Locking in Optical Systems . . . 75
3.8.1 The Phase-Reduced Lugiato-Lefever Equation . . . 77
3.8.2 A Qualitative Comparison of the Mode-Locking Phenomena . . . 78

4 Coherence Echoes and Mode Locking 81
4.1 Phase Oscillators with Stimulation . . . 82
4.1.1 Transport Pattern Resulting from a Single Stimulus . . 83
4.1.2 Coherence Echoes Appearing After Two Stimuli . . . 84
4.2 Synthetic Mode-Locked Initial Conditions . . . 86
4.2.1 Non-Monotonously Decaying Echoes of the Synthetic Mode-Locked Initial Conditions . . . 91
4.2.2 Influence of the Global Coupling on the Synthetic Mode-Locked Initial Conditions . . . 94
4.3 Stimulated Mode-Locked Solutions . . . 95
4.3.1 Accumulation of a Stimulated Fully-Locked Mode Comb 95
4.3.2 Stimulated Mode Locking and Circle Maps . . . 96
4.3.3 Effect of the Global Interaction on Stimulated Mode-Locked States . . . 100

5 Discussion 103

List of Figures

1.1 Pulsed – Mode-locked solution in the Kuramoto model 2

2.1 Flow for the Adler equation 8
2.2 Synchronization transition in the Kuramoto model 12
2.3 Devil's staircase for the Arnold circle map 16
2.4 Globally-coupled circle maps with equidistant phase increments 18
2.5 Basic coherence echo phenomenon in the Kuramoto model . . 20

3.1 Comb of equidistant natural frequencies 28
3.2 Phase interaction function with two harmonics 29
3.3 Prototype mode-locked solution 32
3.4 Decay of the prototype solution with detuned frequencies . . . 33
3.5 Averaged coherence radius $\langle R_1(t)\rangle_T$ of the prototypical mode-locked solution 33
3.6 Preparation of initial conditions for mode locking 37
3.7 Three different types of solutions in the Kuramoto model with equidistant natural frequencies 38
3.8 Mode locking region for Kuramoto-type coupling and increasing system sizes 39
3.9 Equidistant mode-locked solution for Kuramoto-type (first harmonic) coupling 39
3.10 Subharmonic mode-locked solution in the Kuramoto model . . 41
3.11 Dynamical continuation of a subharmonic mode-locked solution in the Kuramoto model 42
3.12 Extensive Lyapunov spectra corresponding to phase turbulence 43
3.13 Coexistence of phase turbulence and mode locking 44
3.14 Average transient times in dependence of the second harmonic coupling 45
3.15 Rates of expansion of phase space volumes in the vicinity of mode-locked solutions 47
3.16 Rates of expansion in systems with larger numbers of oscillators 48

3.17 Dynamical continuation of solutions in the coupling strength . 49
3.18 Merging of effective frequencies at large coupling strength values 50
3.19 Emergence of an invariant torus and its breakdown 52
3.20 Attractor of a chaotically-modulated mode-locked solutions . . 53
3.21 Lyapunov spectrum of the chaotic mode-locked solutions . . . 53
3.22 Intermittency between mode locking and phase turbulence . . 55
3.23 Power-law scaling of the intermittent mode locking 55
3.24 Landscape of solutions for pairs of (K, γ) and $N = 21$ 56
3.25 Survey of the maximal Lyapunov exponent λ_1 for pairs of (K, γ) and $N = 21$ 57
3.26 Scaling of the average transient times with the number of oscillators N 58
3.27 Characterization of the chaotic transients preceding mode locking 59
3.28 Mode-locked solutions for large number of oscillators 59
3.29 Intermittent breakdown of mode locking by quenched disorder 61
3.30 Probability to achieve mode locking for different levels of quenched disorder 62
3.31 Probability to achieve mode locking in terms of the distance to the nearest equidistant frequency comb 64
3.32 Disjoint regions of stable mode locking for different levels of quenched disorder 64
3.33 Mode-locked solutions with systematic detuning 66
3.34 Destabilization of mode-locked solution by systematic detuning 66
3.35 Landscape of solutions for a frequency comb with systematic detuning 67
3.36 Mode locking in large ensembles of oscillators with modal frequency structure 70
3.37 Mode breathing observed in the modal order parameters for a mode-locked solution in a large ensemble 71
3.38 Mode locking for a large ensemble with 31 distinct modes . . . 71
3.39 Modulated mode-locked solution on the verge of breakdown . 73
3.40 Destabilization of mode locking for substantially overlapping modes 74
3.41 Effective and natural frequencies of the modulated mode-locked solution on the verge of breakdown 74
3.42 Mode locking in a large ensemble with Kuramoto-type coupling 75
3.43 Coexisting modal chaos in large systems with Kuramoto-type coupling 76

4.1 Characteristics of the of the stimulus action function h_1 83

4.2 Transport pattern after a single stimulus h_2 85
4.3 Transport pattern after a single stimulus h_1 86
4.4 Coherence echoes following after two stimuli h_2 87
4.5 Coherence echoes following after two stimuli of type h_1 88
4.6 Evolution of a synthetic mode-locked initial condition with coupling $(K, \gamma) = (0.95, 0.7)$ and snapshots 90
4.7 Evolution of a synthetic mode-locked initial condition $K = 0$ with modal order parameters 93
4.8 Evolution of a synthetic mode-locked initial condition, $(K, \gamma) = (0.95, 0.7)$ with modal order parameters 93
4.9 Dependence of the echo strength on the nonlinear interaction for the synthetic mode-locked initial conditions 94
4.10 Accumulation of a stimulated mode comb by periodic stimulation 96
4.11 Stimulated mode locking of uncoupled oscillators for pure sine stimuli, h_1 with $\alpha = 1$ 98
4.12 Stimulated mode locking of uncoupled oscillators for stimuli with two harmonics, h_1 with $\alpha = 0.5$ 98
4.13 Stimulated mode locking of uncoupled oscillators for resetting stimuli h_2 99
4.14 Echo response after termination of the periodic stimulation with resetting stimuli h_2 100
4.15 Impact of the global interaction on stimulated mode locking for h_1 with $(\alpha, \varepsilon) = (1, 1)$ 101
4.16 Impact of the second harmonic global coupling on stimulated mode locking for h_1 and h_2 102

1

Introduction

"We need a dream-world in order to discover the features of the real world we think we inhabit."

– Paul Karl Feyerabend, *Against Method*

1.1 Preamble

The Kuramoto model of coupled phase oscillators which was derived in the 1970s is viewed today as a paradigm in the description of synchronization phenomena in a diverse range of models involving weakly coupled limit cycle oscillators [1]. The phenomenon of collective synchronization is pervasive in the dynamics of nonlinear oscillator systems. However, there is another type of collective behavior called *mode locking* that has not been studied before in the Kuramoto model.

The present work deals with this new type of collective behavior that is inspired by the dynamics of mode-locked lasers, which are specific laser systems built to produce short light pulses. The notion of mode-locked solutions in the Kuramoto model supplements the existing knowledge about the dynamics of phase oscillator systems below the threshold of collective synchronization. It should be emphasized that mode locking is a general phenomenon that can be found in a variety of coupled oscillator systems.

The first key ingredient to the mode-locking phenomenon is a global interaction scheme, which makes the Kuramoto model an ideal candidate. Secondly, but of the same importance, one has to consider well-structured natural frequencies which can be, for instance, equidistant. Making use of these two key ingredients, a new solution type is discovered in the Kuramoto model, which is characterized by sharp pulses in the Kuramoto order parameter, see Fig. 1.1.

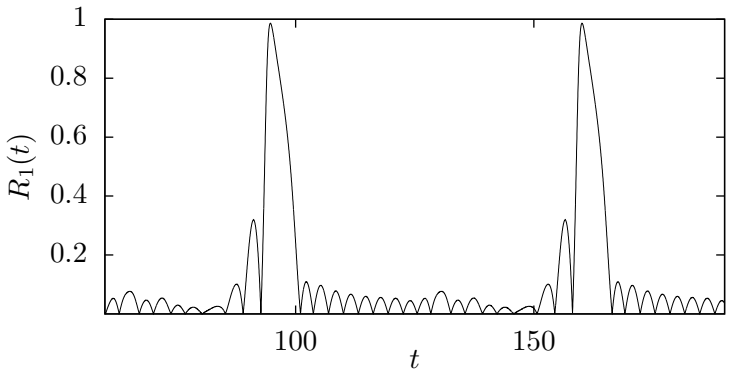

Figure 1.1: For equidistant natural frequencies and Kuramoto-type global coupling, pulsed periodic solutions below the synchronization threshold $K < K_C$ exist.

By investigating mode locking in the context of the basic phase oscillator models, general aspects of the phenomenon can be revealed, which are of importance for the theory of coupled oscillator systems. The present work complements previous works on mode locking in coupled oscillator systems, especially regarding situations involving many oscillators [2]. It is shown that the recently discovered phenomenon of coherence echoes [3], which appears as a response to external stimulation, can be viewed as a consequence of mode locking.

1.2 Thesis Overview

Chapter 2

Chapter 2 covers an introduction to globally coupled phase oscillator models and the phase reduction technique that is used to derive them for weakly-coupled limit cycle oscillators. The two well-known states of collective synchrony and phase turbulence are briefly presented, while it should be noted that the presentation is not exhaustive. The subsequent description of circle maps gives the necessary background from which one can understand oscillator systems that are subject to brief periodic stimulation. To enable the reader to anticipate connections between the coherence echo phenomenon and mode locking, the phenomenon is presented in its basic form following [3]. The final section is concerned with the numerical methods used for simulations, dynamical parameter continuation, and the computation of Lyapunov exponents.

Chapter 3

Chapter 3 starts with the presentation of the basic model, its properties and a description of the concept of effective frequency combs, which is identified as one of the key components for understanding mode-locked structures. Following that, a characterization of a prototypical mode-locked solution is given which already allows one to identify some of the general features of mode locking. Most importantly, it is found that the pulsed mean field of the prototypical solution has the form of a normalized absolute value of a Dirichlet kernel. The average magnitude over time of this particular pulse form turns out to be well below the expected typical value for comparable states of phase turbulence. Noteworthy, this particular form is analogous to the time evolution of the intensity of optical pulses.

Formal definitions of the mode-locked solutions are given, which include the two main types of harmonic and subharmonic solutions. The definitions can be adapted to other models for the classification of mode-locked solutions. The mode-locked solutions described are discovered in the Kuramoto model with equidistant natural frequencies, and how suitable initial conditions can be generated in order to obtain the solutions is presented. In this case, self-organized mode locking was not observed, thus coexistence between extensive chaos and stable mode locking is observed.

Self-organized mode locking is achieved when more involved coupling functions are considered, including foremost a second harmonic term (Kuramoto-Daido type models [4]). Here one finds regions in the parameter space where unique mode-locked solutions develop from randomly chosen initial condition after chaotic transient episodes. It is shown that the average transient length critically depends on the presence of the second harmonic term in the interaction.

A comparison of the rates of expansion and contraction along the stable mode-locked solutions for both types of interaction functions reveals a subtle balance between long periods of weakly expanding phase space volumes and short periods of strong contraction. The comparison especially shows the impact of the second harmonic on the stability of the pulsed solutions.

The most abundant scenario as to how the stability of a mode-locked solution is lost is by intermittency between phase turbulence and an unstable pulsed solution appearing as a bursting in the mean field. Along the stability boundaries of the mode-locked solutions, one can also find strange attractors that emerge in the breakdown of invariant tori or in period doubling cascades. The solutions in these particular cases remains pulsed and have the

characteristic properties of low-dimensional chaos, resulting in a jittering of the inter-pulse intervals and the pulse heights.

Mode-locked solutions are found to exist independently of the system size, however, the average length of chaotic transients scale exponentially with the number of oscillators, which conforms to supertransient behavior of type-II [5]. The supertransient behavior together with the importance of the second harmonic for self-organized mode locking clarifies to a certain extent why these solutions have not been described before.

The investigation of randomly and systematically perturbed equidistant frequency combs reveals that the ability of the system to develop mode locking can be characterized by the order present in the chosen natural frequencies. This especially highlights the importance of commensurability among the chosen natural frequencies of the oscillators. Furthermore, it is shown that mode locking cannot be expected for generic randomly-chosen natural frequencies even when the underlying frequency distribution is uniform.

With the prospect of applications the mode-locking phenomenon is investigated for large ensembles of oscillators where the notion of modal order parameters is introduced to characterize the mode-locking transition in a two-stage process of inner-modal synchronization and subsequent mode locking. The stability of the mode locking is investigated with respect to spectral width within the modes, where prior to the complete breakdown of mode locking, a curious period-two modulation phenomenon occurs. The modulation is found to be a result of a periodic forcing exerted by the mode-locked population on the unlocked population and also relies on the presence of the second harmonic in the interaction.

In the last section, a qualitative comparison to the dynamics of mode-locked lasers is given where the most important common features and the points that are either specific to optical or phase oscillator mode locking are collected.

Chapter 4

Chapter 4 establishes a relationship between mode locking and the coherence echo phenomenon. The basic coherence echo phenomenon is revisited, where the emphasis is put on the identification of mode combs, which are characteristic structures affiliated with mode locking. It was discovered that the echo phenomenon is due to the stimulation of a partially mode-locked initial condition which appears when at least two consecutive stimuli are applied.

By studying an idealized so-called *synthetic mode-locked initial condition*,

it is revealed that the magnitudes of the echoes can behave non-monotonously, which is explained by using a set of modal order parameters. Furthermore, it is shown that the global interaction influences the echoes significantly in this case due to the large coherence of the initial configuration.

It was found that under continued periodic stimulation at regular intervals, fully mode-locked states develop gradually, and that the pulsation synchronizes to the external stimulation. The ensembles of stimulated oscillators are regarded in the coupling free limit, where one can reduce the system to a collection of circle maps. Here it is shown that the response to stimulation depends drastically on the initial state of the system, while the resulting rotation numbers do not. The variation of the pulsation can be linked to the subharmonically locked oscillators that are always present in the staircases of the rotation numbers. Employing the global coupling successively increases the locking plateaus, which directly corresponds to an increase in the stimulated pulsation. Thus, it is demonstrated that for global coupling schemes such as the Kuramoto-type sine coupling, the stimulated mode locking is enhanced.

Chapter 5

In last chapter 5, the findings are summarized and some ideas for future research are collected.

2

Background

"Two roads diverged in a yellow wood,
And sorry I could not travel both
And be one traveler, long I stood
And looked down one as far as I could
To where it bent in the undergrowth;"

– Robert Frost, *The Road Not Taken*

2.1 Models of Coupled Phase Oscillators

Systems of coupled phase oscillators have been established as a paradigm in the description of collective synchronization phenomena where the enormous variety of coupling schemes and frequency distributions found in the literature reflect on the wide range of applications. As such, phase oscillator models can be employed to model biological rhythms; mechanical and electronic systems, e.g. flashing fireflies [6]; collective stepping of pedestrians on a bridge [7]; arrays of coupled Josephson junctions [8] or power grids [9]. In a recent investigation, it was shown that the Lugiato-Lefever equation describing the formation of optical pulses can be reduced to phase dynamics while maintaining some of the important features of the model [10]. This newly established connection between the dynamics of phase oscillators and mode-locking in optics motivates study mode locking as a new type of collective behavior in systems of coupled phase oscillators. This section serves as an introduction to phase oscillator models, the phase reduction technique, the concept of synchronization, and phase turbulence that are necessary to distinguish and characterize mode locking.

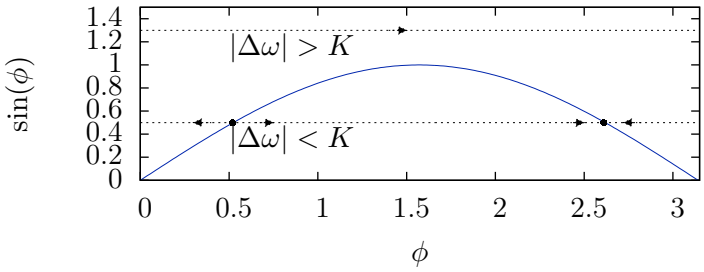

Figure 2.1: Illustration of the direction of the flow for the Adler equation for $|\Delta\omega| < K$ and $|\Delta\omega| > K$.

2.1.1 Synchronization and the Adler Equation

A straightforward introduction to synchronization can be given by the example of the Adler equation [11, 12], which models the synchronization of an oscillator to the frequency of an external oscillator or drive

$$\dot{\theta} = \omega + K\sin(\theta - \theta_{\text{ext}}), \tag{2.1}$$

$$\dot{\theta}_{\text{ext}} = \omega_{\text{ext}}, \tag{2.2}$$

where $K \in \mathbb{R}^+$ is the interaction strength, $\theta, \theta_{\text{ext}} \in \mathbb{S}^1$ are the phase variables, and $\omega, \omega_{\text{ext}} \in \mathbb{R}$ are two natural frequencies. Because the interaction depends only on the phase differences $\phi = \theta - \theta_{\text{ext}}$, one can rewrite the system for the phase difference which gives called the *Adler equation*

$$\dot{\phi} = \Delta\omega + K\sin(\phi), \tag{2.3}$$

where $\Delta\omega = \omega - \omega_{\text{ext}}$ is the detuning or mismatch of the two frequencies. Equilibria given by $\Delta\omega = -K\sin(\phi)$ correspond to synchronized solutions where the forced oscillator $\dot{\theta} = \omega_{\text{ext}}$ is entrained accordingly. The region where the frequency of the driven oscillator becomes identical to the one of the external drive is called *locking cone*. Two equilibria exist for $|\Delta\omega| < K$ where one is stable and the other is unstable. With $|\Delta\omega| > K$, one obtains the asynchronous evolution of the two phases. The situation for which both equilibria coalesce in saddle-node bifurcation $|\Delta\omega| = K$ gives rise to a homoclinic orbit.

2.1.2 Weakly-Coupled Oscillators and Phase Reduction

As a starting point, one might want to answer the question of how general phase oscillator models are, and in particular, in what type of situation one can make use of them. To give an answer to this question, the approach

of phase reduction is presented here. The two most important steps of the approach are the definition of the phase of the limit cycle, and the justification that the concept of the phase can be extended in a small neighborhood around the stable limit cycle, which makes it possible to deal with perturbations. For weakly-coupled and almost identical oscillators, one can then utilize the method of averaging, which further reduces the interactions to periodic functions of phase differences.

In the following, a system of two weakly-coupled limit cycle oscillators is considered to introduce the technique as it has been presented in [1, 13]. Consider the system of weakly-coupled ordinary differential equations given by

$$\dot{X}_k = F_k(X_k) + \varepsilon H(X_k, X_j), \quad k, j \in \{1, 2\}, \tag{2.4}$$

where $X_k \in \mathbb{R}^I$ is the state of the oscillator with index k and $2 \leqslant I \in \mathbb{N}$, $F_k(X_k) : \mathbb{R}^I \to \mathbb{R}^I$ is the right-hand side of the uncoupled oscillator, $\varepsilon \ll 1$ is a small parameter, and $H(X_k, X_j) : \mathbb{R}^I \times \mathbb{R}^I \to \mathbb{R}^I$ is the coupling function.

Furthermore, we assume that the dynamics of the two oscillators only differ at an order of $\mathcal{O}(\varepsilon)$, such that, for the uncoupled oscillators one can write

$$\dot{X}_k = F(X_k) + \varepsilon f_k(X_k), \quad k \in \{1, 2\}, \tag{2.5}$$

where $f_k(X_k) : \mathbb{R}^I \to \mathbb{R}^I$ denotes the differences of the right-hand side.

To reduce (2.4) to phase dynamics, one first needs to introduce the phases $\phi_k \in \mathbb{S}^1$ which parametrize the limit cycles. Both phases $\phi_k(t)$ are defined to progress with a constant speed along the periodic solution $X_k^0(t) = X_k^0(t + T)$ that is found for $\varepsilon = 0$ such that

$$\dot{\phi}_k(X_k) = 1 \quad k \in \{1, 2\}. \tag{2.6}$$

Let X_k^0 be any point on the stable limit cycle Γ^0 of period T and $\tilde{X}_k \in U(\Gamma^0)$ be a small neighborhood of Γ^0, that is, $\left|\tilde{X}_k(t) - X_k^0(t)\right| \to 0$ as $t \to \infty$. The *isochrones* are the $(I-1)$-dimensional hypersurfaces filling $U(\Gamma^0)$, where to every isochrone there is an associated asymptotic phase on Γ^0. With the periodic mapping $P : \tilde{X}_k(t) \to \tilde{X}_k(t + T)$, the asymptotic phase can be defined as $\phi(\tilde{X}_k) = \lim_{i\to\infty} P^i(\tilde{X}_k)$. Details about the existence and certain properties of the isochrones can be found in [14]. The concept of the isochrones enables one to define the phase not only on the limit cycle itself, but also in a small neighborhood around it such that one can use the phase description when also dealing with small perturbations. Letting $\varepsilon > 0$, applying the chain rule one formally to $\phi_k(X_k(t))$, and using (2.4), (2.5), (2.6) one obtains

$$\dot{\phi}_k(X_k) = 1 + \varepsilon \nabla_{X_k} \phi_k \left[f_k(X_k) + H(X_k, X_j)\right] \quad k, j \in \{1, 2\}, \tag{2.7}$$

where ∇_{X_k} denotes the gradient with respect to X_k. While X_k and X_j are generally not known, one can replace them with the $X_k^0(\phi_k)$ on the right-hand side to obtain the lowest order approximation in ε

$$\dot{\phi}_k = 1 + \varepsilon Z(\phi_k)\left[f_k(X_k^0(\phi_k)) + H(X_k^0(\phi_k), X_j^0(\phi_j))\right] \quad k, j \in \{1, 2\}, \tag{2.8}$$

where $Z(\phi_k) = \nabla_{X_k}\phi_k|_{X_k = X_k^0}$ is the so-called *phase sensitivity function* which can be obtained via the method of the adjoint equation [15, 16].

To apply the method of averaging to (2.8), one first transforms the phases according to $\phi_k = \omega^0 t + \theta_k$, where specifically θ_k is varying slowly as compared to $\omega^0 t$. Here, $\omega^0 = 2\pi/T$ is the speed on the limit cycle for $\varepsilon = 0$ that is implicitly defined by (2.6). The resulting equations that may then be averaged over t read

$$\dot{\theta}_k = \varepsilon Z(\omega^0 t + \theta_k)\left[f_k(X_k^0(\omega^0 t + \theta_k)) + H(X_k^0(\omega^0 t + \theta_k), X_j^0(\omega^0 t + \theta_j))\right], \tag{2.9}$$

with $k, j \in \{1, 2\}$, and in particular, all functions are T-periodic in t.

Theorem 2.1.1 (The Averaging Theorem [17])**.** *Considering a dynamical system of the form*

$$\dot{u} = \varepsilon g(u, t, \varepsilon); \quad u \in D \subset \mathbb{R}^I, 0 \leqslant \varepsilon \ll 1, \tag{2.10}$$

where $g : \mathbb{R}^I \times \mathbb{R} \times \mathbb{R}^+ \to \mathbb{R}^I$ is C^r smooth function with $r \geqslant 2$. Let g be bounded on bounded sets and periodic in t with period T. The averaged system is then defined as

$$\dot{y} = \varepsilon \frac{1}{T}\int_0^T g(y, t, 0)dt =: \varepsilon \bar{g}(y). \tag{2.11}$$

There exists a C^r change of coordinates $u = y + \varepsilon w(y, t, \varepsilon)$ under which (2.10) becomes

$$\dot{y} = \varepsilon \bar{g}(y) + \varepsilon^2 g_1(y, t, \varepsilon), \tag{2.12}$$

where g_1 is of period T in t.

The system (2.9) fulfills the requirements of the averaging theorem, therefore the averaged system is given by

$$\dot{\theta}_k = \varepsilon\left[\omega_k + \bar{H}(\theta_j - \theta_k)\right] \quad k, j \in \{1, 2\}, \tag{2.13}$$

where $\bar{H}(\theta_j - \theta_k)$ and ω_k are

$$\bar{H}(\theta_j - \theta_k) = \frac{1}{T}\int_0^T Z(\omega^0 t + \theta_k)H(X_k^0(\omega^0 t + \theta_k), X_j^0(\omega^0 t + \theta_j))dt, \tag{2.14}$$

$$\omega_k = \frac{1}{T}\int_0^T Z(\omega^0 t + \theta_k)f_k(X_k^0(\omega^0 t + \theta_k))dt, \tag{2.15}$$

here $\bar{H} : \mathbb{S}^1 \to \mathbb{S}^1$ is a general periodic function of the phase difference.

2.1.3 The Kuramoto Model

Kuramoto made a substantial extension to the concept of collective synchronization in coupled oscillator systems in [1] when he first successfully treated the transition to collective synchrony of a system of globally-coupled phase oscillators in the continuum limit. A short introduction and an extensive review of the Kuramoto model can be found in [18, 19]. Kuramoto realized that an analytic treatment of the collective synchronization problem is possible by truncating the interaction function in (2.13) after the first sinusoidal harmonic. Additionally, he chose the number of oscillators N to be arbitrarily large and normalized the interaction accordingly, which led him to the *Kuramoto model* of globally coupled phase oscillators

$$\dot{\theta}_k = \omega_k + \frac{K}{N}\sum_{j=1}^{N}\sin(\theta_j - \theta_k), \quad k = 1, \dots, N, \tag{2.16}$$

where $K \in \mathbb{R}$ denotes the coupling strength, $N \in \mathbb{N}$ is the number of oscillators, and $\omega_k \in \mathbb{R}$ are the natural frequencies. The all-to-all sinusoidal interaction can be expressed by the means of a single *complex order parameter* given by

$$\eta(t) = R(t)e^{\mathrm{i}\Psi(t)} := \frac{1}{N}\sum_{j=1}^{N} e^{\mathrm{i}\theta_j(t)} \in \mathbb{C}, \tag{2.17}$$

such that one can rewrite the system as follows

$$\begin{aligned}\dot{\theta}_k &= \omega_k + \frac{K}{2\mathrm{i}}\left(\eta(t)e^{-\mathrm{i}\theta_k(t)} - \bar{\eta}(t)e^{\mathrm{i}\theta_k(t)}\right), \\ &= \omega_k - KR\sin(\theta_k - \Psi),\end{aligned} \tag{2.18}$$

where $\bar{\eta}$ denotes the complex conjugate of the order parameter. The modulus of the order parameter is a natural measure of phase coherence, which is why R is also referred to as the *coherence radius*. In the case that the natural frequencies ω_k follow a normalized symmetric unimodal distribution $g(\omega + \omega_c) = g(-\omega + \omega_c)$ with average frequency ω_c, the system can be transformed into a co-rotating frame by applying $\theta_k \to \theta_k + \omega_c t$. For steady state solutions $R(t) = \text{const.}$ in the co-rotating frame, one can set $\Psi = 0$. Here, the order parameter effectively becomes a parameter in the evolution of each unit such that one is faced with a solvable self-consistency problem.

His self-consistency approach allowed Kuramoto to derive the critical coupling strength $K_C = 2/(\pi g(0))$ at which a branch of partially synchronized solutions bifurcates from the state of incoherence given by $R = 0$. Close to the bifurcation, the order parameter was found to exhibit square root scaling law, which for the standard Cauchy distribution $g(\omega) = 1/(\pi(1 + \omega^2))$

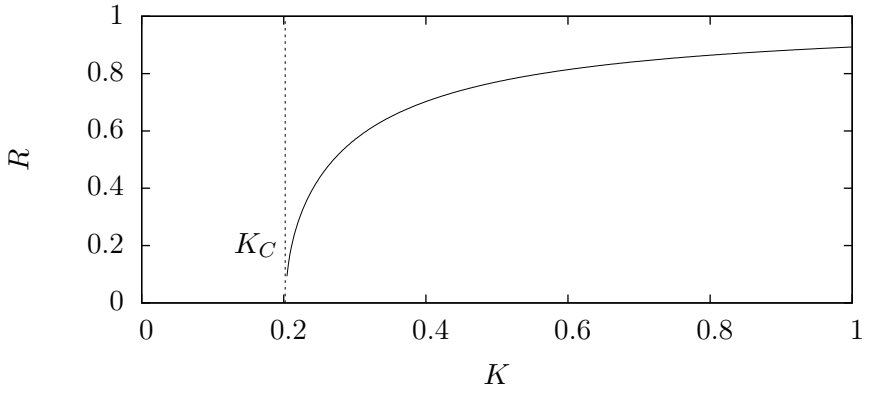

Figure 2.2: Transition from incoherence $K < K_C$ to partial synchrony $K > K_C$ for the natural frequencies drawn from a standard Cauchy distribution $g(\omega)$.

is $R = \sqrt{(1 - K_C/K)}$. The corresponding second order phase transition to synchrony is illustrated in Fig. 2.2.

2.1.4 Daido's Extension of the Coupling Function

The simplifying assumption of a first harmonic interaction function which is surprisingly adequate in a variety of applications was extended by Daido [4] to include higher order Fourier components in the interaction function. For phase reduced models of weakly-coupled limit cycle oscillators, Daido's extension is of great importance because it covers a much wider range of models. However, the more general form comes with the price that the theory of collective synchronization is already much more involved. This is illustrated by the fact that clustered states may appear [20]. Just to name one example, the interaction functions between weakly-coupled Hodgkin-Huxley neurons in the corresponding phase model were found to contain the first four harmonics [21]. The general *Kuramoto-Daido model* of globally-coupled phase oscillators has the form

$$\dot{\theta}_k = \omega_k + \frac{K}{N} \sum_{j=1}^{N} h(\theta_j - \theta_k), \quad k = 1, \ldots, N, \tag{2.19}$$

with a 2π-periodic interaction function that can be expressed in the form of a Fourier series

$$h(\theta) = \sum_{q=1}^{\infty} \left[h_q^{(s)} \sin(q\theta) + h_q^{(c)} \cos(q\theta) \right], \tag{2.20}$$

where a constant term with $q = 0$ is omitted without a loss of generality, and the superscripts (s),(c) indicate sine and cosine-like harmonics. Furthermore, with $h_q = (h_q^{(c)} - \mathrm{i}h_q^{(s)})/2$ for $q > 0$ and $h_{-q} = \bar{h}_q$, where the overbar denotes the complex conjugate, this can be written as

$$h(\theta) = \sum_{q\in\mathbb{Z}} h_q e^{\mathrm{i}q\theta}, \tag{2.21}$$

The mean field description of the model comprises the *generalized complex order parameters*

$$\eta_q(t) = R_q(t)e^{\mathrm{i}\Psi_q(t)} := \frac{1}{N}\sum_{j=1}^{N} e^{iq\theta_j(t)} \in \mathbb{C}, \tag{2.22}$$

where q is the degree of the harmonic. Applying the generalized order parameters, the model becomes

$$\dot{\theta}_k = \omega_k + \frac{K}{N}\sum_{j=1}^{N}\sum_{q\in\mathbb{Z}} h_q e^{\mathrm{i}q(\theta_j-\theta_k)} \tag{2.23}$$

$$= \omega_k + K\sum_{q\in\mathbb{Z}} h_q\eta_q e^{-\mathrm{i}q\theta_k}, \tag{2.24}$$

for which the collective synchronization transition in the thermodynamic limit was successfully treated in a self-consistency approach similar to the one used by Kuramoto. Daido found that the critical coupling in the thermodynamic limit is

$$K_C = \frac{2h_1^{(s)}}{\pi g(\omega_C)((h_1^{(s)})^2 + (h_1^{(c)})^2)}, \tag{2.25}$$

where $g(\omega_C)$ is the distribution function of the ω_k evaluated at the entrainment frequency. A crucial restriction Daido makes on the coupling function is that there is only one minimum and one maximum, which means that the first harmonic is much stronger than the other terms in the interaction. This assumption assures a certain similarity to the Kuramoto-type coupling. Furthermore, note that the synchronization theory presented is strictly only valid in the thermodynamic limit $N \to \infty$. The quantities R_q and Ψ_q characterize the collective behavior of the system. While $R_1(t)$ quantifies the degree of total phase synchronization corresponding to a monopole distribution of the oscillators, the higher order parameters measure higher order moments of the distribution of the oscillators. For instance in $R_2(t)$, the emergence of dipole shape configurations can be seen [1, 22].

2.1.5 Extensive Chaos Below the Synchronization Threshold

The typical behavior of a system of phase oscillators below the synchronization threshold $K < K_C$ is a state of *phase turbulence* presenting a large number of positive Lyapunov exponents [23]. The extensive nature of the phase turbulence was shown in some detail in numerical experiments, however, raising the question of whether this situation would not be sensitive to the chosen realization of the natural frequencies. It was found that the specific realizations of the frequencies in finite size systems influence the synchronization transition in the way that oscillators with frequencies closest to each other tend to synchronize first [24].

Of special importance for the present work are equidistant natural frequencies which might be interpreted as a special realization of frequencies that conforms with a uniform frequency distribution. Even for this particular frequency realization, the incoherent state is the typical solution to be observed in the Kuramoto model. The transition to synchrony for this type of realization was found to be a first-order phase transition for which corrections to the continuum limit synchronization threshold could be established [25]. In the recent past, great accomplishments regarding the incoherent state for random frequencies in finite size systems and in the continuum limit were made [26, 27] such that the picture of a stable incoherent state below the synchronization threshold and the bifurcation scenario conjectured by Kuramoto to collective synchrony could be confirmed.

However, caution is advised because incoherence is not the only possible type of behavior below the threshold of collective synchronization. For equidistant or nearly equidistant natural frequencies, mode locking exists for $K < K_C$, which is a new type of collective behavior. Although equidistant natural frequencies are uniform, it is clear that they are exceptional and fundamentally different from randomly chosen frequencies. The equidistant frequencies, as opposed to randomly chosen frequencies, conform to the concept of hyperuniformity regarded in the frequency domain [28].

2.2 Circle Maps Mode Locking and Resonances

In mathematics, a particular notion of mode locking appears in the context of circle maps. The main difference to the notion of mode locking that is known in laser physics is that it usually does not refer to a collective phenomenon. Circle maps and phase oscillator models are deeply related such that one can expect to find connection and relations between helpful concepts. In this

regard, the most important candidate is that of the rotation numbers, which is related in phase oscillator systems to the average frequencies.

In this section, the Arnold circle map and globally-coupled circle maps are presented. For the Arnold circle map, the notions of the rotation number and resonant locking are of primary interest, while the extension to coupled circle maps allows promoting ideas about extensivity and collective types of behavior.

2.2.1 Arnold Circle Map

A circle map is a time discrete mapping on the circle with one of the most prominent examples being the *Arnold circle map* [29, 30]

$$\theta_{\nu+1} = \theta_\nu + 2\pi\omega + K\sin(\theta_\nu) \mod 2\pi, \tag{2.26}$$

where $\nu \in \mathbb{N}$ is the discrete time index, $\theta \in \mathbb{S}$ is the phase variable, $\omega \in [-1, 1]$ is the natural phase increment, and $K \in [0, 1]$ is the strength of the nonlinearity. The common approach to studying the dynamics of this system involves the so-called *rotation number*, which is a fundamental quantity in the study of circle maps and defined by

$$W_{\omega,K}(\tilde{\theta}_0) := \lim_{\nu\to\infty} \frac{\tilde{\theta}_\nu - \tilde{\theta}_0}{2\pi\nu}, \tag{2.27}$$

where $\tilde{\theta} \in \mathbb{R}$ denotes the phase variable lifted to the universal cover of $\mathbb{S}$. The rotation number corresponds to the average number of rotations of the circle map per iteration, which can be seen as an analog to the average angular velocity of a phase oscillator. It is known that for (2.26), the limit (2.27) indeed exists and further that it is independent of $\tilde{\theta}_0$ [30].

The distinction between periodic and quasiperiodic motion is made by the rotation number, which is rational $W_{\omega,K} \in \mathbb{Q}$ in the periodic case, and irrational in the quasiperiodic case. Starting from the linear case $K = 0$, one obtains periodic motion only for ω values which are exact rationals corresponding to elements of the *Farey sequence*

$$F_i := \left\{ \frac{p}{q} : p, q \text{ coprime}, 0 \leqslant p < q < i \right\}, \tag{2.28}$$

where $i \in \mathbb{N}$ in this context will be called the *Farey order*. Interestingly, for increasing $1 \geqslant K > 0$, one finds regions around the exact rational $\omega \in \cup_{i\in\mathbb{N}} F_i$ where the rationality of the rotation number is maintained. A comparison between the rotation number and the natural phase increment reveals a *Devil's*

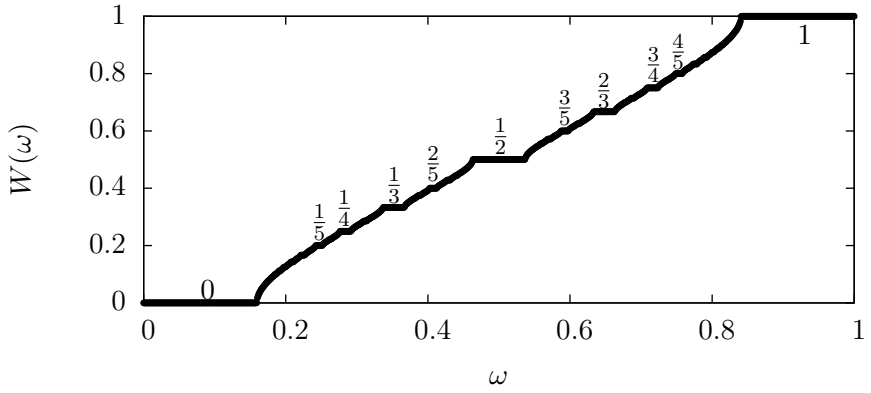

Figure 2.3: Devil's staircase with multiple locking plateaus in $W(\omega)$ for the Arnold circle map (2.26) with $K = 1$.

staircase, see Fig. 2.3. By extending the staircase in K direction, *locking cones* also known as *Arnold tongues* appear, which are regions of rational rotation numbers in the space spanned by K and ω. Note that with increasing Farey order, the areas of the tongues decrease. While the Arnold circle map (2.26) is only concerned with a single phase variable, it is interesting to discuss the situation of multiple coupled phase variables.

2.2.2 Globally-Coupled Circle Maps

By extending the number of maps and involving a global coupling scheme, one obtains *globally-coupled circle maps* as introduced by Kaneko [31]

$$\theta_{\nu+1}(k) = \theta_\nu(k) + \frac{K}{N} \sum_{j=-n}^{n} \sin(\theta_\nu(j) - \theta_\nu(k)) \mod 2\pi, \tag{2.29}$$

where $k \in \{-n, \ldots, n\}$ denotes the map index of the $N = 2n + 1$ coupled circle maps. The one dimensional circle map is therefore extended to an N-dimensional system of globally-coupled circle maps with coupling similar to the sine coupling of the Kuramoto model (2.16). Similar to the order parameter used to describe the interaction in the Kuramoto model, one can use

$$\eta_\nu = R_\nu e^{i\Psi_\nu} := \frac{1}{N} \sum_{k=-n}^{n} e^{i\theta_\nu(k)} \in \mathbb{C}. \tag{2.30}$$

Using this order parameter to rewrite (2.29) results in

$$\theta_{\nu+1}(k) = \theta_\nu(k) - KR_\nu \sin(\Psi_\nu - \theta_\nu(k)) \mod 2\pi. \tag{2.31}$$

In this particular example, all of the units are identical in the sense that the natural phase increments are all zero. Introducing a heterogeneity in the model results in

$$\theta_{\nu+1}(k) = \theta_\nu(k) + 2\pi\omega_k + \frac{K}{N}\sum_{j=-n}^{n}\sin(\theta_\nu(j) - \theta_\nu(k)) \mod 2\pi, \qquad (2.32)$$

where $\omega_k \in [-1, 1]$ denotes the different natural phase increments. Locking and therefore the appearance of periodic motion in the context of the Arnold circle map (2.26) referred to $W_{\omega,K} \in \mathbb{Q}$, which is depending on the phase increment ω and the nonlinearity K. In the case of coupled maps (2.32), one would similarly be interested in studying the relationship between the different ω_k and K to identify periodic, quasiperiodic, and chaotic regimes, as well as collective types of behavior.

The notion of the rotation numbers can be carried over in the context of the multiple circle maps by defining the rotation numbers

$$W_{\omega_k,K}(\tilde{\theta}_0(k)) := \lim_{\nu\to\infty}\frac{\tilde{\theta}_\nu(k) - \tilde{\theta}_0(k)}{2\pi\nu}, \qquad (2.33)$$

which results in a *rotation vector* $W = (W(-n), \ldots, W(n)) \in \mathbb{R}^N$ if the limits exist. The rotation number for the single circle map (2.26) was noted to be independent of the initial condition, which is not necessarily true for mutually coupled maps. Note that the rotation vector does not always exist, however, in that cases one can still form what is called a rotation set [2].

For systems of coupled circle maps, the commensurability between all entries of the rotation vector becomes a necessary condition for a periodicity. It assures that all the rotation numbers are rationally related pairwise

$$W(j)p = W(k)q, \quad \forall j, k \in \{-n, \ldots, n\}, \qquad (2.34)$$

where $p, q \in \mathbb{N}$. The intriguing part is now that one does not know when the global interaction warrants the stabilization of the resonances among the rotation numbers. Even for the case that one chooses the natural phase increments ω_k, mutually resonant the interaction has to support the locking dynamically.

In particular, when the phase increments are equidistant $\omega_k = k/n$ for N coupled maps (2.32), the system allows for a special type of solution with a peculiar collective behavior. The solution is characterized by a pulsation of the coherence that is measured by R_ν. After multiple iterations with small coherence, a rapid increase in a pulse-like fashion is observed, see Fig. 2.4. To obtain the presented solution, one has to use initial conditions that have large

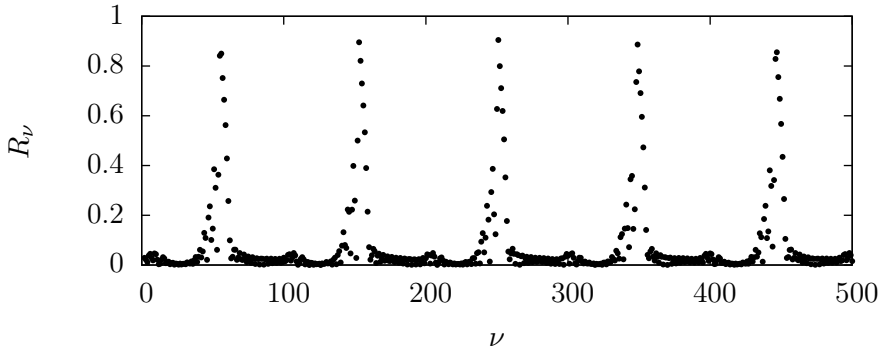

Figure 2.4: The iterates of the modulus of (2.30): R_ν for the system of $N = 2n + 1 = 31$ globally-coupled circle maps (2.32) with equidistant natural phase increments $\omega_k = k/n$ with $k \in \{-n, \ldots, n\}$ and coupling strength $K = 1$.

initial coherence ($R_0 \approx 1$). The presented model of globally-coupled maps is certainly interesting, however, it is meant only to illustrate the generic nature of the solution types that will be discussed for time-continuous systems. The pulsing solution is in fact a stroboscopic analog to pulsed solutions that can be found in time-continuous systems.

As pointed out in [31], coupled circle maps can be viewed as a prototypical system that develops extensive chaos. The same is true for coupled phase oscillator systems where among the presented phase turbulence, other exotic chaotic states known as *Chimeras* have been found for more involved coupling schemes [32, 33]. Although not much is known about the solution presented in Fig. 2.4, it is clear that the recurrently increasing values of R_ν are a manifestation of a collective type of behavior.

2.3 The Coherence Echo Phenomenon

This section serves as a brief introduction to an echo-type response phenomenon that was found in systems of coupled oscillators [3, 34]. Similar echo phenomena have been known for awhile in the field of plasma physics [35, 36] and as spin echoes in systems with nuclear magnetic dipoles in an inhomogeneous external magnetic field [37]. The basic phenomenon can be found by applying two stimuli separated by a time distance τ to a large ensemble of phase oscillators with random natural frequencies. It is then observed that increased coherence reappears after the second stimulus at integer multiples of τ. The reappearing coherence echoes are found to disap-

pear quickly at higher multiples of τ. The term *coherence echo* is chosen to stress the fact that the response is seen in the modulus of the first complex order parameter, the coherence radius $R_1(t)$.

2.3.1 Stimulation of Ensembles of Phase Oscillators

The idea behind stimulation is that an instantaneous external action is applied to the system state for a brief period of time or instantaneously. For simplicity, the stimuli considered are so-called *delta stimuli*, which cause an instantaneous change of the system state at a specific impact time $t = t_0$. A delta stimulus adjusts the system state according to an action function $h : \mathbb{S}^1 \to \mathbb{S}^1$ while otherwise not influencing the system's evolution, which makes this type particularly convenient for use in simulations. The preparation of the system state is done by the transformation

$$\theta(t_0^+) = \theta(t_0^-) - h(\theta(t_0^-)), \tag{2.35}$$

where at $t = t_0$ the system state is transformed from $\theta(t_0^-)$ to $\theta(t_0^+)$ for all oscillators in a discontinuous fashion. The types of action functions $h(\cdot)$ considered may be written as a Fourier series

$$h(\theta) = \sum_{l \in \mathbb{Z}} h_l e^{\mathrm{i}l\theta}. \tag{2.36}$$

The chosen action function has a strong influence on the coherence echoes, in particular, regarding their magnitude. In order to recover the effect presented in [3], one can use (2.36) including the first two odd harmonics

$$h(\theta) = \frac{\sin(\theta) + \sin(2\theta)}{2}. \tag{2.37}$$

2.3.2 Coherence Echoes in Kuramoto-Type Systems

A system of globally-coupled phase oscillators (Kuramoto-type), below the synchronization threshold $K < K_C$ and with natural frequencies that are drawn from a Gaussian distribution is considered. The system will typically evolve towards a state of phase turbulence [23]. Application of two stimuli of the form (2.37) at t_0 and t_1 are sufficient to observe coherence echoes. The system responds with a coherence echo at approximately $t_1 + \tau$, where $\tau = t_1 - t_0$. The outcome of a numerical experiment for the system described is presented in Fig. 2.5, where the action of the stimuli is indicated, as well as the reappearance of increased coherence at $t = t_1 + \tau$. Additionally, the modulus of the second order parameter $R_2(t)$ is presented, which shows a sudden increase at $t = t_1 + \tau/2$. This will also be identified as a main feature of mode-locked solutions.

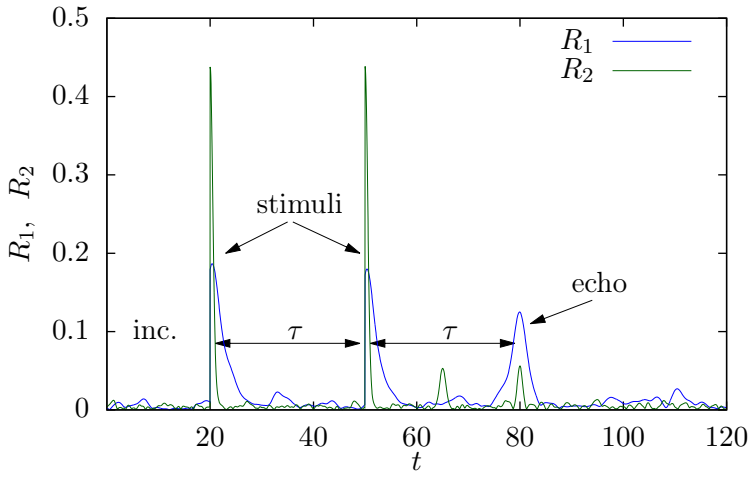

Figure 2.5: Coherence echo seen in $R_1(t)$ and $R_2(t)$ as a response to two stimuli (2.35) with (2.36) separated by a time distance $\tau = 30$. The system consists of $N = 5 \cdot 10^4$ oscillators with natural frequencies drawn from a standard normal distribution. The coupling strength is $K = 1 < K_C$.

2.4 Numerical Methods

Implementations of the numerical experiments for this work are done in C++ and make use of the libraries Armadillo, Boost [38, 39], and employ parallelization schemes from OpenMP [40].

2.4.1 Simulations

Explicit scheme

Simulations of differential equations are performed with a forward-explicit fourth order Runge-Kutta scheme [41]. Given an autonomous initial value problem $\dot{x} = f(x(t))$ with initial value $x(0) = x_0$, one can iterate the system forward in time from $t_0 = 0$ to $t_1 = h$ in a discrete fashion. The increment of the independent variable with each step is called step size h. Although in many applications methods with adaptive step size are preferable, such methods were not required in the context of this work. To obtain the approximate solution, one has to reapply the following iterative equation

$$x_{i+1} = x_i + h\frac{1}{6}\left(k_1 + 2k_2 + 2k_3 + k_4\right), \tag{2.38}$$

here x_i is the previous state and k_1, k_2, k_3, k_4 are evaluations of the r.h.s. at $(k_1, k_2, k_3, k_4) = (f(x_i), f(x_i + hk_1/2), f(x_i + hk_2/2), f(x_i + hk_3))$. The scheme presented is preserving invariant subspaces, which can lead to numerical trapping [42]. To avoid this problem appropriately, small perturbations are frequently applied in order to allow the system to diverge if instabilities transvere to the invariant subspaces appear. A second option to handle the problem of numerical trapping is to break the system symmetries by applying small quenched disorder in the natural frequencies.

Poincaré sections and maps

An important concept in the study of dynamical systems is that of Poincaré return maps. For the study of an N-dimensional dynamical system given by a system of differential equations, an $N-1$-dimensional hyperplane is chosen that adequately dissects the phase space. The consecutive returns of the trajectory to the Poincaré section generate a discrete map that is called *Poincaré return map*. The return time T_ν, where $\nu \in \mathbb{N}$, are the evolution times between crossings of the Poincaré section, and are often used to illustrate Poincaré maps. For a periodic orbit, the restriction to a Poincaré map lifts the phase shift symmetry resulting in a fixed number of section crossings. The number of crossings generally depends on the particular Poincaré section that is chosen, and should therefore be chosen with care. During the numerical simulations, the Poincaré maps are studied in order to identify regimes of periodic, quasiperiod or chaotic motion and characterize bifurcations.

In principle, one can always make use of what is known as Henon's trick, which refers to a transformation of the time into a dependent variable sufficiently close to the section crossing in order to arrive with machine precision on the chosen Poincaré section [43, 44]. Although this approach is generally possible once the system is sufficiently close to the hyperplane where the Jacobian is expected to be invertible, a linear approximation is often sufficient and will be used here.

Parameter scans

To detect bifurcations of solutions in numerical simulations, parameter scans can be performed where a system parameter is adapted and structural changes of the solution are observed. The adaptation of the parameter is usually performed adiabatically, which means that the parameter changes are small and succeeded by sufficiently long transients such that the system converges back to a stable regime. Due to the peculiar stability properties of the periodic solutions discussed in this work, a small extension of the basic procedure in

performing parameter scans is presented.

Periodic and chaotic trajectories can exhibit different rates of expansion and contraction at different points in phase space, such that perturbations of a parameter can have different effects depending on the exact moment when they are applied. In practice, this is often handled by making sufficiently small parameter steps in the scan. Smaller parameter increments, on the other hand, can increase the length of the computation of the scan substantially, making it sometimes favorable to vary the chosen parameter increment in different parameter regions of the scan. To obtain a reliable and detailed parameter scan, one typically has to restart the procedure and adjust the parameter steps.

The method of *slow adaptation of a parameter* can help to alleviate both problems at the same time by distributing the parameter change equally over a certain time window. In this way, perturbations are spread more evenly over the periodic orbit or on the chaotic attractor. The advantage of the procedure is that one needs less a priori knowledge of the stability properties of solutions.

Considering the initial value problem

$$\dot{x} = f(x, p), \quad x(0) = x_0, \tag{2.39}$$

where $p \in \mathbb{R}$ is a parameter and $x \in \mathbb{R}^N$ is an N-dimensional state vector, and $f : \mathbb{R}^N \times \mathbb{R} \to \mathbb{R}^N$ is a continuous function. The basic approach of a parameter scan is to adjust parameter p at the time moment τ

$$p^+ = p^- + \Delta_p \tag{2.40}$$

where p^- and p^+ are the parameter values right before and after the adaptation, and $\Delta_p \in \mathbb{R}\backslash\{0\}$ corresponds to the finite size parameter increment. The procedure described is the commonplace approach to investigate bifurcation scenarios in numerical simulations where Δ_p is also sometimes varied along a scan.

A simple but effective extension of this basic procedure is to distribute the adaptation of the parameter over a time interval of finite length t_{ad}. The simulation step size h is taken to be fixed and one chooses t_{ad} such that $t_{\text{ad}}/h \in \mathbb{N}$. Starting at time $t = \tau$, before the next t_{ad}/h simulation steps of the scheme (2.38), the parameter is adapted by

$$p^+ = p^- + \frac{\Delta_p h}{t_{\text{ad}}}, \tag{2.41}$$

where $\Delta_p h/t_{\text{ad}}$ can be as small as machine precision. The procedure can in principle also be formulated for methods with adaptive step size. Compared

to the basic procedure, where one only has to specify the desired parameter increment Δ_p, the distributed adaptation requires the additional time span t_{ad} over which the parameter change takes place. The procedure described is not only interesting to study stable periodic solutions with complicated structure, but also when chaotic attractors are explored that exhibit difficult stability properties. The method should be considered when switching between several stable attractors by small perturbations is possible.

For periodic solutions and potentially unstable solutions, it is clear that numerical bifurcation theory [17, 45] and path-following methods, e.g. pseudo-arclength continuation as implemented in AUTO or DDE-BIFTOOL [46, 47, 48, 49], are the most reliable tools and should if possible be preferred to direct simulations.

However, note that for large systems or when investigating chaotic attractors, simulations are frequently used due to their simplicity. To investigate, for instance, the properties of a chaotic attractor with numerical continuation methods one would have to study a representative collection of unstable periodic orbits within the attractor, which is not a straightforward task. In large systems and for long periodic orbits, it is further likely to encounter problems related to computer memory.

2.4.2 Lyapunov Spectra

Lyapunov exponents measure the average rate of contraction and expansion on an attractor in a dynamical system by means of the evolution of generic perturbations in the tangent spaces. Given an autonomous dynamical system

$$\dot{x} = f(x), \tag{2.42}$$

where $x \in \mathbb{R}^N$ is the N-dimensional state vector, $f(\cdot)$ is a continuously differentiable vector field one can obtain a solution $x(t)$ for a given initial condition $x(0) = x_0$. After the passage of a sufficiently long transient time, the solution is assumed to reache a periodic orbit or a chaotic attractor. To investigate the stability of the solution, one can use orbits that are arbitrarily close by $x(t)+u(t)$ and compute the linearized evolution of the perturbations along $x(t)$ which is given by

$$\dot{u} = J(x(t))u(t), \tag{2.43}$$

where J is the Jacobian matrix evaluated along the orbit $x(t)$. Integrating (2.43) leads to the tangent map $u(t) = M_{x_0}(t)u_0$ where $M_{x_0}(t)$ is the time-dependent transition matrix. The stability properties of $x(t)$ can be obtained by solving for the eigenvalues of $M_{x_0}(t)^T M_{x_0}(t)$, which are $\mu_1^2 \geqslant \cdots \geqslant \mu_N^2 \geqslant 0$. So far these depend in principle on the initial values x_0. However, it was

proven by Oseledets [50, 51] that for ergodic dynamical systems the *Lyapunov exponents* exist and that they are with probability one independant of x_0

$$\lambda_k = \lim_{t\to\infty} \frac{1}{t} \log \mu_k(t) \quad k \in \{1, \ldots, N\}. \tag{2.44}$$

The complete set $\{\lambda_1, \ldots, \lambda_N\}$ is called the *Lyapunov spectrum*, which is an invariant [50, 52].

Finite-time Lyapunov exponent

Lyapunov exponents in the usual sense are obtained for solutions that are already on a stable attractor, and therefore one computes the spectrum for the dynamical system and the specific attractor. Transients are pieces of solutions of dynamical systems where, in particular, an attractor has not been reached. Since transients by definition only exist for a finite time, the computation of the Lyapunov exponents does not make sense per se. However, finite-time quantities in the fashion of Lyapunov exponents can be calculated to gain insight. The so-called the *finite-time Lyapunov exponent* can be utilized to characterize transient behavior [53]. For different initial points along the transient $x(t_0), x(t_1), \ldots$ one computes the leading Lyapunov exponent for a short time window of length τ

$$\lambda_{\mathrm{ft}}(t_i) = \lim_{t\to t_i+\tau} \frac{1}{\tau} \log \mu_1(t). \tag{2.45}$$

Chaotic transients of two basic types can be distinguished by the dynamics of the finite-time Lyapunov exponent $\lambda_{\mathrm{ft}}(t)$. Type-I chaotic transients are characterized by a gradual decrease of the finite-time exponent, while for type-II transients, the finite-time exponent fluctuates around a certain value before it suddenly approaches zero, usually within the length of the chosen window.

Continuous Gram-Schmidt orthonormalization

In order to compute Lyapunov exponents for an attractor of a dynamical system, one has to deal, at least in numerical investigations, with the difficulty that without a procedure for orthonormalization, the matrix of the eigenvalue problem of the variational equations becomes ill-conditioned. This happens because in the general case the eigenvalues of the matrix diverge exponentially over time. To circumvent this problem, in numerical computations, it is common practice to use a Gram-Schmidt orthonormalization at regular intervals while storing the exponents for each interval [54, 55].

It is an interesting concept to include an orthonormalization procedure into the integration of the system such that orthonormalization is provided in a continuous fashion [56, 57]. Considering the dynamical system governed by the evolution equation

$$\dot{x} = f(x), \tag{2.46}$$

where $x \in \mathbb{R}^N$, the idea is that the dynamical system can be augmented with a time-dependent orthonormal frame, which consists of orthonormal vectors $E(t) = \{e_1(t), \ldots, e_N(t)\}$. With this orthonormal frame one can write the matrix elements of the Jacobian as $J_{lm} = (e_l, Je_m)$, where $(\cdot, \cdot)$ denotes the inner product in $\mathbb{R}^N$. Further, one introduces the stabilized matrix elements $L_{mm} = J_{mm} + \beta((e_m, e_m) - 1)$, $L_{lm} = J_{lm} + J_{ml} + 2\beta(e_l, e_m)$ and a real valued vector $\Lambda = \{\Lambda_1(t), \ldots, \Lambda_N(t)\}$. The augmented system is written as

$$\begin{aligned} \dot{x} &= f(x), \\ \dot{e}_m &= Je_m - \sum_{l \leqslant m} e_l L_{lm} \qquad && m = 1, \ldots, N, \\ \dot{\Lambda}_m &= J_{mm} && m = 1, \ldots, N. \end{aligned} \tag{2.47}$$

It is proven that for an initial point x_0 for which the Lyapunov spectrum exists and $\Lambda(0) = 0$ for stability parameter $\beta > -\lambda_N$ for almost any initial frame $E(0)$ the evolution of (2.47) gives the Lyapunov spectrum

$$\lim_{t \to \infty} \frac{1}{t} \Lambda_m(t) = \lambda_m \quad m = 1, \ldots, N. \tag{2.48}$$

In this way, one can obtain the Lyapunov spectrum by integrating the augmented system (2.47). It is also possible to apply the method for an orthonormal frame with a dimension smaller than the system's dimension whether or not the complete spectrum is needed.

3

Mode Locking in Systems of Globally-Coupled Phase Oscillators

"Science may be described as the art of systematic oversimplification."

– Karl Raimund Popper, *The Logic of Scientific Discovery*

3.1 Globally-Coupled Phase Oscillators with Equidistant Natural Frequencies

In this section, the basic phase oscillator system in which mode-locked solutions are observed is introduced and important quantities to classify solution types are presented. Analogous to the mode-locking phenomenon in optics, a global interaction is considered that is of the Kuramoto-Daido type (2.19). The second crucial ingredient of mode-locking phenomenon will be a set of equidistant natural frequencies, a so-called *frequency comb*.

The basic system which exhibits mode-locked solutions is given by

$$\dot{\theta}_k = \omega_k + \frac{K}{N} \sum_{j=-n}^{n} \left[\gamma \sin(\theta_j - \theta_k) + (1-\gamma)\sin(2(\theta_j - \theta_k))\right], \tag{3.1}$$

where $N = 2n + 1$ is the number of oscillators, $k \in \{-n, \ldots, n\}$ is the oscillator index, $K \in \mathbb{R}_0^+$ the coupling strength, and $\gamma \in [0, 1]$ is a balancing factor that is used to vary the relative strength of the two harmonic interaction terms. Note that the Kuramoto model is obtained by setting $\gamma = 1$. The

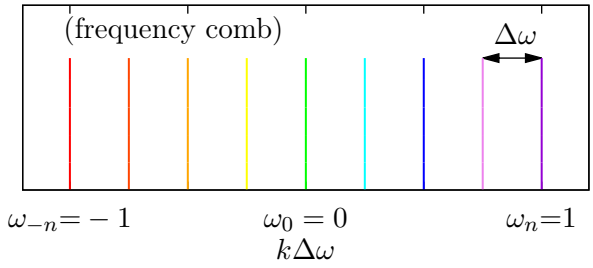

Figure 3.1: Illustration of an equidistant comb of natural frequencies with ($N = 9$) in (3.2).

natural frequencies ω_k are chosen to form an exactly equidistant frequency comb as depicted in Fig. 3.1.

$$\omega_k = k\Delta\omega, \tag{3.2}$$

with the frequency spacing $\Delta\omega$, which gives a set of different but commensurable natural frequencies. The equidistant frequencies are considered to be normalized to the interval $[-1, 1]$ such that the smallest and largest natural frequencies are -1 and 1, respectively. With this normalization, the spacing between the natural frequencies becomes $\Delta\omega = 2/(N-1) = 1/n$. Normalizing the natural frequencies in this way fixates for which parameter values the different types of solutions can be found. This is highly desirable when studying the systems with a varying number of oscillators, because regions where mode-locked solutions appear will also coincide. Note that the restriction to an odd number of oscillators has no significant implications on the mode-locking phenomenon.

To support the self-organized mode locking, it turns out to be important to include higher Fourier harmonics of the interaction. In terms of the general Kuramoto-Daido model (2.19), the model considered (3.1) is a minimal extension that besides $h_1^{(s)} \neq 0$ only includes $h_2^{(s)} \neq 0$. This is interesting because the interaction functions obtained in phase models often include higher harmonics, e.g. the aforementioned phase-reduced model of weakly coupled Hodgkin-Huxley neurons [21]. Note that the theory developed by Daido describing the synchronization threshold only holds for $N \to \infty$ and $\gamma \approx 1$. Regarding the specific interaction function with the first two harmonics, recent results show that the evolution of the order parameter can be found on a corresponding center manifold [58]. For the specific interaction function with two harmonics, one can rewrite the model (3.1) using Daido's first and

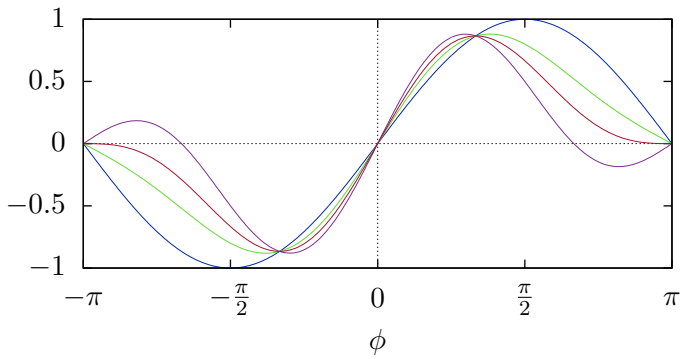

Figure 3.2: Interaction between two oscillators at phase difference ϕ given by the interaction function (3.4). Several balancing values are shown in the corresponding colors $\gamma = 1, \frac{4}{5}, \frac{2}{3}, \frac{1}{2}$. For $1 > \gamma \geqslant 2/3$ the interaction is strictly attractive, whereas for $\gamma < 2/3$ it becomes repulsive for $|\phi \mod \pi| \approx \pi$.

second complex order parameter (2.22) to obtain

$$\dot{\theta}_k = \omega_k - K\left[R_1\gamma\sin(\theta_k - \Psi_1) + R_2(1-\gamma)\sin(2\theta_k - \Psi_2)\right]. \tag{3.3}$$

The shape of the interaction function

The parameter $\gamma \in [0, 1]$ is used to balance between the strength of the two harmonics in the interaction function

$$f(\phi) = \gamma\sin(\phi) + (1-\gamma)\sin(2\phi), \tag{3.4}$$

where $\phi = \theta_k - \theta_j$ denotes the phase difference between two oscillators with arbitrary indices $j, k \in \{-n, \ldots, n\}$. The dependence of the shape of the interaction function on γ is illustrated in Fig. 3.2. For $1 > \gamma \geqslant 2/3$, the interaction between two oscillators is purely attractive, while for values $\gamma < 2/3$, regions of repulsive interaction appear for $|\phi \mod \pi| \approx \pi$. Before the interaction becomes repulsive, decreasing γ has the effect of weakening the interaction for oscillators that are separated by distances of $|\phi \mod \pi| \approx \pi$. This behavior can be understood as a localization of the interaction in the sense that when the phases are relatively close to each other their attraction is stronger.

3.1.1 System and Solution Symmetries

The system has a phase shift symmetry such that a constant phase added to all oscillators does not affect the dynamics. In principle, the system can be

regarded in phase differences which alleviates the phase shift symmetry

$$\phi_k = \theta_k - \theta_0 \quad \text{for all} \quad k \in \{-n, \dots, n\}, \tag{3.5}$$

where ϕ_0 becomes trivial and can be discarded. This leaves an $N-1$-dimensional system in phase differences which reads

$$\dot{\phi}_k = \omega_k + \frac{K}{N} \sum_{j=-n}^{n} \left[f(\phi_j - \phi_k) - f(\phi_j) \right], \tag{3.6}$$

where $f(\cdot)$ is the interaction function (3.4), cf. Fig. 3.2.

Due to the symmetry of the natural frequencies $\omega_k = -\omega_{-k}$, the system is equivariant with respect to

$$\sigma : \theta_k \to -\theta_{-k} \quad \text{for all} \quad k \in \{-n, \dots, n\}. \tag{3.7}$$

This means that an n-dimensional invariant torus exists, whose stability properties have been investigated using renormalization group methods under certain non-resonance conditions for the natural frequencies in the regime $K \to 0$ [59]. To show the systems equivariance under (3.7), it is sufficient to test it for the sum of the first harmonic interactions for the right hand side of one oscillator

$$\sigma \left(\frac{K}{N} \sum_{j=-n}^{n} \gamma \sin(\theta_j - \theta_k) \right) = \frac{K}{N} \sum_{j=-n}^{n} \gamma \sin(\sigma(\theta_j) - \sigma(\theta_k)). \tag{3.8}$$

Evaluating σ for both sides and omitting the constant factors results in

$$-\sum_{j=-n}^{n} \sin(\theta_{-j} - \theta_{-k}) = \sum_{j=-n}^{n} \sin(-\theta_{-j} + \theta_{-k}). \tag{3.9}$$

The symmetry invariant subspace includes all solutions of the form

$$\phi_k(t) = -\phi_{-k}(t) \quad \text{for all} \quad k \in \{1, \dots, n\}, \tag{3.10}$$

where $\phi_k = \theta_k - \theta_0$ is the phase difference with respect to the central oscillator. The distance χ to this symmetry invariant manifold can be monitored in order to detect symmetry breaking bifurcation

$$\chi = \frac{1}{n} \sqrt{\sum_{k=1}^{n} (\phi_k + \phi_{-k})^2}. \tag{3.11}$$

3.1.2 Effective Frequencies and Effective Frequency Combs

Assuming that the following limits exist, one may define the average or *effective frequencies* as

$$\Omega_k := \lim_{t\to\infty} \frac{1}{t} \int_0^t \dot{\theta}_k(\tau) d\tau = \lim_{t\to\infty} \frac{\theta_k(t) - \theta_k(0)}{t}, \tag{3.12}$$

where in (3.12), each phase is considered on the universal cover of the circle $\theta_k \in \mathbb{R}$. In the case of a periodic solution, one can instead take the average over a single period, where it is clear that the effective frequencies are mutually commensurable. Furthermore, the *effective relative frequencies* are defined as

$$\Omega_{k,j} := \Omega_k - \Omega_j \quad \text{for all} \quad k \neq j. \tag{3.13}$$

Analogous to frequency spacing $\Delta\omega$ in the equidistant comb of natural frequencies (3.2), the nearest neighbor relative-effective frequencies define the *effective frequency spacings*

$$\Omega_{k+1,k} := \Omega_{k+1} - \Omega_k \quad \text{for all} \quad k \in \{-n, \ldots, n-1\}. \tag{3.14}$$

It is possible that the effective frequency spacings also form an equidistant comb

$$\Omega_{k+1,k} = \Delta\Omega \quad \text{for all} \quad k \in \{-n, \ldots, n-1\}. \tag{3.15}$$

3.2 Prototype Mode-Locked Solution

As a first step towards the notion of mode-locked solutions, it is illustrative to present a prototype-pulsed solution for a system of uncoupled rotators $\dot{\theta}_k = \omega_k$, which means $(K = 0)$ in (3.1). For these free rotators, it is clear that due to the resonantly chosen natural frequencies (3.2), all possible solutions are periodic with period $T = 2\pi/\Delta\omega$. Note that all of these periodic solutions are neutrally stable with respect to perturbations of the phases. The evolution of the order parameters is explicitly given by

$$\eta_q(t) = \frac{1}{N} \sum_{j=-n}^{n} e^{iq(\theta_j(0) + \Delta\omega j t)}. \tag{3.16}$$

Assuming identical initial conditions, e.g. $\theta_j(0) = 0$ for all j, a prototypical pulsed solution in $R_1(t)$ is realized. The moduli of the order parameters for this initial condition are

$$R_q(t) = \frac{1}{N} \left| \frac{\sin((n + \frac{1}{2})q\Delta\omega t)}{\sin(\frac{q\Delta\omega t}{2})} \right| = \frac{|D_n(q\Delta\omega t)|}{N}, \tag{3.17}$$

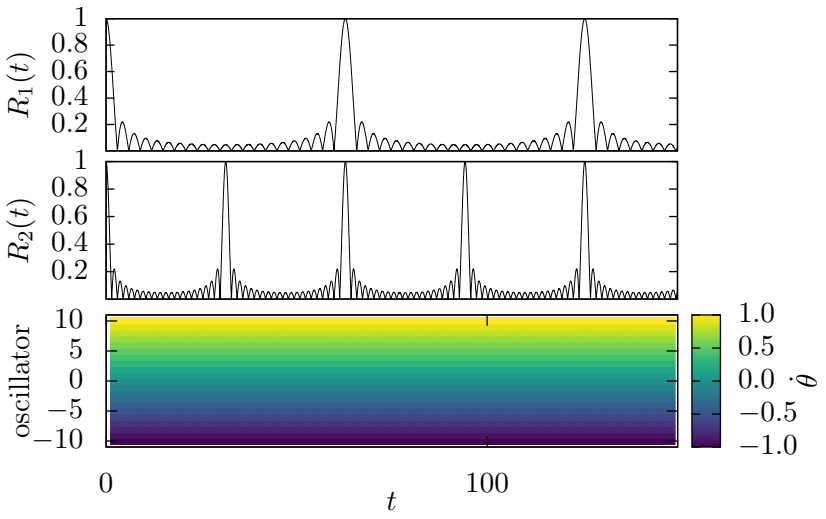

Figure 3.3: The time traces $R_1(t)$ and $R_2(t)$ for the system (3.1) with $N = 21$ and $K = 0$ and identical initial conditions (top and middle panels). The instantaneous frequencies $\dot{\theta}_k = k\Delta\omega$ are presented in color (bottom panel).

where $D_n(\cdot)$ is the Dirichlet kernel of order n and $q \in \{1, 2\}$. The phases of the order parameters $\Psi_1(t)$ and $\Psi_2(t)$ jump between 0 and π whenever $R_1(t) = 0$ or $R_2(t) = 0$, respectively. The time traces $R_1(t)$ and $R_2(t)$ of an example with $N = 21$ oscillators are shown in Fig. 3.3.

The behavior is sensitive to the choice of the initial phases, and moreover for small quenched disorder in the form of a detuning of the natural frequencies, the pulses decay, cf. Fig. 3.4.

A heuristic observation for the prototypical mode-locked solution is that the time-averaged order parameter $\langle R_1(t)\rangle_T = \frac{1}{T}\int_0^T R_1(t)dt$ with period T, is in particular much smaller than $1/\sqrt{2n+1}$ as presented in Fig. 3.5.

3.3 Definitions of Mode-Locked Solutions

3.3.1 Equidistant Mode-Locked Solutions

In general, mode-locked solutions are expected to exhibit the following two characteristics:

i) Recurrent pulses of $R_1(t) \approx 1$ that appear at regular intervals.

ii) The effective frequencies form a comb.

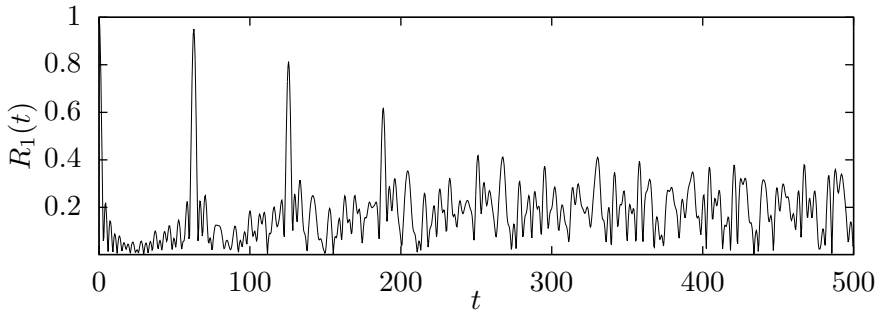

Figure 3.4: Disappearance of the pulses for slightly detuned natural frequencies $\omega_k = k\Delta\omega + D\zeta_k$, where $\zeta_k \in [-1, 1]$ are independent uniform random numbers and $D = 0.01$ is the amplitude of the detuning.

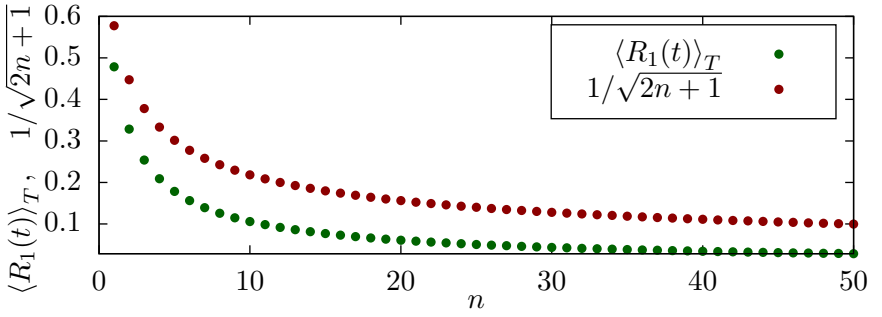

Figure 3.5: The averaged value $\langle R_1(t)\rangle_T$ of the prototypical mode-locked solution obtained by numerical integration of (3.17) is shown to differ significantly from $1/\sqrt{2n+1}$.

To distinguish between the various types of mode-locked solutions that have been discovered in this work, we start by defining the most basic solution which is called an *equidistant mode-locked solution.*

Definition 1. *An equidistant mode-locked solution is a periodic solution of period T such that*

$$\Omega_k = \left\langle \dot{\theta}_k(t) \right\rangle_T = k\Delta\Omega \quad \text{for all} \quad k \in \{-n, \ldots, n\}, \tag{3.18}$$

where $\Delta\Omega \neq 0$ is the spacing of the resulting equidistant effective frequency comb. Furthermore, the number of distinct pulses p within one complete period is defined as the number of Poincaré events for any of the sections given by

$$\theta_k - \theta_{k+1} = 0 \quad \text{for all} \quad k \in \{-n, \ldots, n-1\}. \tag{3.19}$$

The pulse peaks are then defined as the p largest occurrences in the time trace $R_1(t)$ for $t \in [t_0, t_0 + T]$. In the case of $(p > 1)$, the solution is called modulated. The period of the solution is $T = p2\pi/\Delta\Omega$.

For an equidistant mode-locked solution, the effective frequency spacings are of the form (3.15), and because of $\Delta\Omega \neq 0$ the following *no entrainment condition* holds

$$\Omega_{k,j} = \Omega_k - \Omega_j \neq 0 \quad \text{for all} \quad k \neq j. \tag{3.20}$$

This type of mode-locked solution is intuitively the one that is most expected due to the choice of equidistant natural frequencies.

3.3.2 Harmonic Mode-Locked Solutions

The equidistant mode-locked solution can be understood as an example of the more general class of so called *harmonic mode-locked solutions.*

Definition 2. *A harmonic mode-locked solution is a periodic solution of period T such that the effective frequency spacings* (3.14) *are*

$$\Omega_{k+1,k} \in \{\Delta\Omega_j\}_{j\in\{1,\ldots,s\}} \quad \text{for all} \quad k \in \{-n, \ldots, n-1\}, \tag{3.21}$$

where $\{\Delta\Omega_j\}_j$ is ordered and s is the number of different non-zero spacings that are all integer multiple of $\Delta\Omega_1$

$$\Delta\Omega_j = r_j \Delta\Omega_1 \quad \text{for all} \quad j \in \{1, \ldots, s\}, \tag{3.22}$$

where $r_j \in \mathbb{N}_{>0}$. Furthermore, let $\{p_k\}_k$ be the numbers of Poincaré events within one complete period for the sections given by

$$\theta_k - \theta_{k+1} = 0 \quad \text{for all} \quad k \in \{-n, \ldots, n-1\}. \tag{3.23}$$

The number of pulses p is defined via the maximal number of counts

$$p := \max_k \sum_{j=-n}^{n-1} \delta_{p_j p_k}, \tag{3.24}$$

where $\delta_{p_j p_k}$ is the Kronecker delta. The pulse peaks are then defined as the p largest occurrences in the time trace $R_1(t)$ for $t \in [t_0, t_0 + T]$.

3.3.3 Subharmonic Mode-Locked Solutions

In addition to harmonic effective frequency combs, there is the possibility to obtain pulsed periodic solutions with a *subharmonic effective frequency comb*. Subharmonic refers to the fact that different rationally-related effective frequency spacings appear in the comb.

Definition 3. *A subharmonic mode-locked solution is a periodic solution of period T such that the effective frequency spacings* (3.14) *are*

$$\Omega_{k+1,k} \in \{\Delta\Omega_j\}_{j\in\{1,\dots,s\}} \quad \text{for all} \quad k \in \{-n, \dots, n-1\}, \tag{3.25}$$

where $\{\Delta\Omega_j\}_j$ is ordered and s is the number of different non-zero spacings. The spacings are rationally related

$$\Delta\Omega_j = r_j \Delta\Omega_1 \quad \text{for all} \quad j \in \{2, \dots, s\}, \tag{3.26}$$

where $1 < r_j \in \mathbb{Q}$ and there is at least one j such that $r_j \notin \mathbb{N}$. Furthermore, let $\{p_k\}_k$ be the numbers of Poincaré events within one complete period for the sections given by

$$\theta_k - \theta_{k+1} = 0 \quad \text{for all} \quad k \in \{-n, \dots, n-1\}. \tag{3.27}$$

The number of pulses p is defined via the maximal number of counts

$$p := \max_k \sum_{j=-n}^{n-1} \delta_{p_j p_k}, \tag{3.28}$$

where $\delta_{p_j p_k}$ is the Kronecker delta. The pulse peaks are then defined as the p largest occurrences in the time trace $R_1(t)$ for $t \in [t_0, t_0 + T]$.

Lemma 3.3.1. *Subharmonic mode-locked solutions of the type Def. 3 are modulated ($p > 1$).*

Proof. Assuming a solution of type Def. 3 with period T and w.l.o.g. $s = 2$. From (3.28) it follows that if $p_k > 1$ for all $k \in \{-n, \ldots, n-1\} \implies p > 1$. Periodicity demands that $\int_0^T \Omega_{k+1,k} dt = p_k 2\pi$. Take $k_1, k_2 \in \{-n, \ldots, n-1\}$, $k_1 \neq k_2$ with $\Omega_{k_1+1,k_1} = \Delta\Omega_1$, $\Omega_{k_2+1,k_2} = \Delta\Omega_2$ and $\Delta\Omega_1 < \Delta\Omega_2$. If now $p_{k_2} = 1 \implies \int_0^T \Omega_{k_1+1,k_1} dt < \int_0^T \Omega_{k_2+1,k_2} dt = 2\pi$ one finds a contradiction with periodicity. Further, one has $\Delta\Omega_2 = r_2 \Delta\Omega_1$ with $1 < r_2 \in \mathbb{Q}\backslash\mathbb{N}$, therefore $p_{k_1} = 1$ implies the contradiction $2\pi = \int_0^T \Omega_1 dt = \int_0^T \Omega_2 / r_2 dt \neq 2\pi$. □

3.4 Self-Organization of Mode-Locked Solutions

In the following, it is shown how the global coupling scheme of (3.1) is able to stabilize pulsed solutions and even enables their self-organized appearance is presented, which is facilitated by the second harmonic interaction term ($\gamma < 1$). The results presented here were partially published in [60].

3.4.1 Mode Locking in the Kuramoto Model with Equidistant Natural Frequencies

The most basic form of global interaction in the model is achieved by setting $\gamma = 1$, which corresponds to the coupling of the Kuramoto model. In the following details on mode-locked solutions for systems with Kuramoto-type coupling are presented, and the basic mechanism of stabilization of the pulsed periodic order parameter is described. The critical coupling strength of the synchronization transition at K_C for finite-size systems with equidistant natural frequencies and Kuramoto-type coupling has been established in [25], giving an upper bound for the coupling strength up to which mode-locked solutions can potentially be found ($0 \leqslant K < K_C$).

Destabilization of pulses by small coupling

A natural starting point to look for stable mode-locked solutions is the regime of small coupling $K \approx 0$. However, by starting from identical initial conditions, no stable pulsed solutions could be obtained in the small coupling regime. Note that since the presented prototypical solution (3.17) is a non-hyperbolic periodic orbit, there is no guarantee that for small coupling similar stable periodic solutions are to be found. The scenario in mind is that of locking cones connected to $K = 0$ for exactly resonant natural frequencies, inside of which stable pulsed solutions exist. Although the scenario described is intuitive, no stable pulsed solutions could be found in the small coupling regime.

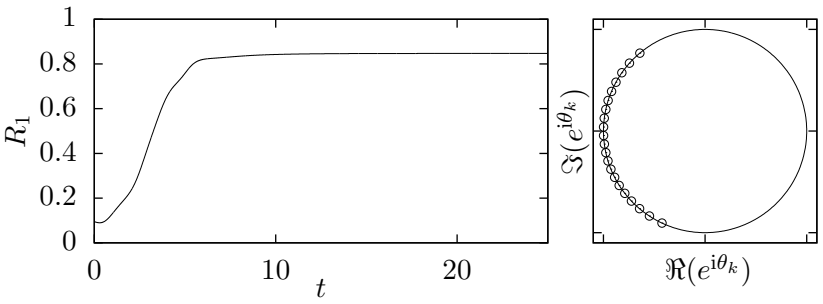

Figure 3.6: Approach to the symmetric synchronous solution for $K = 1.4 > K_C \approx 1.313$ and the final system state projected in the complex plane. The final state is a good initial condition to find mode-locked solutions.

Preparation of initial conditions for mode locking

While for $K \approx 0$ no stable pulsed solutions could be obtained, in the intermediate coupling regime $0 \leqslant K < K_C$, mode-locked solutions are found that conform to different previously-defined types. In order to obtain mode-locked solutions for a system with Kuramoto-type coupling ($\gamma = 1$) one has to prepared the initial conditions carefully. Even all-identical initial conditions, which seems like a natural first attempt, are often insufficient to reach a stable mode-locked solution. A second attempt, which turns out to be a good general choice, is to set $K \gtrsim K_C$ and obtain a symmetric synchronized solution as an initial condition. An example of this type of initial condition is presented in Fig. 3.6.

The initial conditions are then taken for different values of the coupling strength K to find regions of stable mode locking. After the passage of an initial transient, the maximal value in the time trace of $R_1(t)$ and its average $\langle R_1(t)\rangle_t$ are computed, from which the mode-locked solutions can be identified, cf. Fig. 3.7. The figure shows three characteristically different regions which are comprised of synchronized solutions, incoherence, and mode-locked solutions.

For synchronous solutions, which are found at large coupling strength values, $R_1(t) = const.$ such that $\langle R_1(t)\rangle_t = \max_t R_1(t)$. Mode-locked solutions on the other hand exhibit very large pulse peaks, where the largest peak corresponds to $\max_t R_1(t) \approx 1$, while the time-averaged coherence radius $\langle R_1(t)\rangle_t$ is very small. The small value of $\langle R_1(t)\rangle_t$ is characteristic for mode-locked solutions, as it was mentioned in the discussion of the prototype solution, cf. Fig. 3.5. The averaged coherence radius is especially useful to quickly distinguish between incoherence and mode-locking. For a mode-locked so-

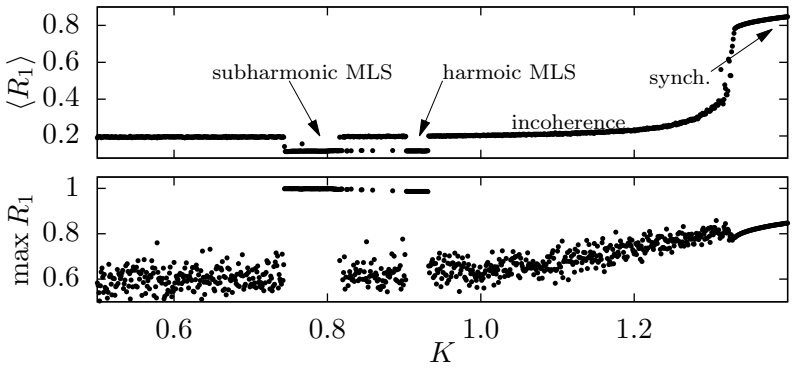

Figure 3.7: Starting from initial conditions Fig. 3.6, the time traces $R_1(t)$ are processed for different coupling strength K for fixed system size $N = 21$. The quantities $\max_t R_1(t)$ and $\langle R_1(t) \rangle_t$ are plotted and two disconnected regions of different types of mode-locked solutions are found in the central region where the harmonic solution is in particular of the equidistant type Def. 1.

lution, the averaged fluctuations are suppressed, meaning that $\langle R_1(t) \rangle_t$ is significantly smaller than in the case of incoherent solutions.

A similar investigation for different system size $N \in \{51, 71, 91\}$ shows that the qualitative picture does not change when the number of oscillators is increased, cf. Fig. 3.8. The noticeable difference is that the regions of subharmonic and harmonic mode-locked solutions are now forming one connected plateau such that they are bordering each other.

Equidistant mode-locked solution in the Kuramoto model

The harmonic mode-locked solutions indicated in Fig. 3.7 are of the equidistant type and fulfill Def. 1. One example at coupling strength $K = 0.91$ and $N = 21$ is presented in Fig. 3.9. The left panels show the time traces $R_1(t)$ and $R_2(t)$. At the pulse peaks, the interaction is particularly strong $\max_t R_1(t) \approx 1$ and all phases are pulled towards the mean phase. This is also visible in the bottom panel where the instantaneous angular velocities $\dot{\theta}_k$ for all oscillators are plotted over time in form of a color map. At the occurrences of the pulses, the instantaneous velocities change significantly, resulting in a reorganization that stabilizes the mode-locked solution. In between the pulses, the oscillators evolve with angular velocities close to their natural frequency. The effective frequency spacing $\Delta\Omega$ is smaller than the spacing of the natural frequencies $\Delta\omega$ such that the period increases by the nonlinear interaction.

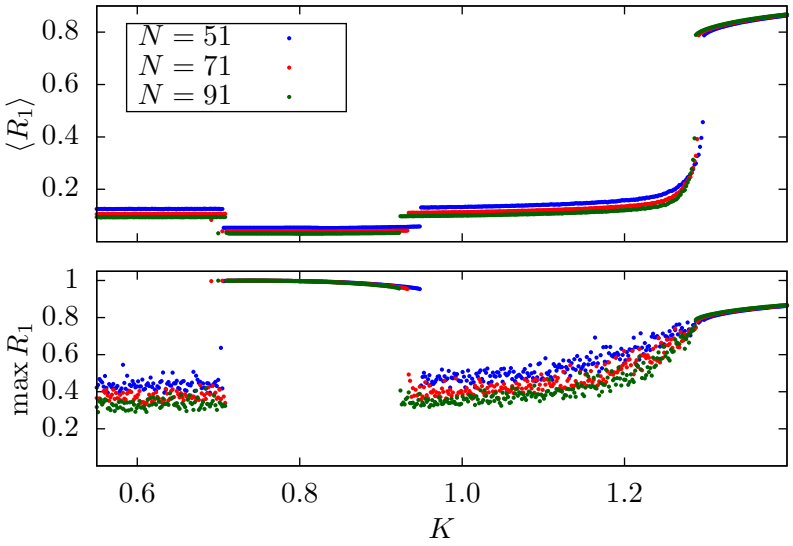

Figure 3.8: Starting from synchronous initial conditions similar to Fig. 3.6, the time traces $R_1(t)$ are processed for different coupling strength K and different system size $N \in \{51, 71, 91\}$. The quantities $\max_t R_1(t)$ and $\langle R_1(t) \rangle_t$ are plotted, revealing a long plateau of of harmonic and subharmonic mode-locked solutions that border each other.

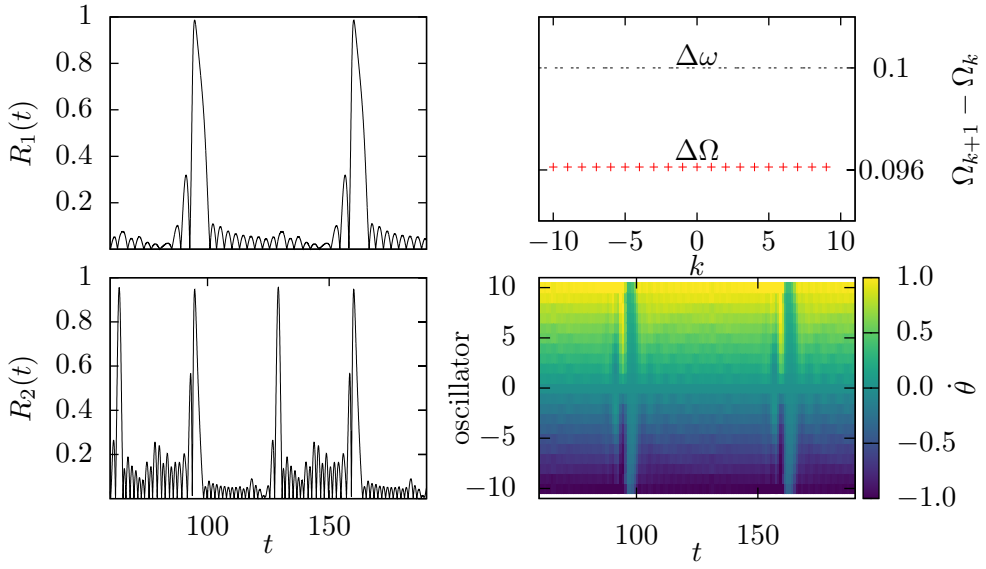

Figure 3.9: Time traces $R_1(t)$ and $R_2(t)$ for an equidistant mode-locked solution of the system with $(K, \gamma) = (0.91, 1)$ and $N = 21$ (left). The compressed effective frequency spacings ($\Delta\Omega < \Delta\omega$) and the instantaneous phase velocities $\dot{\theta}_k$ (right).

Subharmonic mode-locked solution in the Kuramoto model

In addition to the equidistant mode-locked solution, subharmonic mode-locked solutions of type Def. 3 are obtained at lower values of K in Fig. 3.7. This solution type exhibits a more intricate relationship between the effective frequencies and frequency spacings. It is shown in lemma 3.3.1 that these solutions are always modulated, meaning that the inter-pulse intervals and the magnitudes of the pulse peaks vary. In the simplest case of a subharmonic mode-locked solution that is also the one found here, one has two different effective frequency spacings such that

$$\Omega_{k+1,k} \in \{\Delta\Omega_1, \Delta\Omega_2\} \quad \text{for all} \quad k \in \{-n, \ldots, n-1\}. \tag{3.29}$$

In the example for $K = 0.765$ that is shown in Fig. 3.10, the two spacings fulfill a rational relation $\Delta\Omega_1/\Delta\Omega_2 = 7/8$ and the period is given by $T = 2\pi 8/\Delta\Omega_1 = 2\pi 7/\Delta\Omega_2$. During one complete period, the sections given by (3.27) are counted $p_k = 8$ for $k \in \{-n+1, \ldots, n-2\}$ and $p_k = 7$ for $k \in \{-n, n-1\}$ times. This means that the solution has $p = 8$ distinct pulses, which are also visible in the time trace $R_1(t)$ in Fig. 3.10 (a). In the plot of the effective frequency spacings, cf. Fig. 3.10 (c), one sees that the spacings on the edges are different from the rest.

Although it is conceivable to obtain effective frequency combs with more than two different spacings, the commonly observed subharmonic solutions for equidistant natural frequencies are of the form (3.29). In panel (b), the return times T_ν are plotted against the next return times $T_{\nu+1}$ for the section $\theta_{-n} - \theta_{-n+1} = 0$. For another section, e.g. $\theta_{-n+1} - \theta_{-n+2} = 0$, additional crossings would be observed in the $(T_\nu, T_{\nu+1})$-plane.

Performing parameter scans for the system in order to explore bifurcations of the solutions is especially difficult for mode-locked solutions with Kuramoto-type coupling due to a high sensitivity of the solution to finite size perturbations. The origin of the high sensitivity of the mode-locked solutions comes from the strong variation of the interaction at the pulses and between them. Due to this peculiar property of the solutions, the exact time when the change of the parameter is applied matters and can lead to a divergence from the periodic solution.

To perform the parameter scan, the previously described approach of the slow adaptation of a parameter (2.41) is applied. In this way, one is able to perform a dynamical continuation of the solution and discover bifurcations of the stable mode-locked solutions. The subharmonic mode-locked solution shown in Fig. 3.10 is investigated in a parameter scan for increasing coupling strength, cf. Fig. 3.11. While the initial subharmonic solution shows $p_{-n} = 7$ crossings of the Poincaré section, see Fig. 3.10 (b), the solution undergoes a

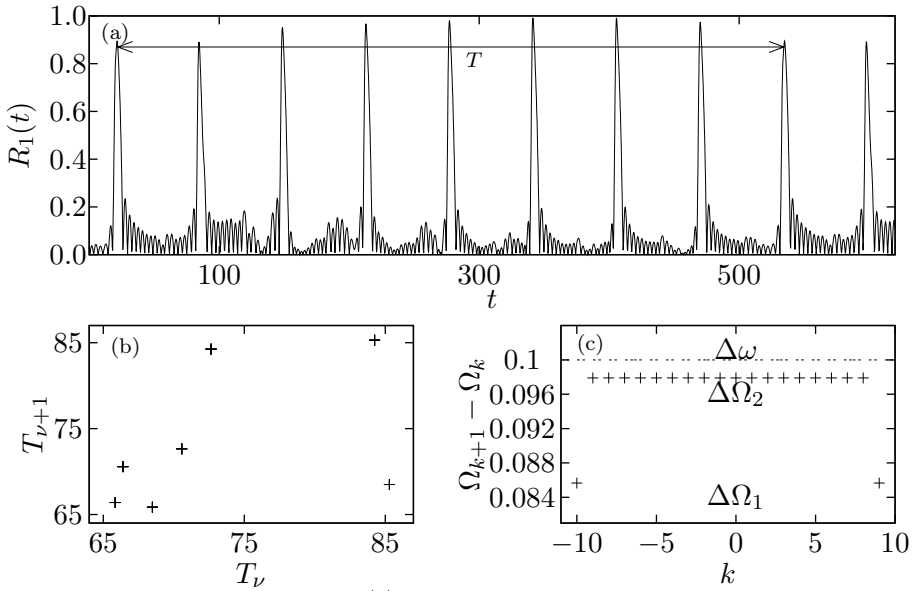

Figure 3.10: The time trace $R_1(t)$ of the subharmonic mode-locked solution for $(K, \gamma) = (0.765, 1)$ and $N = 21$, in panel (a). The return times T_ν and next return times $T_{\nu+1}$ to the section $\theta_{-n} - \theta_{-n+1} = 0$ are shown in (b). The effective frequency spacings presented in (c) are of the subharmonic type conforming to Def. 3, with two different spacings $s = 2$ in (3.25).

period tripling giving $p_{-n} = 21$ and a consecutive period doubling $p_{-n} = 42$, before phase turbulence emerges. In Fig. 3.11 (a), a zoom in on one of the crossings is shown starting shortly before the period tripling occurs. Note that after the period doubling occurs (green) the total period of the solution is already of order $\mathcal{O}(10^3)$. In the panels (b) and (c) of Fig. 3.11, one representative of all of the different solutions is shown in a 2-dimensional plot of $T_{\nu+1}$ against T_ν.

Even though the parameter increments are already small $\Delta_p = 10^{-7}$, adapting the parameter at a random moment of the periodic orbit frequently destabilizes the solution and one observes phase turbulence to appear for different coupling strength values. By employing the slow adaptation procedure (2.41), one is able to observe the bifurcations and dynamically follow the stable mode-locked solutions. The time interval of the adaptation scheme used for the simulation presented in Fig. 3.11 is $t_{\text{ad}} = 25 \cdot 10^3$ with the time step size $h = 0.01$, resulting in an increment of $4.0 \cdot 10^{-14}$ at each time step during the adaptation interval.

Beyond the presented periodic mode-locked solutions that already have a complicated structure, low-dimensional chaotic attractors that support solutions with comparable properties exist. Examples of such solutions are

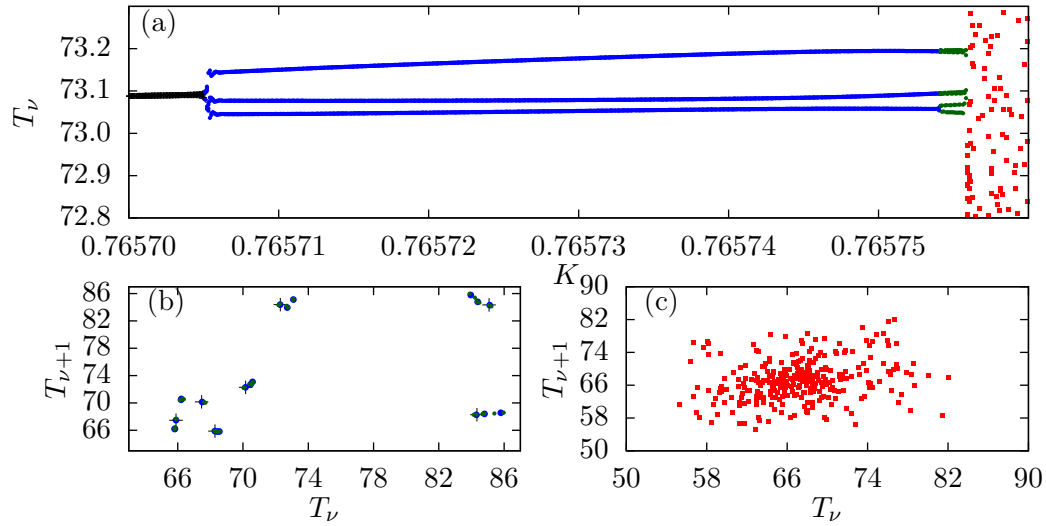

Figure 3.11: The top panel shows a parameter scan for increasing K starting from the solution Fig. 3.10. In particular, it is only a zoom into the vicinity of one of the seven different return times. In the bottom panels consecutive return times T_ν and $T_{\nu+1}$ are presented for the different solution types in the color according to the upper panel.

presented for the system, including a second harmonic interaction term because there, the stability properties of the solutions are improved.

Coexistence of mode locking and incoherence in the Kuramoto model

Previous work on finite size Kuramoto models with equidistant natural frequencies and first harmonic coupling function was mostly focused on the desynchronization transition and extensive chaos found below the synchronization threshold [24, 23]. Corresponding extensive Lyapunov spectra are shown in Fig. 3.12. The horizontal axis for the spectra is normalized to the interval $[0, 1]$ to illustrate the extensivity. The extensive spectra can be found for other values of the coupling strength, however, for the parameter values presented, phase turbulence coexists with the equidistant mode-locked solution, cf. Fig. 3.13.

The procedure used to find the mode-locked solutions reveals that there are indeed periodic solutions to be found in the same parameter region where typically extensive Lyapunov spectra are obtained, starting from random initial conditions. For intermediate system sizes, e.g. $N = 21$ presented in Fig. 3.13, one does not usually observe convergence to mode-locked solutions

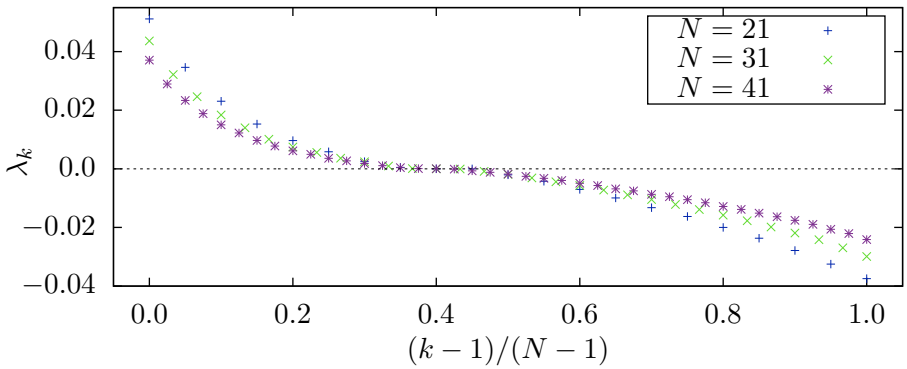

Figure 3.12: Extensive Lyapunov spectra for system sizes $N \in \{21, 31, 41\}$ found from random initial data and $(K, \gamma) = (0.91, 1)$.

starting from random initial data even for simulations as long as 10^7 time units. It is noteworthy that a symmetrization of the effective frequencies seems to occur for long simulation times $\Omega_k = -\Omega_{-k}$. Similarly, the subharmonic mode-locked solution found for $(K, \gamma) = (0.91, 1.0)$, see Fig. 3.10 coexists with phase turbulence. It is not clear whether the phase turbulence in the parameter regions described could be merely long-living chaotic transients. However, in the simulations for many initial conditions, no convergence to a mode-locked solution could be observed.

The coexistence is especially important when parameter scans like the one for the subharmonic mode-locked solutions presented in Fig. 3.11 are performed. Without the described procedure of the slow adaptation of the parameter, mode-locked solutions are often destabilized whereas the system remains in phase turbulence.

3.4.2 Mode locking in the Kuramoto Model with Second Harmonic Interaction

It is interesting that the simple Kuramoto-type coupling ($\gamma = 1$) can stabilize the pulsed solutions starting from initial conditions that are suitably chosen when at the same time, they are difficult to investigate due to their sensitivity to perturbations and the coexistence of phase turbulence. It is clear that when models for specific applications are considered coupling functions with several harmonics are more general, thus it is interesting to go beyond the Kuramoto-type coupling and investigate the effects that more complicated coupling functions have on mode-locked solutions.

In contrast to the coexistence found for the systems with first harmonic coupling, including a second harmonic in the interaction changes the picture

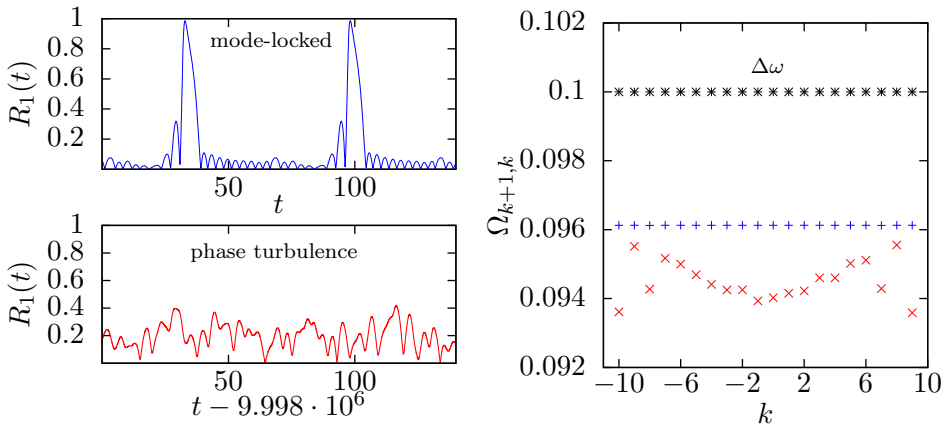

Figure 3.13: Time traces $R_1(t)$ of coexisting solutions for $(K, \gamma) = (0.91, 1)$ and $N = 21$ (left) and the effective frequency spacings in the corresponding colors (right). The effective frequencies for the phase turbulence are computed over an interval of 10^7 time units.

significantly in a way that one achieves self-organization to mode-locked solutions in extended regions of the parameter space (K, γ). By letting $(\gamma < 1)$ in (3.1) the second harmonic coupling is activated and its influence is investigated by varying the balancing parameter γ.

Globally-stable mode-locked solution

With $(\gamma < 1)$, extended regions in parameter space (K, γ) now appear where mode-locked solutions exist and develop from random initial data. Due to self-organized mode locking, the model becomes interesting to study the emergence of the pulsed solutions and explore their relations with phase turbulence. The local stability of the mode-locked solutions that will be discussed in detail reveals a stabilization mechanism that is exclusively attributed to the presence of the second harmonic. For balancing values $\gamma > 2/3$, one often finds unique mode-locked solutions and sometimes solutions that appear as pairs with a broken central mode symmetry (3.10). For $\gamma < 2/3$, on the other hand, one frequently encounters multistability that is supported in particular by the repulsive interaction, cf. Fig. 3.2.

Influence of the second harmonic on the emergence of mode locking

To study the influence of the second harmonic interaction on the emergence of mode-locked solutions, the system is investigated for varying balancing parameter γ. The main question to be addressed here is how the specific values

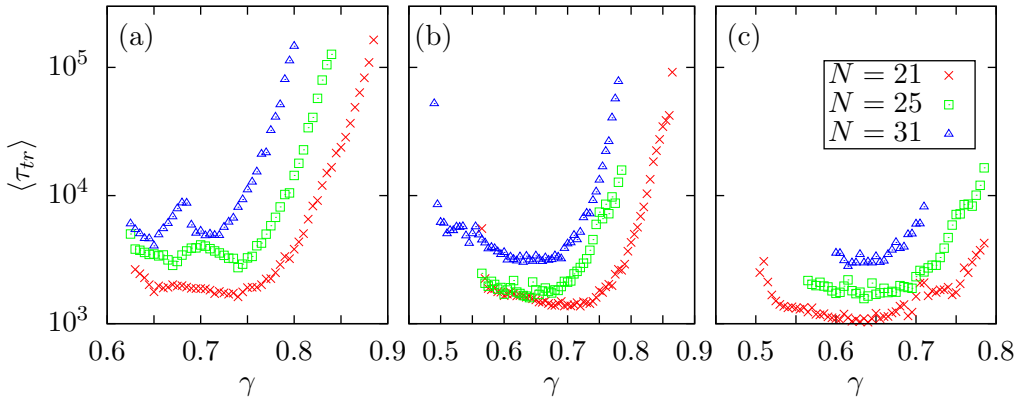

Figure 3.14: The average length of the chaotic transients $\langle \tau_{tr} \rangle$ to a stable mode-locked solution on a logarithmic axis for different γ values. The computations are performed for different system size $N \in \{21, 25, 31\}$ and coupling strength $K \in \{1.2, 1.25, 1.3\}$, panels (a), (b), (c), respectively. Each data point represents an average obtained from 200 random initial conditions with convergence to a mode-locked solution of type Def.1 with $p = 1$ for each initial condition within 10^6 time units.

of γ and N influence the average length of the chaotic transient preceding the mode locking.

For different values of the coupling strength $K \in \{1.2, 1.25, 1.3\}$, system sizes $N \in \{21, 25, 31\}$, and varying γ, the system is initialized 200 times with independent random initial conditions for every γ, after which the resulting transient times are averaged. The averaged transient times $\langle \tau_{tr} \rangle$ are plotted on a logarithmic axis and exhibit drastic growth for increasing γ that has an exponential tendency, cf. Fig. 3.14 (a)–(b). For the presented parameter values in the figure, all tested initial conditions converged to a mode-locked solution of the type Def.1 with $p = 1$ within 10^6 time units. This means the collection of data is stopped for transients that are either too long, or for more complicated mode-locked solutions. For $\gamma < 2/3$, one can see some non-monotonous features that are due to the multistability of many different mode-locked solutions.

An interesting feature regarding the double zero of the interaction function is prominent in (a), where at $\gamma = 2/3$ for $N = 31$ transient times increase and a sharp local maximum appears. In principle, one can also look for general types of pulsed solutions by tracking the rolling average of the order parameter. It is already indicated that a larger number of oscillators tends to give longer average transient times, which will be discussed later on.

Local expansion rates of phase space volumes

To further explore the impact of the second harmonic and the improvement of the stability of the mode-locked solutions, the local expansion rates along periodic solutions for the cases $(K, \gamma) = (0.91, 1)$ and $(K, \gamma) = (1.25, 0.7)$ are compared. The term local rate of expansion refers to the rate of expansion of phase space volume that a small ball of initial conditions around a trajectory experiences according to the linearized flow. Unlike in Hamiltonian systems where according to Liouville's theorem, phase space volume is preserved under the phase flow [61], dissipative dynamical systems can exhibit regions of local contraction or expansion. Since the eigenvalues of the Jacobian matrix J give the local exponential rates of expansion in all eigendirections, the rate of expansion of phase space volume is given as the sum of the eigenvalues which will be presented normalized to the systems dimension

$$\Lambda(t) = \frac{1}{N}\mathrm{tr}\left(J|_{\theta(t)}\right), \tag{3.30}$$

where N is the dimension of the complete phase space and J is the Jacobian matrix which is evaluated at the particular points $\theta(t) \in \mathbb{R}^N$.

As a side note, it is easy to see that since there exists a non-singular matrix P with $PJP^{-1} = M$, where M has Jordan normal form, one also has that $\mathrm{tr}J = \mathrm{tr}M = \sum_{i=1}^{N} \lambda_i$ with λ_i being the eigenvalues of J, which is why the desired quantity is obtained by computing the trace of the Jacobian for each point along a particular solution in (3.30).

A necessary condition for a periodic solution is that $\int_0^T dt\Lambda(t) \leqslant 0$. However, locally, the quantity $\Lambda(t)$ can be alternatingly expanding or contracting even for a stable periodic orbit such as the mode-locked solutions. The time-dependent quantity (3.30) can be used to identify episodes along the orbits where perturbations contract or diverge. Additionally, one can monitor the maximal eigenvalue to assure in case of volume contraction that the contraction is indeed happening in all directions.

For the two stable mode-locked solutions found for $(K, \gamma) = (0.91, 1)$, $(K, \gamma) = (1.25, 0.7)$ and $N = 21$, the normalized rate of expansion $\Lambda(t)$ as well as the maximal instantaneous eigenvalue $\max \lambda_i(t)$ are plotted aside the corresponding time traces of the order parameters, see Fig. 3.15. It is apparent that in both cases, the main contribution to the stabilization of the periodic solution comes from the coherence pulses. By including the second harmonic interaction, the contraction at the time of the coherence pulses is increased due to simultaneous maxima in $R_1(t)$ and $R_2(t)$. Furthermore, the additional maximum in the $R_2(t)$ leads to a contraction of phase space volume that occurs at approximately half the period between the pulses in

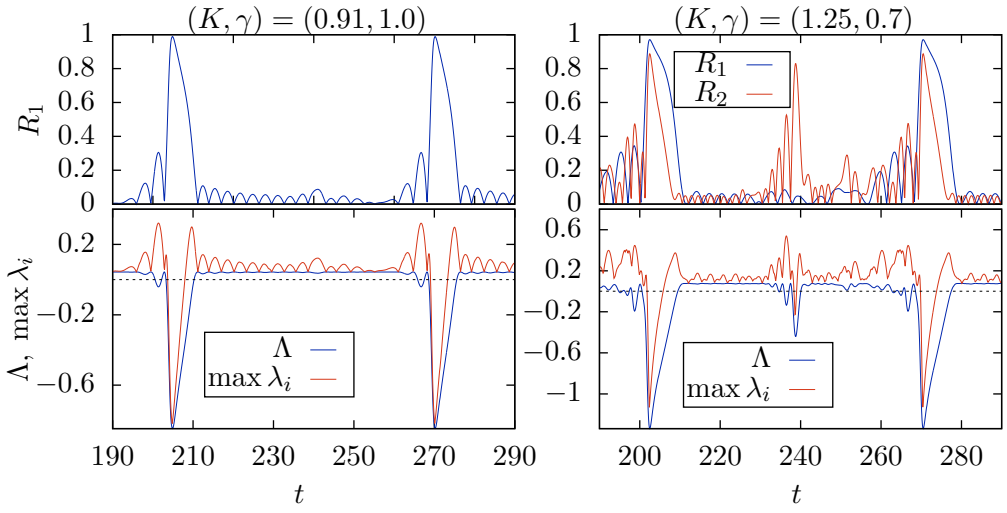

Figure 3.15: The upper panels show the time traces $R_1(t)$ and $R_2(t)$ where for Kuramoto-type coupling (left), the second order parameter has been omitted. On the bottom, the normalized expansion rates of phase space volume $\Lambda(t)$ (3.30) and the maximal instantaneous eigenvalue $\max \lambda_i(t)$ are presented.

$R_1(t)$. For the first harmonic coupling, the volumes are strictly expanded between the coherence pulses. In fact, without the second harmonic, one finds a long plateau with a small and almost constant rate of expansion.

In comparison, the system including the second harmonic interaction exhibits more erratic behavior during the second half of the period. Interestingly, the more erratic fluctuations lead to smaller rates of expansion compared to the constant plateau during the first half of the period. For the second half of the period, it is to be noted that although phase space volumes expand less, the maximal eigenvalue exhibits increase. A close look at the time trace $R_2(t)$ in the second half of the orbit suggests that the decline of the expansion rate is accompanied by an increase in $R_2(t)$, which means that the second harmonic exerts an influence even apart from the pulses. For a larger number of oscillators, the fluctuations of the expansion rate in the second half of the period level off, which is illustrated in Fig. 3.16 for the system $(K, \gamma, N) = (1.25, 0.7, 91)$.

3.5 Bifurcations of Mode-Locked Solutions

This section is concerned with the typical bifurcation scenarios that are observed when K is varied. The previously used approach of a slowly varying

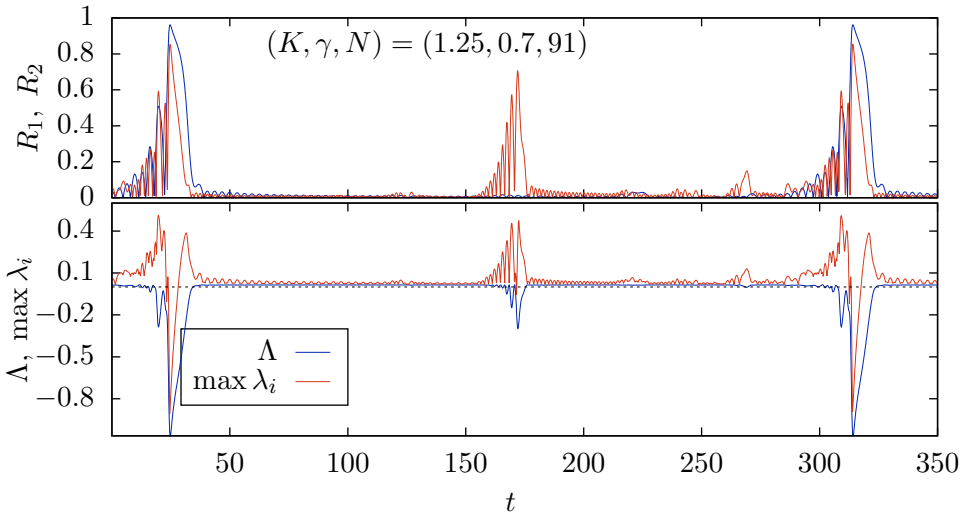

Figure 3.16: Top panels: time traces of the order parameters, for $N = 91$ oscillators. Bottom panel: normalized expansion rates of phase space volume $\Lambda(t)$ (3.30) and the maximal instantaneous eigenvalue $\max \lambda_i(t)$.

parameter (2.41) for the Kuramoto-type coupling $\gamma = 1$ could be used again. However, due to the improved convergence and stability properties of the solutions, it is not necessary. The Poincaré section condition that is used marks the passage of the two fastest oscillators with indices $n - 1$ and n

$$\theta_n - \theta_{n-1} = 0. \tag{3.31}$$

A representative parameter scan performed for varying K at fixed $\gamma = 0.82$ for a system consisting of $N = 21$ oscillators is presented in Fig. 3.17. Therein, times between consecutive section crossings are plotted against the coupling strength and the distance to the symmetry invariant subspace (3.11) at the particular crossings is recorded. The scanning is performed for increasing (blue) and decreasing (orange) parameter values in order to discover multistability. After each parameter change, the system is perturbed in the direction transverse to the symmetry invariant subspace to avoid numerical trapping. In regions where the return times T_ν are vastly scattered, the system is in a state of phase turbulence while in the other regions, one finds several kinds of mode-locked solutions.

The largest periodic window corresponds to equidistant mode-locked solutions according to Def. 1. While most solutions of the branch are invariant under the central mode symmetry (3.7), a period doubled solution with broken symmetry is found that demonstrates a symmetry breaking period doubling for an equidistant mode-locked solution. In this case, the number

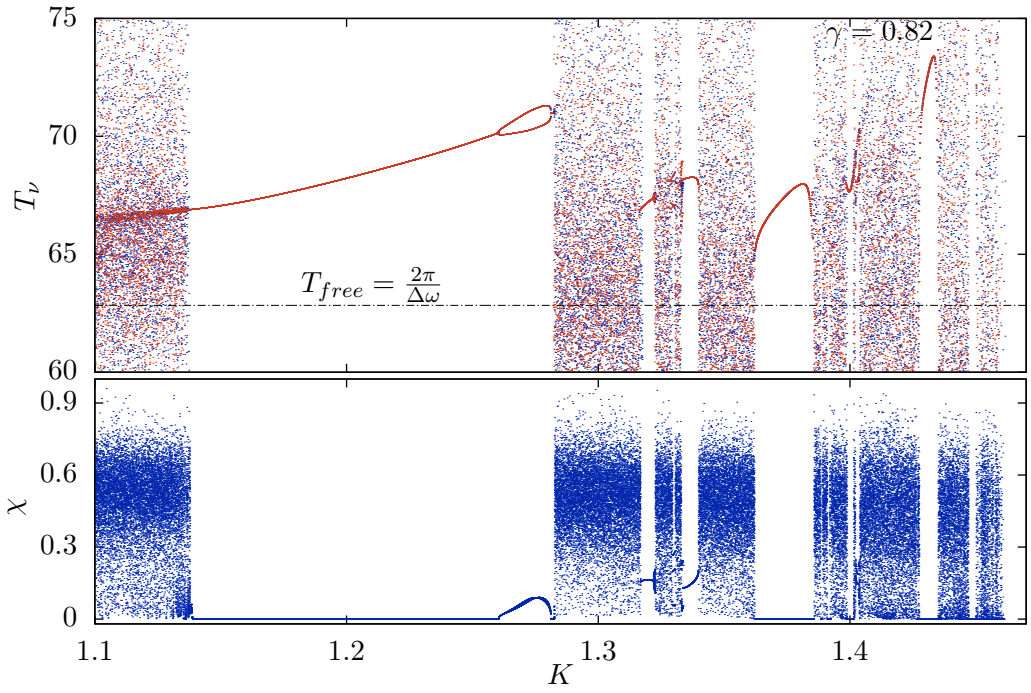

Figure 3.17: Top: consecutive return times T_ν to the Poincaré section; different colors indicate positive (blue) and negative (orange) scanning direction. The dashed line indicates the period of the free rotating oscillators for $K = 0$. Bottom: shows the distance to the invariant subspace with central mode symmetry (3.11).

of distinct pulses increases from $p = 1$ to $p = 2$. The eventual destabilization of the solutions of the central branch will be discussed in detail below.

The stabilization of the mode-locked solutions in the narrow windows for larger coupling strength is attributed to *mode merging*. Mode merging refers to a violation of the no entrainment condition (3.20), such that for some j, the effective spacing becomes zero $\Delta\Omega_j = 0$. Accordingly, this type of solution is called a *merged mode-locked solution*. An example of this type of solution is shown in Fig. 3.18 for $(K, \gamma, N) = (1.38, 0.82, 21)$. The solution lies on the invariant subspace with central mode symmetry (3.11) with $\chi = 0$, which implies that symmetry-related oscillators have merged. In the present example, the oscillators with the indices 2 and 1 as well as -2 and -1 have merged. One observes that the pulse in $R_2(t)$ at half the period between the pulses in $R_1(t)$ has become much less pronounced.

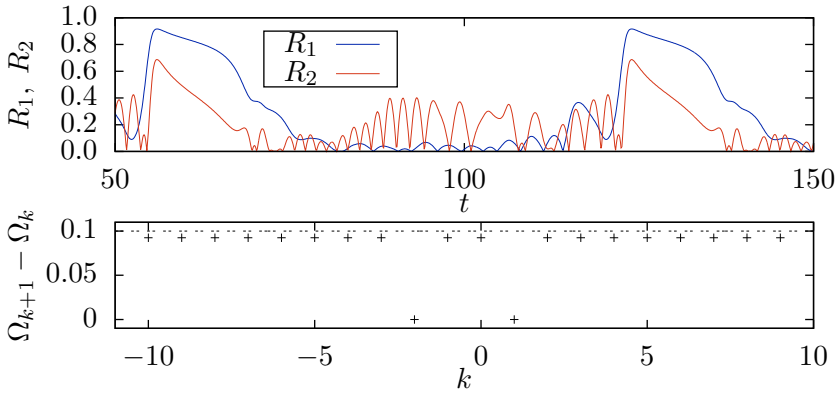

Figure 3.18: Top: time traces of the order parameters of a solution with merged modes for the system $(K, \gamma, N) = (1.38, 0.82, 21)$. Bottom: effective frequency comb spacings where $k \in \{-10, \ldots, 9\}$ and the spacing of the natural frequencies $\Delta\omega$ are represented by the dotted line.

3.5.1 Chaotically-Modulated Solution Through Torus Breakdown

The right stability boundary of the largest mode locking window in Fig. 3.17 is given by a torus bifurcation, where a stable invariant torus of mode-locked solutions emerges. Sampling return times T_ν to the Poincaré section (3.31) for the mode-locked solutions on the torus give closed curves in the two-dimensional representation of T_ν against $T_{\nu+1}$. In the usual way, solutions can be quasiperiodic when the torus is densely covered or periodic when there is locking on the torus. Correspondingly, the solutions exhibit a periodic or quasiperiodic modulation of the pulses.

Definition 4. *An equidistant mode-locked solution on an invariant torus is a solution that exists on an invariant torus with the property that when there is locking on the torus, the solution obeys Def. 1.*

Otherwise, the solution has quasiperiodic modulation and there is an infinite number of distinct pulses. Choosing any one of the Poincaré sections

$$\theta_k - \theta_{k+1} = 0 \quad \text{for all} \quad k \in \{-n, \ldots, n-1\}, \tag{3.32}$$

the return times T_ν and next-return times $T_{\nu+1}$ are on a closed curve in the $(T_\nu, T_{\nu+1})$-plane for all $\nu \in \mathbb{N}$. There is an upper bound T_b to the return times T_ν with $|T_\nu - T_b| < \varepsilon$ for some small ε and the time trace $R_1(t)$ for $t \in [t_0, t_0 + T_b]$ for any t_0 contains at least one pulse, where the pulse peak is defined as the maximal value within the interval.

A close up of the family of mode-locked solutions on an invariant torus for varying K together with a collection of several two-dimensional embeddings in the $(T_\nu, T_{\nu+1})$-plane is presented in Fig. 3.19. Panel (a) shows the parameter scan for increasing and decreasing parameter values in blue and orange, respectively. Vertical colored lines indicate parameter values for which two-dimensional embeddings are supplied in (b)–(c). For small values of the coupling strength, the solutions are of the type Def. 4, see panel (b). Panel (c) shows the two-dimensional representation of the attractor corresponding to the parameter value of the green vertical line, where a low-dimensional chaotic attractor has emerged via torus breakdown. The solution exhibits a chaotic modulation of the pulses that appears as a jittering of the inter-pulse intervals and pulse peaks.

For further increased coupling, the chaotic attractor collapses in an inverse cascade of period doublings to a periodic orbit with five distinct section crossings, which itself exists as a pair of solutions with broken symmetry $\phi(t)$ and $\tilde{\phi}(t)$ that satisfy

$$\phi_k(t) = -\tilde{\phi}_{-k}(t), \quad \text{for all} \;\; k \in \{1, \ldots, n\}, \tag{3.33}$$

with $\phi_k = \theta_k - \theta_0$ and $\tilde{\phi}_k = \tilde{\theta}_k - \tilde{\theta}_0$. In (b), the progressive deformation of the torus can be seen, where as K is increased five distinct folding regions appear along the contour for the largest presented coupling (dark-red). Note that the number of folding regions corresponds to the number of peaks $p = 5$ of the equidistant mode-locked solution that appears after the inverse cascade. Eventually, also the $p = 5$ mode-locked solution loses its stability and an intermittent transition to phase turbulence occurs. The low-dimensional chaotic attractor represented in $(T_\nu, T_{\nu+1}, T_{\nu+2})$ is shown in Fig. 3.20. The Lyapunov spectrum of the attractor has been obtained for a total integration time of $2 \cdot 10^5$ units, cf. Fig. 3.21. One finds one positive Lyapunov exponent as well as two zero exponents, where one is attributed to the time shift along the attractor, i.e. in the longitudinal direction, whereas the second one is due to the phase shift symmetry of the whole solution. The rest of the spectrum has a complicated structure compared to the spectra found for the examples of phase turbulence, which look smooth in comparison, see Fig. 3.12. In particular, one finds in the negative part of the spectrum several pairs of exponents that are identical up to the numerical precision of the procedure. An estimate of the attractor dimension by the Kaplan-York-Formula [62] gives $D_{KY} \approx 3.015$, where the resulting dimension has to be reduced by one in order to account for the phase shift symmetry.

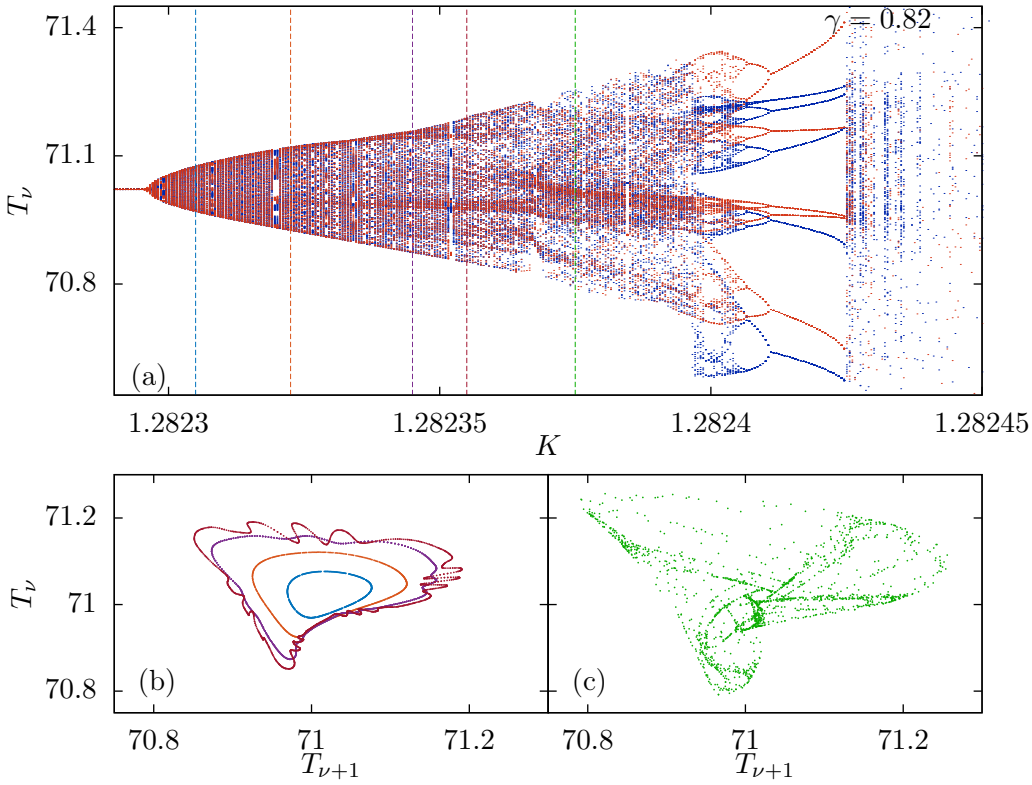

Figure 3.19: Close up into the parameter scan from Fig. 3.17 highlighting the emergence of an invariant torus of equidistant mode-locked solutions (Def. 4). Panel (a): return times T_ν against coupling strength K, increasing and decreasing parameter in blue and orange, respectively. Panel (b)–(c) two-dimensional embeddings T_ν against $T_{\nu+1}$ for the parameter values indicated by the colored vertical lines in (a).

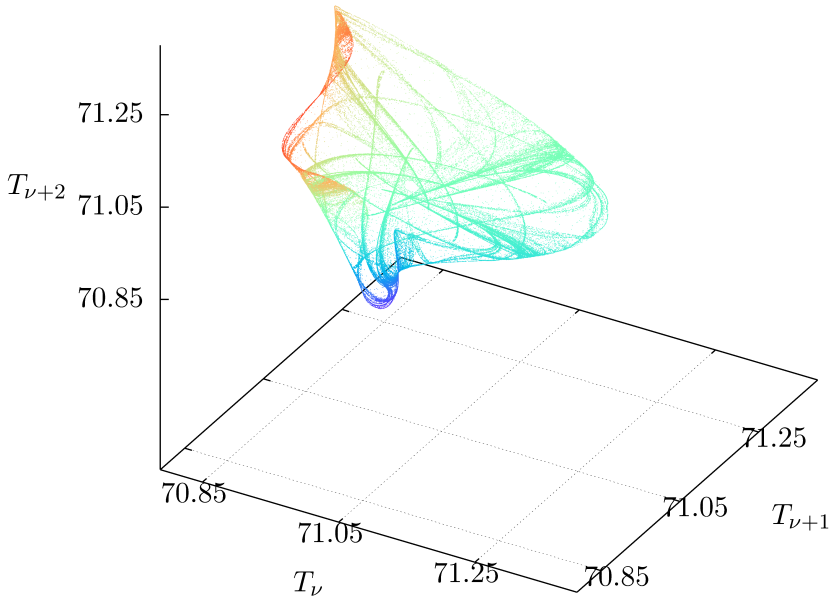

Figure 3.20: Attractor of chaotically-modulated mode-locked solution from Fig. 3.19 (c), for $K = 1.282375$ represented in $(T_\nu, T_{\nu+1}, T_{\nu+2})$, where the height in $T_{\nu+2}$ is also color coded.

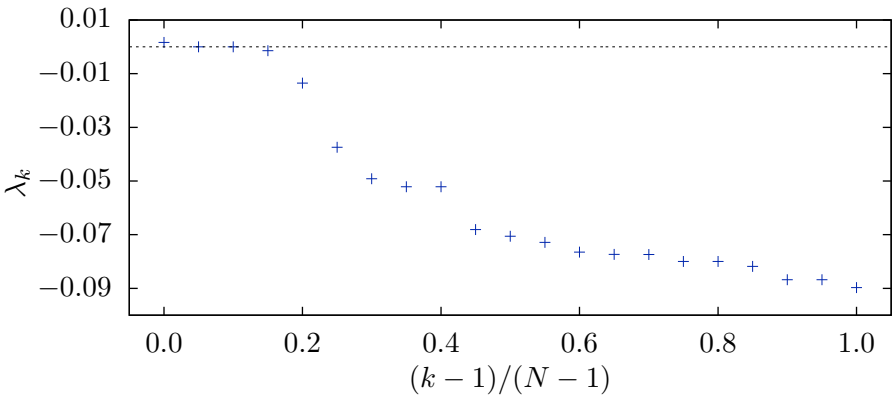

Figure 3.21: Lyapunov spectrum of the chaotic attractor from Fig. 3.20.

3.5.2 Transition to Phase Turbulence Through Intermittency

The connection between regimes of phase turbulence and mode-locked solutions is found to be of an intermittency type. A particularly well suited example to demonstrate this connection is the intermittent transition to phase turbulence that occurs at $K < 1.137 \approx K_b$ in the parameter scan in Fig. 3.17, which is the second stability boundary of the largest mode locking region in the scan. Following the branch of unstable solutions, one sees that where it has become unstable ($K < K_b$), the return times T_ν accumulate around an approximate value of the period of the unstable solution. This corresponds to the intermittent returns to mode locking from episodes of phase turbulence. The intermittent behavior that compares to scenarios described in [63, 64, 65] is due to a weakly unstable mode-locked solution that is recurrently visited after episodes of phase turbulence.

An example of the alternation between phase turbulence and pulsation is illustrated in Fig. 3.22. To identify episodes of pulsing behavior where the system is close to the unstable mode locking, one can use the rolling average of $R_1(t)$, which is plotted in red in Fig. 3.22. The length T of the time window over which the rolling average is computed should be close to the approximate inter-pulse interval of the underlying unstable mode-locked solution

$$\langle R_1(t) \rangle_T = \frac{1}{T} \int_{t-T}^{t} R_1(\tau) d\tau. \tag{3.34}$$

For a varying distance from the bifurcation point $K_b \approx 1.137$, the average length of the mode locking episodes $\langle \tau_{\mathrm{ML}} \rangle$ demonstrate a power-law behavior that is typical for intermittency , cf. Fig. 3.23.

$$\langle \tau_{\mathrm{ML}} \rangle \propto |K - K_b|^{-\alpha}, \tag{3.35}$$

where the critical exponent is estimated to be $\alpha \approx 0.27$, which is related to properties of the underlying unstable periodic orbit, see [66].

Parameter survey for mode-locked solutions

For a system of $N = 21$ oscillators, simulations are performed for different parameter pairs (K, γ) starting from prepared initial conditions akin to Fig. 3.6. After passage of an initial transient, $\max_t R_1(t)$ and $\langle R_1(t) \rangle_t$ are recorded and used to identify regions with pulsed solutions, as was already done in Fig. 3.8. The resulting landscape of the values is presented in Fig. 3.24. Mode-locked solutions are found where the coloring is dark blue in the left and yellow in the right panel. The landscape presented helps to identify regions of mode

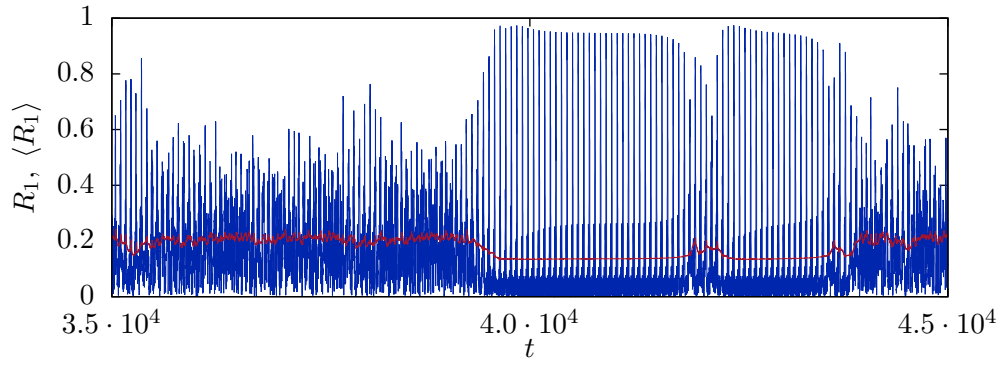

Figure 3.22: Time trace of $R_1(t)$ (blue) that appears like a bursting of the mean field and the rolling average (3.34) (red) at $(K, \gamma) = (1.12, 0.82)$ shows alternation between phase turbulence and an unstable mode-locked solution.

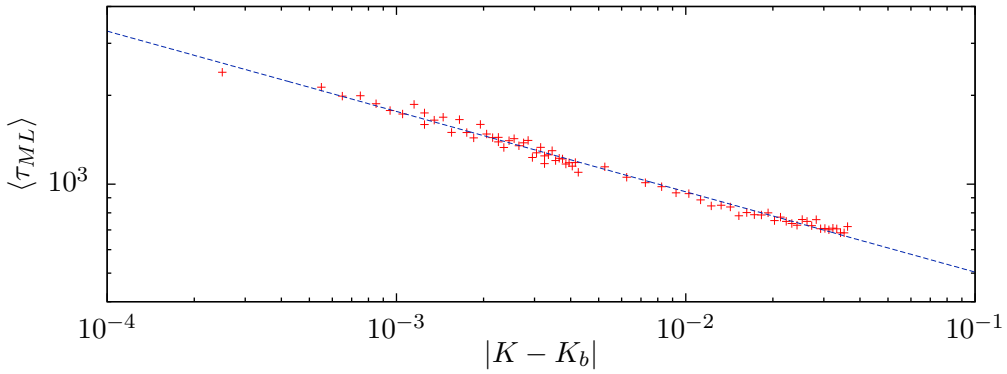

Figure 3.23: The average duration of the intermittent mode locking $\langle \tau_{\mathrm{ML}} \rangle$ with respect to the distance to the bifurcation $|K - K_b|$ in a double logarithmic plot demonstrates the power-law scaling of intermittency.

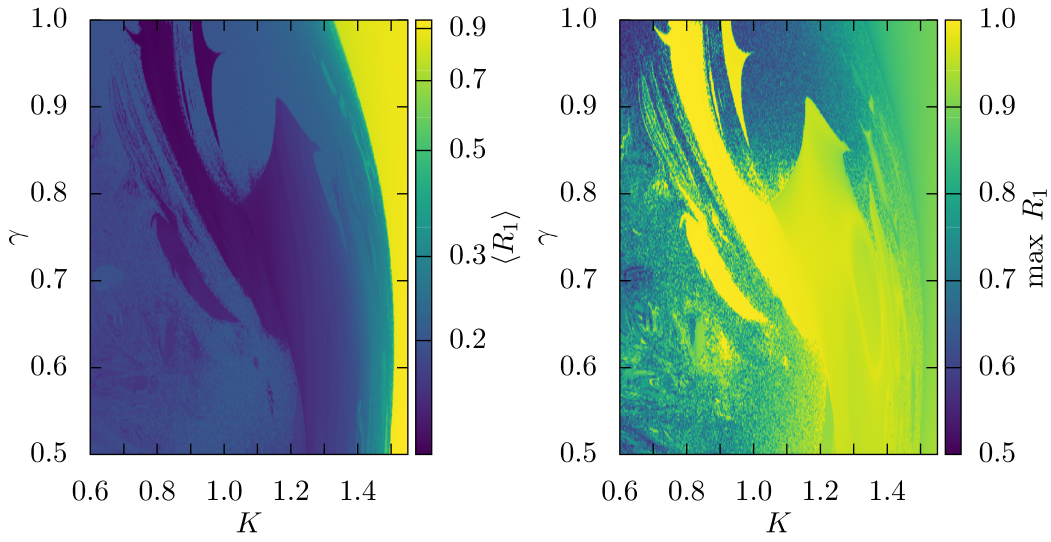

Figure 3.24: Starting from prepared synchronous initial conditions, $\max_t R_1(t)$ and $\langle R_1(t)\rangle_t$ reveal the abundance of mode-locked solutions for different parameter values.

locking and discern them from regions of phase turbulence or synchronous solutions. The survey does not allow to make a distinction between the different types of mode-locked solutions. However, their abundance is clearly demonstrated.

To identify regions of periodic solution, one can calculate the largest Lyapunov exponent λ_1, cf. Fig. 3.25. One notes that the positive maximal Lyapunov exponent is very small at lower coupling values K, while it is an order of magnitude bigger for the large coupling values (yellow regions). The chosen system dimension is still relatively small, which means that finite-size effects are still part of the picture. Creating a survey for a larger system, e.g. $N = \mathcal{O}(10^2)$, is not being done because of the long computational times.

3.5.3 Classification of Chaotic Transients

By choosing the combs of natural frequencies to be normalized to the interval $[-1, 1]$ for any system size $N = 2n + 1$, the critical coupling of the synchronization transition K_C is fixed up to finite-size effects. In this setup, the number of oscillators directly scales the spacing of the natural frequencies by $\Delta\omega = 1/n$ which then gives a rough approximation of the expected period

$$T(N) \approx \pi(N - 1). \tag{3.36}$$

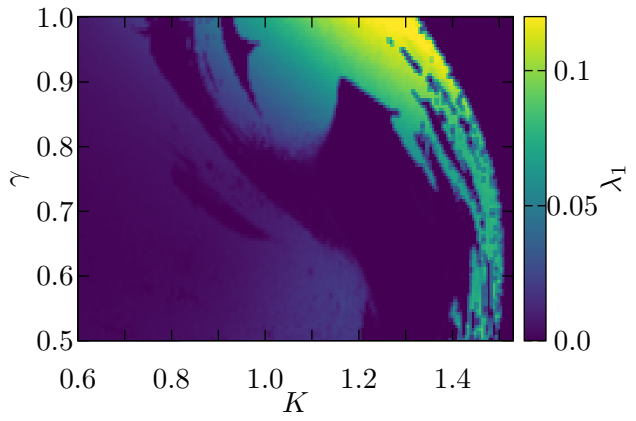

Figure 3.25: Starting from the same initial conditions as in Fig. 3.24, with $N = 21$, the largest Lyapunov exponent λ_1 is calculated for different parameter values over an interval of $2.5 \cdot 10^4$ time units.

This approximation refers to the exact period of the prototypical solution $T = 2\pi/\Delta\omega$. The period of the mode-locked solution with $K > 0$ is in general slightly longer. Although the existence of mode-locked solutions does not depend on the system size, the average length of the chaotic transients in the system depends heavily on N. With increasing system size, an exponential increase in the average chaotic transient time is observed, cf. Fig. 3.26. The data is collected by averaging over many transients for different random initial conditions. The exponential growth cannot be explained by the linear relationship (3.36). The growth of the average transient time is instead related to the exponential increase in phase space volume when additional oscillators are added. The averaged transient times follow the exponential relation

$$\langle \tau_{\mathrm{tr}} \rangle = A e^{\kappa N}. \tag{3.37}$$

In the example presented for fixed system parameters $(K, \gamma) = (1.2, 0.7)$, one finds the exponent $\kappa \approx 0.107$ and $A \approx 158$. The transients are classified as type-II chaotic supertransients [5, 67, 53, 68], i.e. the transition from the turbulent phase to mode locking is abrupt. The types of transients can be distinguished from the evolution of the finite-time Lyapunov exponent (2.45) along the transient trajectory. The finite-time Lyapunov exponent $\lambda_{\mathrm{ft}}(t)$ together with the time trace $R_1(t)$ for a system of 21 oscillators with $(K, \gamma) = (1.2, 0.85)$ are presented in Fig. 3.27. The type-II transients characteristically maintain a certain magnitude of the finite-time Lyapunov exponent before one observes a quick decent to zero within the length of the chosen time window. Similarly, Chimeras states in spatially extended finite

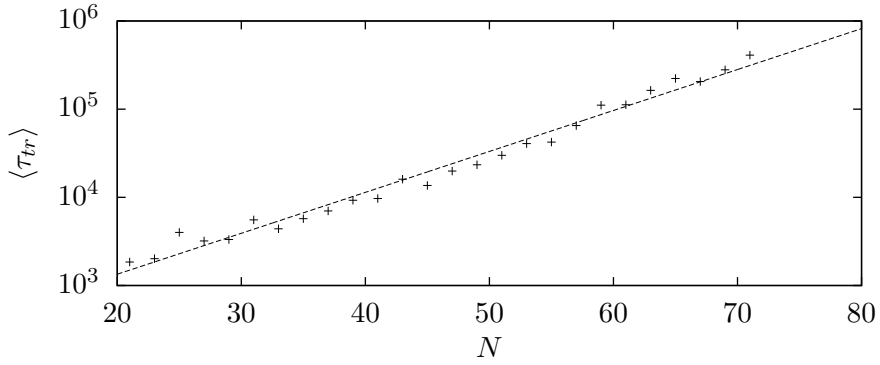

Figure 3.26: Averaged lengths of the chaotic transients are shown on the ordinate logarithmic axis against varying system sizes for fixed parameter $(K, \gamma) = (1.2, 0.7)$. For each data point, at least 300 different initial conditions are used to obtain the average.

size systems were found to be type-II chaotic supertransients [69], where after exponentially long chaotic transients, the collapse of the incoherent phase occurs. Type-I transients in comparison would show a gradual decline of $\lambda_{\mathrm{ft}}(t)$ starting from the beginning of the trajectory. Such a progressive decent process is in general recognized as an aging of the system state.

To illustrate that mode-locked solutions indeed still exist for large N, two examples obtained from prepared initial conditions for $N = 201$ and $(K, \gamma) = (0.91, 1.0)$ and $(1.2, 0.7)$ are given in Fig. 3.28. Because of the rapid growth of the average transient times with N, normal computation times can easily be exceeded by orders of magnitude before convergence to mode locking takes place. In this way, the true asymptotic state of the system can be hidden behind the exponentially long-living chaotic transients, and therefore it is likely that such state can be overlooked in simulations. Extrapolating the average transient time in Fig. 3.26 for the given example with system parameters $(K, \gamma) = (1.2, 0.7)$ leads, for instance, to an expected transient time of order $t_{\mathrm{tr}} \approx 10^{11}$. Regarding the case with $\gamma = 1$, phase turbulence was not observed to be transient even for small N.

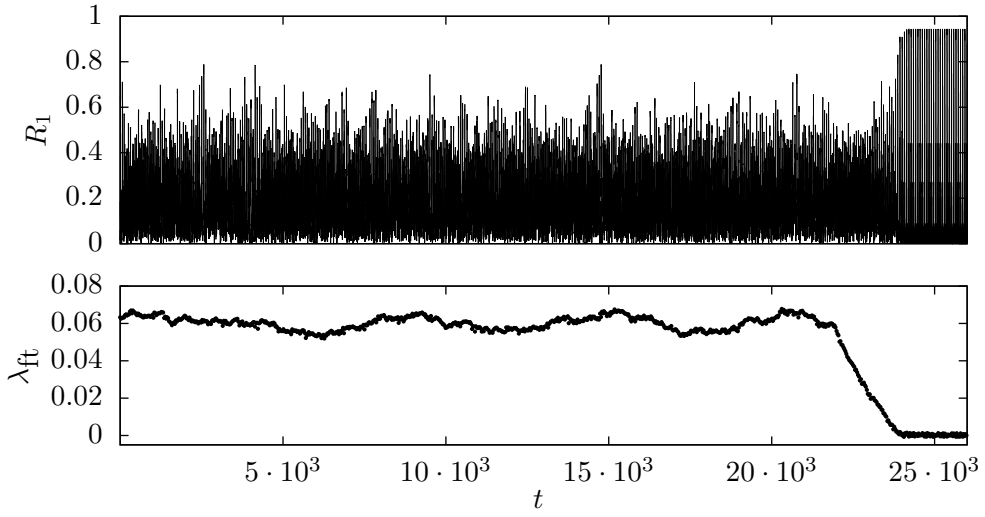

Figure 3.27: Convergence to a mode-locked solution and evolution of the finite-time Lyapunov exponent for $N = 21$ and $(K, \gamma) = (1.2, 0.85)$ where the time window for computation of the finite-time exponents $\lambda_{\rm ft}(t)$ has a length of 2000 time units.

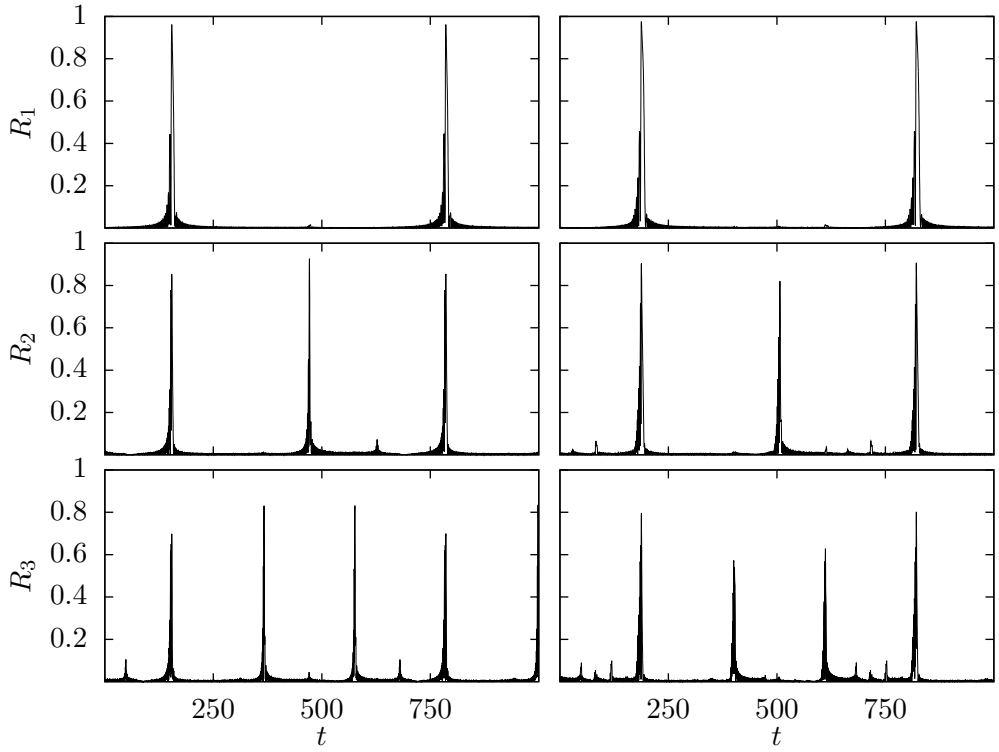

Figure 3.28: The time traces $R_1(t)$, $R_2(t)$ and $R_3(t)$ for the mode-locked solutions with $N = 201$ oscillators, $(K, \gamma) = (0.91, 1.0)$ (left) and $(K, \gamma) = (1.2, 0.7)$ (right). $R_3(t)$ is the modulus of the third complex order parameter with $q = 3$ in (2.22).

3.6 Detuned Combs of Natural Frequencies

Exactly equidistant frequency combs correspond to an idealized situation that in general can be perturbed in a random or systematic fashion. One finds that the phenomenon of mode-locking is robust with respect to both types of perturbations. The transitions from stable mode-locking to phase turbulence with quenched disorder are also of the intermittency type described.

3.6.1 Frequency Combs with Quenched Disorder

For the prototype solutions, it was presented that small quenched disorder leads to the degradation of the pulsed solution, see Fig. 3.4. The effect of the quenched disorder can be compensated by the global interaction which is therefore able to stabilize the mode-locked solutions. In this case, during the appearance of a pulse, the contraction is strong enough to adjust for the individual detuning.

The natural frequencies including a quenched disorder term are given by

$$\omega_j = \Delta\omega(j + Q\zeta_j), \quad j \in \{-n, \ldots, n\}, \tag{3.38}$$

where $\Delta\omega = 1/n$ is the equidistant spacing, Q is the amplitude of the frequency perturbations, and ζ_j are random independent perturbations, for instance, drawn from a Gaussian or a uniform distribution. A relabelling of the oscillators is always possible such that $\omega_{-n} \leqslant \omega_{-n+1} \leqslant \cdots \leqslant \omega_n$, although the cases that are considered here have perturbations that are much smaller than the equidistant spacing $\Delta\omega$. The average frequency spacing of the perturbed comb is given by $\langle \Delta\omega_j \rangle = |\omega_n - \omega_{-n}|/2n$, which should also be close to the spacing $\Delta\omega$.

It turns out that the transient time behavior is mostly unaffected by the quenched disorder, as it is governed by the system size scaling (3.37). For sufficiently small Q, the system exhibits mode locking since for $Q = 0$, the original unperturbed frequency comb is retrieved. The breakdown of the mode-locked solution can be observed by successively increasing Q, which for a particular realization of the quenched disorder is shown in Fig. 3.29. Note that the mode-locked and turbulent regimes are separated by a thin layer exhibiting intermittency.

The resilience of mode-locked solutions to quenched noise in the frequencies can be quantified with respect to Q in the form of a probability to obtain a realization that converges to a mode-locked solution $P(Q) = u_{\text{conv}}/u$ where u_{conv} denotes the number of realizations that converge to a mode-locked solution and p denotes the total number of realization considered. To sample over many realizations and Q efficiently, the system size should be small,

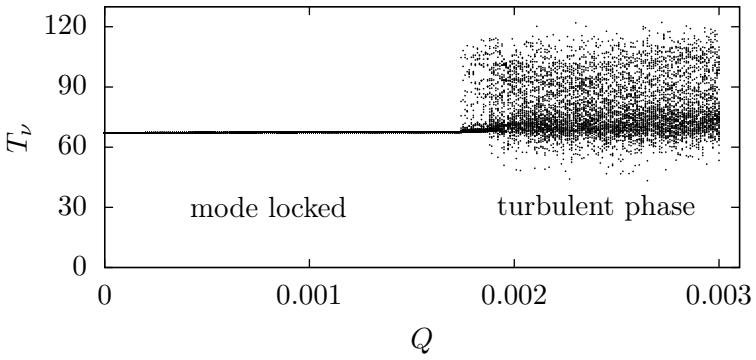

Figure 3.29: Return times T_ν to the Poincaré section (3.31) demonstrate the transition from a mode-locked solution to phase turbulence with increasing Q. The system is specified by $(N, K, \gamma) = (21, 1.2, 0.7)$.

however, it is clear that for small N, the relevance of finite-size effects increases. Fixing the system size and parameters to $(N, K, \gamma) = (21, 1.2, 0.7)$ for $Q = 0$, one recovers a stable mode-locked solution of the type Def. 1. The different realizations of the frequency perturbations are drawn from a standard normal distribution $\mathcal{N}(0, 1)$. As the initial condition, the mode-locked solution for $Q = 0$ is used, which in most cases is an adequate guess that can be precomputed. To achieve a good sampling, the total number of realizations of the quenched disorder is $u = 10^4$. The procedure reveals a smooth phase transition from systems that exhibit mode locking to systems that are with high probability unable to maintain the pulsed solutions, see Fig. 3.30. For the presented study, only solutions with $p = 1$ in Def. 1 were regarded, which excludes all modulated and especially also subharmonic mode-locked solutions Def. 3. Including solutions with a larger number of peaks could affect the steepness of the phase transition.

To obtain a measure of the strength of the perturbation, one can calculate the nearest equidistant frequency comb to any perturbed comb like (3.38). The set of all equidistant frequency combs can be defined as

$$\mathcal{M} := \{x \in \mathbb{R}^{2n+1} : x_j = \nu + j\Delta\nu\} \quad \text{with } j \in \{-n, \ldots, n\}, \tag{3.39}$$

where any frequency comb is defined by the number of different frequencies $N = 2n + 1$, the comb offset $\nu \in \mathbb{R}$ and the spacing $\Delta\nu \in \mathbb{R}^+/\{0\}$. Given a perturbed comb (3.38), one can define the distance to an element $x \in \mathcal{M}$ as

$$d(\omega, x) := \|\omega - x\|_{L^2}, \tag{3.40}$$

where $\omega \in \mathbb{R}^{2n+1}$ is the perturbed comb. An equidistant frequency comb that

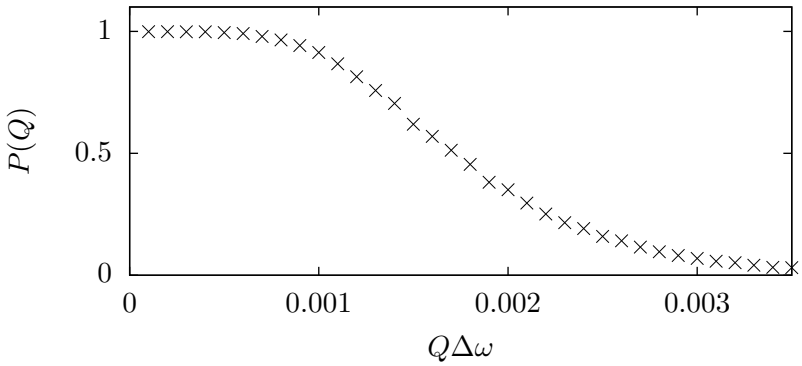

Figure 3.30: The probability of a system with a perturbed frequency comb to converge to mode locking for different perturbation strength Q. The system is specified by $(N, K, \gamma) = (21, 1.2, 0.7)$.

minimizes this distance $x_{\min} \in \mathcal{M}$ can be found

$$x_{\min} := \min_{x \in \mathcal{M}} d(\omega, x). \tag{3.41}$$

From the partial derivatives of (3.40) with respect to ν and $\Delta\nu$, one obtains the following two conditions for the minimum

$$\sum_{j=-n}^{n} (j\Delta\omega + \zeta_j - \nu - j\Delta\nu) = 0, \tag{3.42}$$

$$\sum_{j=-n}^{n} j(j\Delta\omega + \zeta_j - \nu - j\Delta\nu) = 0. \tag{3.43}$$

The first condition (3.42) can be used to compute ν where one uses that $j\Delta\omega$ and $j\Delta\nu$ vanish symmetrically in the sum, hence

$$\frac{1}{N} \sum_{j=-n}^{n} \zeta_j = \nu, \tag{3.44}$$

the comb offset is therefore given by the average of the realization. Afterwards, ν can be used to solve for $\Delta\nu$ in the second condition (3.43)

$$\sum_{j=-n}^{n} j^2 \Delta\nu = \sum_{j=-n}^{n} j(j\Delta\omega + \zeta_j - \langle\zeta_j\rangle). \tag{3.45}$$

The sums that include the spacings are

$$\sum_{j=-n}^{n} j^2 \Delta\nu = \Delta\nu \frac{n(n+1)(2n+1)}{3}, \tag{3.46}$$

$$\sum_{j=-n}^{n} j^2 \Delta\omega = \Delta\omega \frac{n(n+1)(2n+1)}{3}. \tag{3.47}$$

Eventually, one finds the spacing of the closest equidistant comb

$$\Delta\nu = \Delta\omega + \frac{3}{n(n+1)(2n+1)} \sum_{j=-n}^{n} j(\zeta_j - \langle\zeta_j\rangle). \tag{3.48}$$

Proceeding in a similar fashion, one can now compute the probability that the system with a perturbed frequency comb ω and $d_{\min} = d(\omega, x_{\min})$ is converging to a mode-locked solution. Here again, only solutions of the type Def. 1 with $p = 1$ are regarded. The number of realizations that support mode locking u_{conv} within a small range of the distances relative to the total number of sampled realizations in that particular range u_d give the probability $P(d_{\min}) = u_{\text{conv}}/u_d$, which is presented in Fig. 3.31. For large distances between the perturbed comb and the set of equidistant combs, the system loses the ability of mode locking.

In contrast to the transition that follows by increasing Q, the criterion including the minimal distance to the set of equidistant frequency combs can be used to access the mode locking quality of individual frequency combs in a statistical fashion regarding the distance. A similar access to the ability of mode locking for an individual frequency comb is attained by looking at the kurtosis of the individual realizations. The influence of quenched disorder on the stability of mode-locked solutions has been demonstrated as a smooth phase transition in terms of Q and $d_{\min} = d(\omega, x_{\min})$. The complex underlying problem is the interrelation between perturbations of the frequencies which is in general difficult to access. As a vivid illustration of the complexity of this task, an example is presented where disjointed regions of stable mode locking appear for one particular realization of the quenched disorder, cf. Fig. 3.32.

3.6.2 Frequencies with Systematic Detuning

Systematic detuning takes an equidistant frequency comb and applies a spreading or a compression to the natural frequencies depending on the oscillator index. Here, a cubic dependence on the index is considered, which preserves the symmetry with respect to the central frequency

$$\omega_k = \Delta\omega(k + Dk^3), \quad k \in \{-n, \ldots, n\}, \tag{3.49}$$

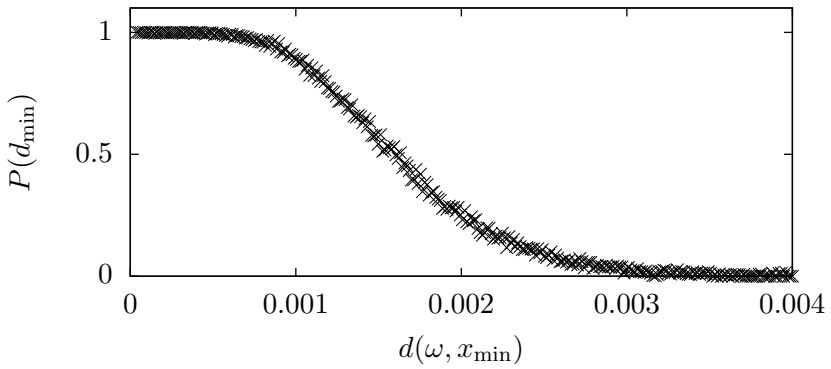

Figure 3.31: Probability of a system with a perturbed frequency comb to converge to a mode-locked solution depending on the distance to the nearest equidistant frequency comb $d_{\min}$, for the system configuration $(N, K, \gamma) = (21, 1.2, 0.7)$.

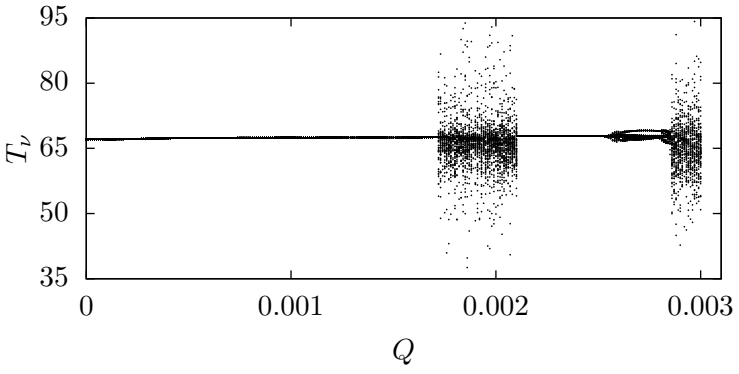

Figure 3.32: A particular realization can allow multiple disjointed islands of mode-locked solutions to exist. The system parameters are $(N, K, \gamma) = (21, 1.2, 0.7)$.

where $\Delta\omega = 1/n$ is the equidistant linear spacing and D is the amplitude of the detuning.

For zero detuning $D = 0$, the equidistant frequencies are retrieved such that for appropriate system parameters, mode locking is recovered. The two choices $D < 0$ and $D > 0$ correspond to compression or attenuation of the frequencies compared with the unperturbed comb. Very small values of D can compromise index ordering of the frequencies in the comb (3.49), which is avoided for D that fulfills $D > \frac{1}{k^3-(k+1)^3}$ ensuring $\omega_k < \omega_{k+1}$ for all $k \in \{-n, \ldots, n-1\}$. In the regions, where this condition is violated, mode merging occurs frequently and the detuning dominates the linear frequency spacing which will not be considered further.

For detuning amplitudes $D \approx 0$, one finds a region of equidistant mode-locked solutions, cf. Fig. 3.33. A simple definition of the pulse width t_p is the elapsed time between certain points on the slope of the pulse of, for instance, specified magnitude $\frac{3}{4}\max_t R_1(t)$. The cubic static detuning turns out to have a marginal effect on the pulse width t_p. The pulse width is primarily influenced by the number of oscillators. Because the number of oscillators is constant, the pulse width does not vary significantly.

For negative detuning amplitudes $D < 0$, corresponding to a comb compression, the pulse width increases. This is attributed to the fact that for compressed frequency combs, the oscillators are closer to synchronization where pulses tend to be elongated. In the opposite way, one can observe that for attenuation of the frequencies, the pulses become shorter as the oscillators are further away from being synchronized.

For further increasing D in either direction, the mode-locked solutions are found to destabilize in two different breakdown scenarios, see Fig. 3.34. In the figure, the averaged order parameter $\langle R_1(t)\rangle_t$ is presented to identify mode locking regions, and the effective frequency combs are shown to distinguish the two different pathways to phase turbulence.

For $D < 0$ in a gradual process, the outermost oscillators start to unlock from the pulsed solution. However, for various detuning values, the unlocked oscillators are close enough to achieve subharmonic mode locking with the rest of the population such that periodicity is reestablished and solutions is of the type Def. 3.

In contrast to that for $D > 0$, the mode-locked solution loses its stability abruptly, after which the frequency spacings follow a parabola as expected for the cubic detuning. A solution survey for a system of $N = 21$ at pairs of (K, γ) and fixed $D = -0.000065$ is shown in Fig. 3.35. The parameter regions, where mode-locked solutions are found agree to a large extent with the landscape for the equidistant frequency comb Fig. 3.24.

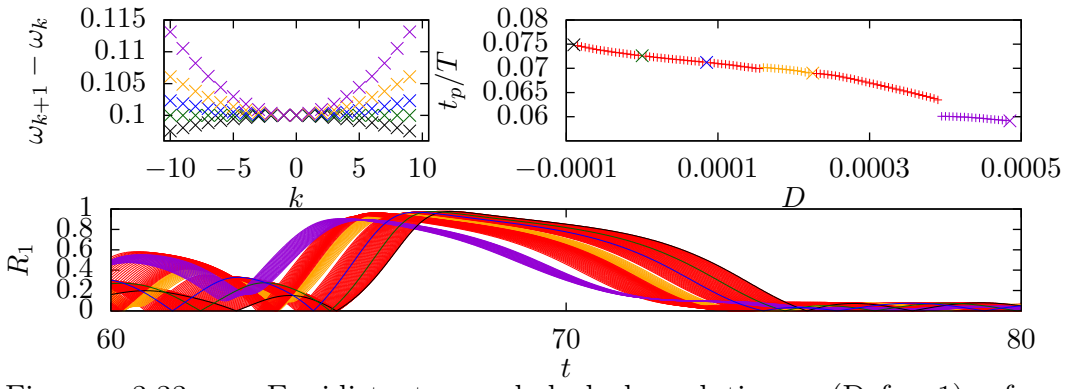

Figure 3.33: Equidistant mode-locked solutions (Def. 1) for $(N, K, \gamma) = (21, 1.2, 0.7)$. The combs of natural frequencies are presented on the top left, where color and symbol relate to the top right panel which shows the normalized pulse width t_p/T. Time traces $R_1(t)$ (bottom panel): different colors relate to the top right panel. For the purple and the yellow solutions, the central mode symmetry is broken, $\chi > 0$ in (3.11).

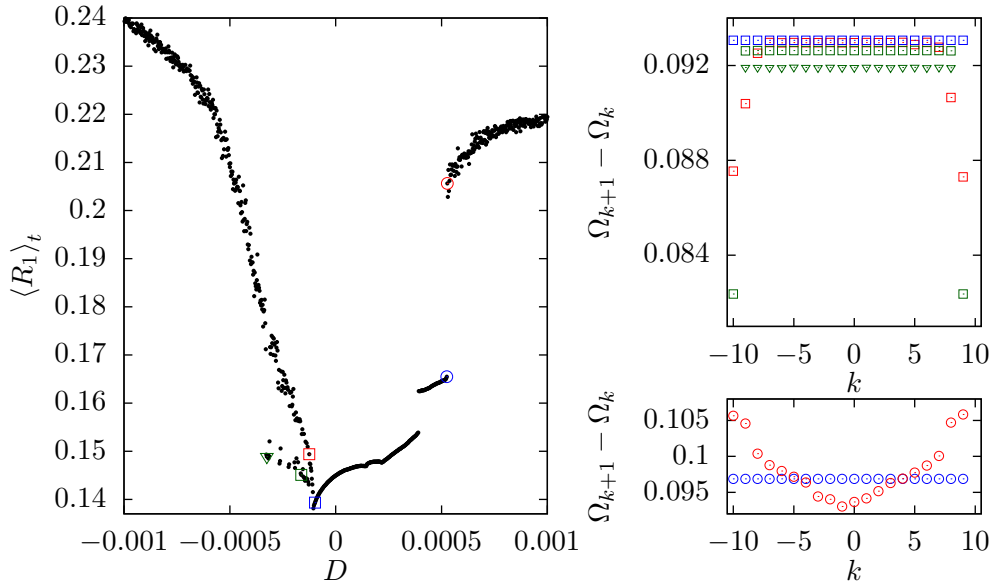

Figure 3.34: Breakdown of mode locking for varying D with system parameters being $(N, K, \gamma) = (21, 1.2, 0.7)$. Left panel: $\langle R_1 \rangle_t$ indicates regions of mode locking. Right panels: effective frequency spacings in corresponding symbols to the left. Blue symbols correspond to equidistant solutions Def.1, green symbols to subharmonic solutions Def.3, and red symbols indicate non-periodic solutions. The outermost green triangle spacings are omitted due to their scaling.

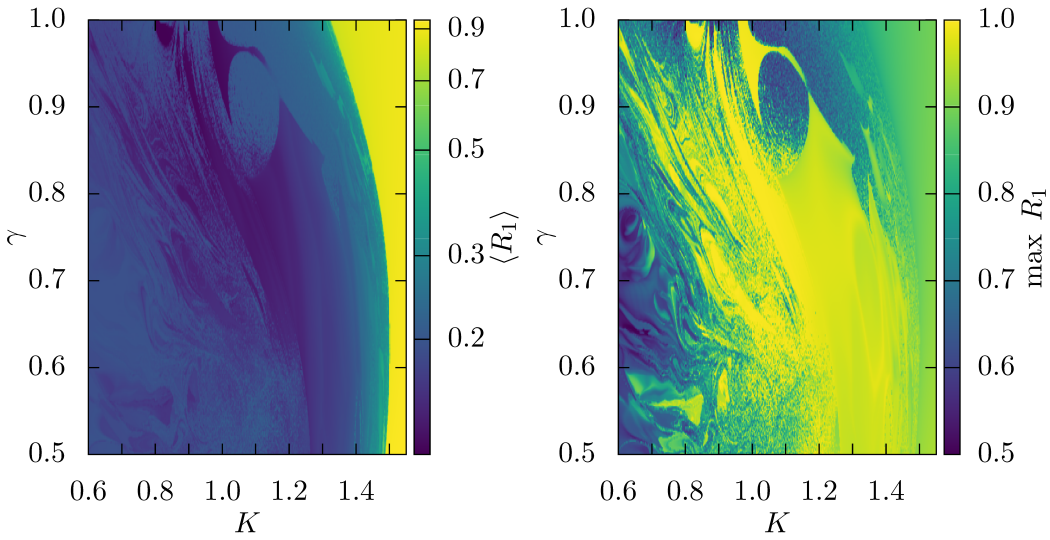

Figure 3.35: For a system with $N = 21$ and systematic detuning amplitude $D = -0.000065$ in (3.49), a simulation is performed for pairs of (K, γ). The initial state is generated by letting $K > K_C$. After an initial transient, $\max_t R_1(t)$ and $\langle R_1(t) \rangle_t$ are recorded.

3.7 Mode Locking in Large Ensembles

Up to this point, the considered models include a rather small number of oscillators, where every oscillator has its own very distinct natural frequency. From the applications point of view, it is of great importance to also consider models consisting of large numbers of oscillators where the natural frequencies come from some frequency distribution.

In this section, frequency distributions are considered that have a multimodal appearance. Mode-locked solutions, similar to Def. 1, are found that show the typical behavior of pulses in the coherence radius $R_1(t)$. The emergence of mode-locked solutions in large ensembles of globally-coupled phase oscillators is discussed, where the main aspect of difference is that of *modal synchronization*, which is a necessary ingredient in the process of mode locking in large systems.

3.7.1 Multimodal Frequency Distributions and Modal Order Parameters

The natural frequencies of the model are given by

$$\omega_{k,j} = \Delta\omega(k + Q\zeta_{k,j}), \quad k \in \{-n, \ldots, n\},\ j \in \{1, \ldots, M\}, \tag{3.50}$$

where k is called the *mode index*, j is the oscillator index within each mode, Q is the amplitude of the random detuning, and $\zeta_{k,j}$ are independent random numbers drawn from a standard normal distribution. A mode is defined accordingly as the set of all oscillators with modal index k.

The total number of oscillators is $N = (2n+1)M$, where each mode consists of M oscillators with frequencies distributed around the equidistant frequencies $\omega_k = \Delta\omega k$. In this way, the average natural frequencies of the modes are almost equidistant. The variance from the equidistant average mode frequencies is Q^2. For the natural frequencies to maintain a comb structure, one has to require $Q^2 \ll \Delta\omega$ such that the modes are well separated. It is expected that at a certain level of Q, mode locking will no longer be possible due to the loss of the modal structure.

The system equations of the large ensembles read

$$\dot{\theta}_{k,j} = \omega_{k,j} + \frac{K}{N}\sum_{p=-n}^{n}\sum_{q=1}^{M}\left[\gamma\sin(\theta_{p,q}-\theta_{k,j}) + (1-\gamma)\sin(2(\theta_{p,q}-\theta_{k,j}))\right]. \tag{3.51}$$

In order for the predefined modes to make sense, the separation condition $Q^2 \ll \Delta\omega$ should hold. The modal synchronization level can be attained by the *modal order parameters*

$$\eta_{q,k} = R_{q,k}e^{\mathrm{i}\Psi_{q,k}} := \frac{1}{M}\sum_{j=1}^{M} e^{\mathrm{i}q\theta_{k,j}}, \quad q \in \{1,2\}, \tag{3.52}$$

where mode k is synchronous, when $R_{1,k}(t) \approx 1$. At large values of Q, the modal structure as a general prerequisite for mode locking is certainly destroyed and mode locking is no longer possible. For self-organized mode locking, the second harmonic as previously discussed is significant, and suitable parameter values such as $(K,\gamma) = (1.2, 0.7)$ should be considered.

Concerning the study of continuum limit descriptions by means of the Ott-Antonson ansatz [70], note that due to the second harmonic in the interaction function, the ansatz cannot be applied here. Although one can in principle drop the second harmonic for the sake of this particular obstacle with the self-organization of mode locking crucially depending on the second harmonic, the most interesting feature of the system would be lost. It has been shown that the Ott-Antonsen ansatz is applicable to multimodal frequency distributions [71, 72] where it is claimed that complicated chaotic dynamics can be expected.

Aside from the potential to observe chaotic dynamics, it is expected that stable mode-locked states can be found following the recipe for setting up suitable initial conditions for mode locking.

3.7.2 Self-Organization to Mode-Locked Solutions

From the discussion of the basic system (3.1), one expects the length of the preceding transients of mode locking to scale exponentially with the number of modes $2n + 1$. The properly balanced second harmonic of the interaction that made the mode-locked solutions emerge from random initial configurations is again crucial so that the parameters of the interaction are fixed to $(K, \gamma) = (1.2, 0.7)$.

For large ensembles, mode locking essentially becomes a two-stage process where modal synchronization precedes the locking of the modes. When the modal synchronization is low, the phenomenon of mode locking in general appears less pronounced or even breaks down completely. It is found that in principle, partially synchronized modes also adhere to mode locking. In Fig. 3.36, the emergence of a mode-locked solution is presented for a system consisting of 15 modes, where each mode consists of 5000 oscillators such that the average natural frequency of the modes are very close to the equidistant $\omega_k = \Delta\omega k$. The detuning amplitude is set to $Q = 0.01$, resulting in well-separated modes, cf. histogram of the natural frequencies Fig. 3.36, with $Q^2 \ll \Delta\omega = 1/7$.

To demonstrate the two processes of modal synchronization and mode locking, both the modal (3.52) and the complete order parameters are recorded. The modal synchronization increases most significantly at the times when $R_1(t)$ is large. There is a tendency that the modes on the edge of the comb synchronize last.

A close-up of the final mode-locked solution shown in Fig. 3.37 reveals a breathing behavior, where preceding to the mode-locking pulses some of the modal order parameters decrease before, on the falling edge of the pulse, all modal synchronization level $R_{1,k}(t)$ increase again. Between the pulses, the modal synchronization slowly decreases until a stabilizing effect governed by the second harmonic appears halfway between the pulses in $R_1(t)$. This conforms with the stabilizing influence on mode locking by the second harmonic that has previously been demonstrated, cf. Fig. 3.15. In large ensembles, the second harmonic has the additional effect of contributing to the modal synchronization level at the half of the inter-pulse interval. Note that the mode-locked solution shows a particularly strong breathing of the modes with indices $k = -3$ and $k = 0$. It is curious that the breathing strength is not ordered by the mode index. This is related to the fact that on the rising edge of the pulse, the modal phases $\Psi_{q,k}$ are not ordered by the indices.

The tendency that the modal synchronization appears first for the more central modes is illustrated for a transient in a system with 31 modes, cf. Fig. 3.38. Here, one also sees that the transient time is longer, which on av-

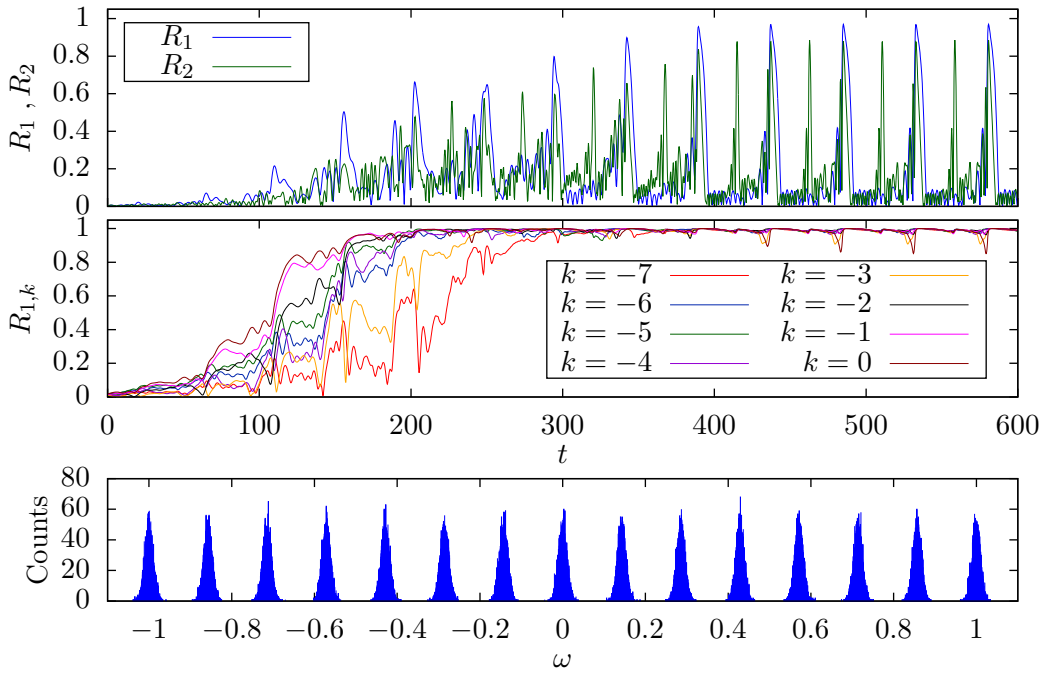

Figure 3.36: The system (3.51) with system parameters $(K, \gamma, Q) = (1.2, 0.7, 0.01)$, and $2n + 1 = 15$ modes consisting of $M = 5000$ oscillators is initialized with random uniform phases. The time traces $R_1(t), R_2(t)$, and the modal order parameter $R_{1,k}(t)$ (3.52) are presented for the modes $k \in \{-7, \ldots, 0\}$. The histogram of the natural frequencies illustrates that the modes are well separated.

erage scales exponentially with the number of modes $(2n + 1)$. The additional contribution to the transient times that come from the modal synchronization prior to the locking is expected to scale subexponentially.

3.7.3 Stability with Respect to the Spectral Width

The detuning amplitude Q characterizes what will be called the *spectral width* of the modes. It tells what range of natural frequencies are attributed to a specific mode and whether the modes are clearly distinguishable from each other. To approach the value of Q for which the mode-locked solutions destabilize initial conditions close to the mode-locked state are used, the initial conditions are obtained by first increasing the coupling strength above critical $(K = 1.5 > K_C)$. Instead of making a parameter scan in Q, multiple simulations are performed for different values starting from the prepared initial state.

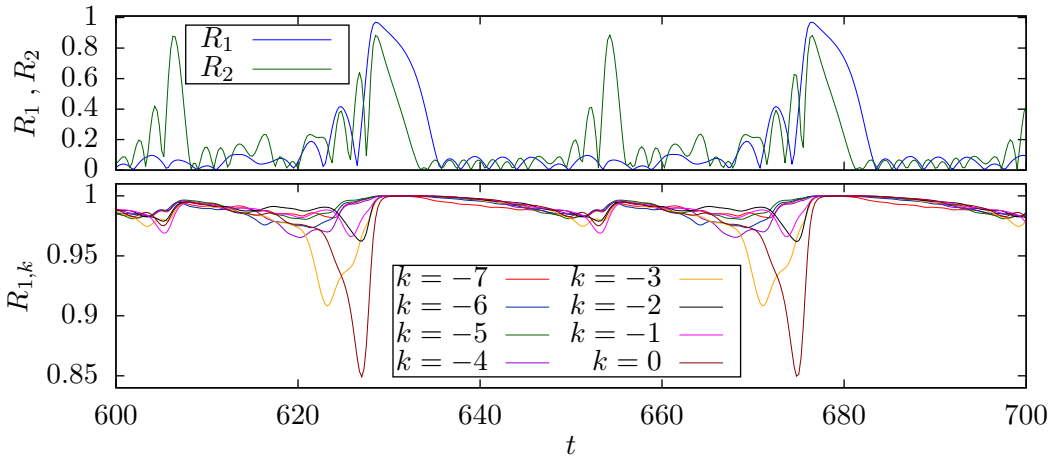

Figure 3.37: A close-up of the breathing behavior of the modal order parameter $R_{1,k}(t)$ (3.52) of the mode-locked solution, in Fig. 3.36. Some modes show a strong decline in modal synchrony preceding the pulse.

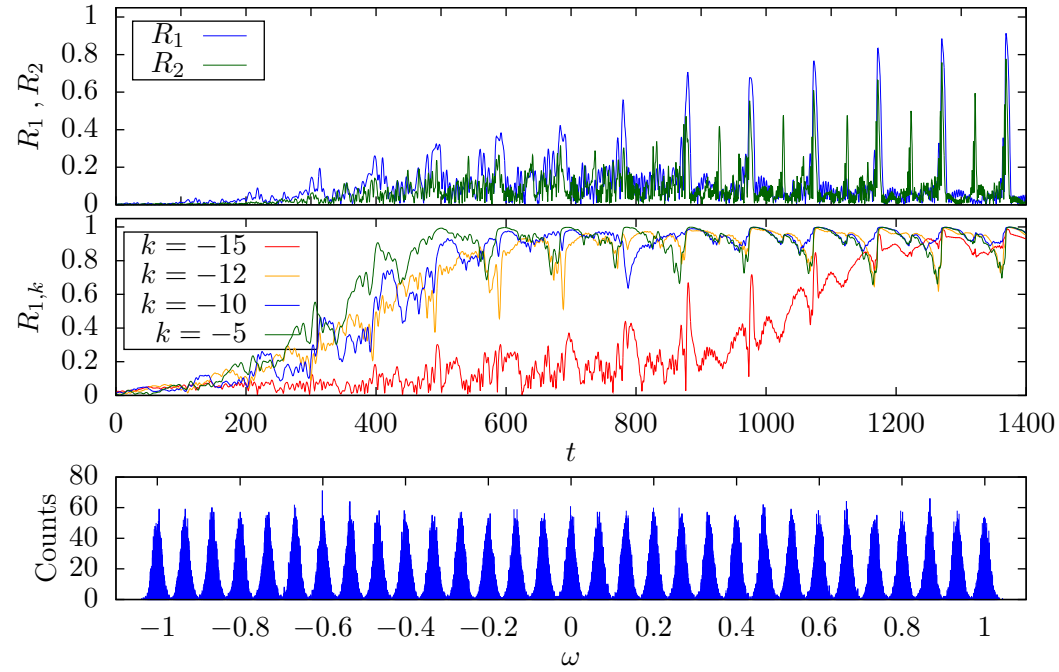

Figure 3.38: The system (3.51) with the system parameters $(K, \gamma, Q) = (1.2, 0.7, 0.01)$, and $2n+1 = 31$ modes consisting of $M = 5000$ oscillators is initialized with random uniform phases. The time traces $R_1(t), R_2(t)$, and the modal order parameters $R_{1,k}(t)$ (3.52) for $k \in \{-15, -12, -10, -5\}$ are presented. The bottom panel shows a histogram of the natural frequencies with distinct modes.

When the detuning is increased to $Q = 0.032$, one observes that the mode-locked solution becomes modulated, cf. Fig. 3.39. In the example shown, the number of oscillators is $N = 3 \cdot 10^5$. The solution shows smaller pulse peaks of approximately $R_1 \approx 0.8$ and significant fluctuations of the modal order parameters $R_{1,k}(t)$ (3.52).

In the histogram of the natural frequency, one sees a strong overlap between the different modes. To understand the origin of the modulation it is essential to look at the histogram of the effective frequencies (bottom panel). The histogram shows the primary effective frequency comb, which is given by the histogram boxes that reach the top and are further cut off.

Apart from the primary effective frequency comb, a substantial number of oscillators with non-matching frequencies is present. Furthermore, a secondary comb has emerged, which is the reason for the modulation of the solution. The secondary frequency comb has the same spacing as the primary one, while it is shifted by $\Delta\Omega/2$ with respect to it. It therefore adds to one pulse constructively by increasing $R_1(t)$ while decreasing it at the next pulse, hence causing the specific type of modulation. Both effective frequency combs can also be seen in a plot of $(\Omega_{k,j}, \omega_{k,j})$, cf. Fig. 3.41.

For a sufficiently broad spectral width ($Q = 0.04$), the mode-locked solution eventually breaks down, albeit some modes still maintain a significant modal synchronization, see Fig. 3.40. The prepared initial conditions decay over several pulses and the predefined modes mostly desynchronize.

3.7.4 Coexistence of Mode-Locked Solutions and Modal Turbulence

In systems with Kuramoto-type coupling ($\gamma = 1$) no additional increase in the modal synchronization is generated between the pulses in $R_1(t)$ due to the absence of the second harmonic. To find mode-locked solutions in the system with $(K, \gamma, Q) = (0.96, 1.0, 0.01)$, $N = 75 \cdot 10^3$, and $2n + 1 = 15$, cf. Fig. 3.42, one has to initialize the system with properly prepared initial conditions. The increase in the modal synchronization is an important part of the stabilization of the mode-locked solutions, since the modal synchronization has to be large $R_{1,k} \approx 1$ in order to have modes that can perform the locking.

The self-organized emergence of mode-locked solution from random initial conditions, as observed for the Kuramoto-Daido type coupling ($\gamma < 1$), could not be observed, which agrees with the previous findings of coexistence of mode locking and phase turbulence for $\gamma = 1$. In Fig. 3.43, one sees how modal synchronization is achieved without locking between the modes. This

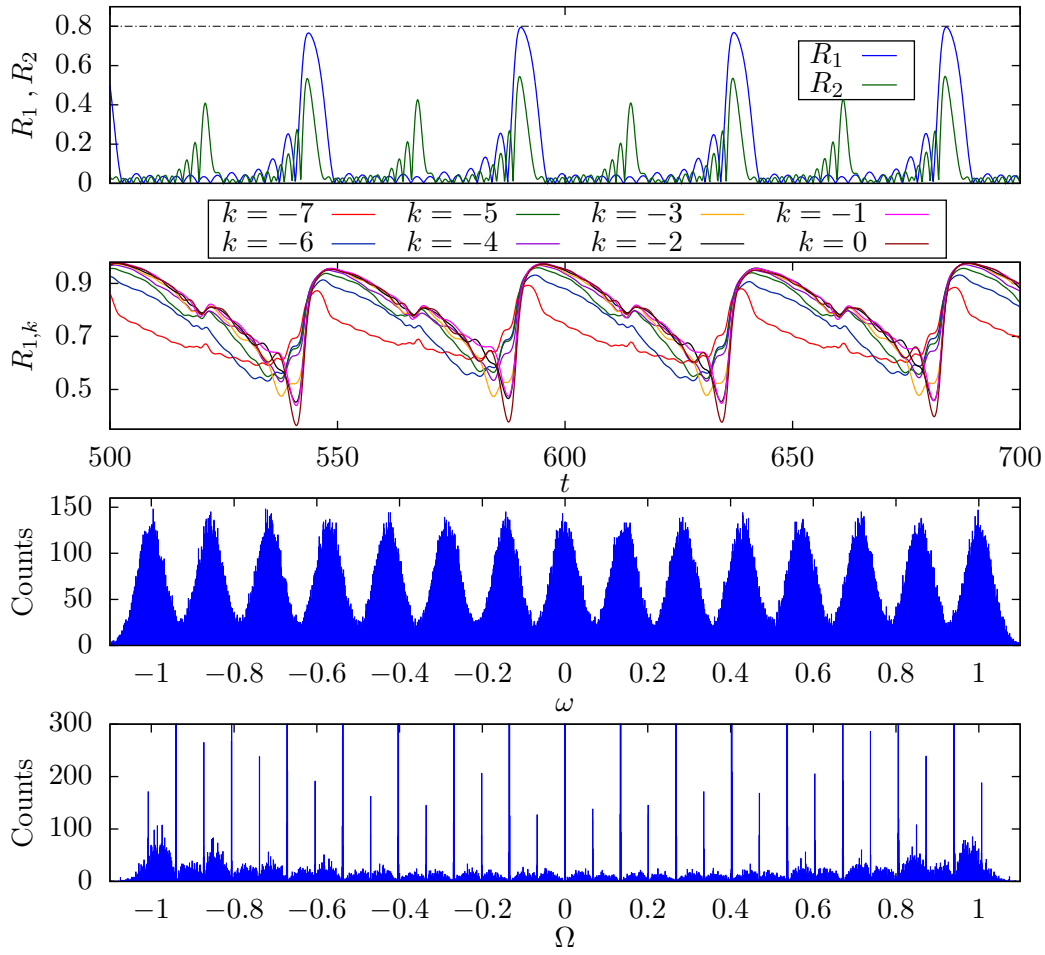

Figure 3.39: The system (3.51) consisting of $N = 3 \cdot 10^5$ oscillators, $(2n + 1 = 15)$ modes, and with the parameters $(K, \gamma, Q) = (1.2, 0.7, 0.032)$ is initialized with prepared initial conditions. The time traces $R_1(t)$, $R_2(t)$, and the modal order parameters $R_{1,k}(t)$ (3.52) for $k \in \{-7, \ldots, 0\}$ are presented. The histograms of natural frequencies and the effective frequencies are shown. Note the locking of a shifted frequency comb in the effective frequencies.

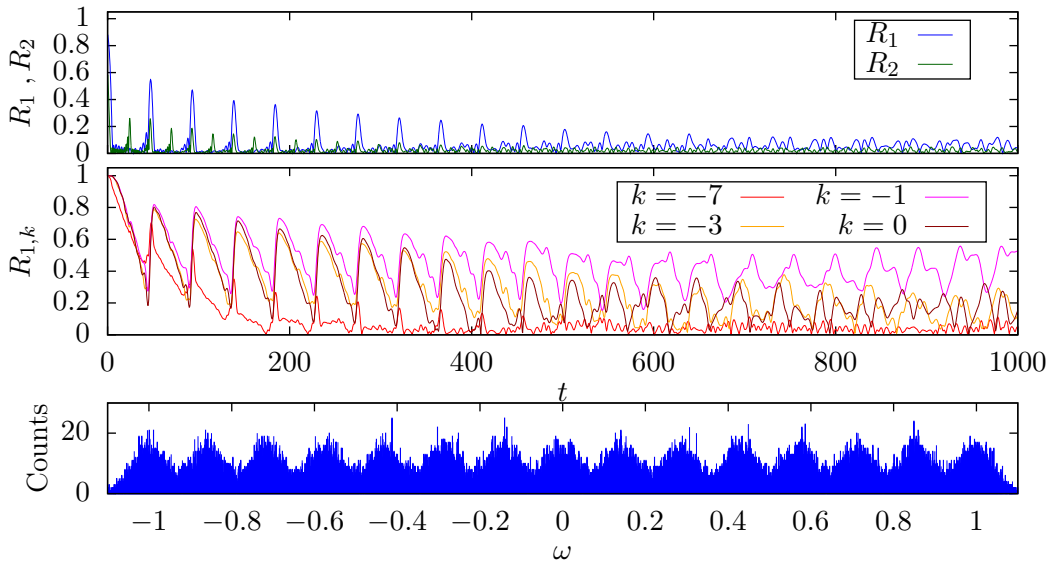

Figure 3.40: For further increased spectral width $Q = 0.04$, in the system studied shown in Fig. 3.39, the modal synchronization breaks down. The time traces $R_1(t)$, $R_2(t)$, and modal order parameters $R_{1,k}(t)$ (3.52) are presented for $k \in \{-7, -3, -1, 0\}$. The histogram of the natural frequencies shows that the modes overlap substantially.

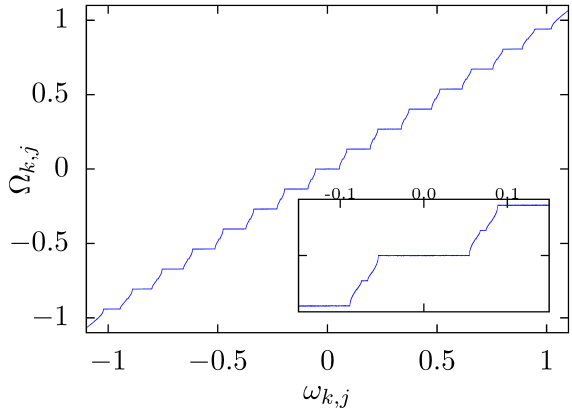

Figure 3.41: The effective frequencies $\Omega_{k,j}$ against the natural frequencies $\omega_{k,j}$ for the solution shown in Fig. 3.39.

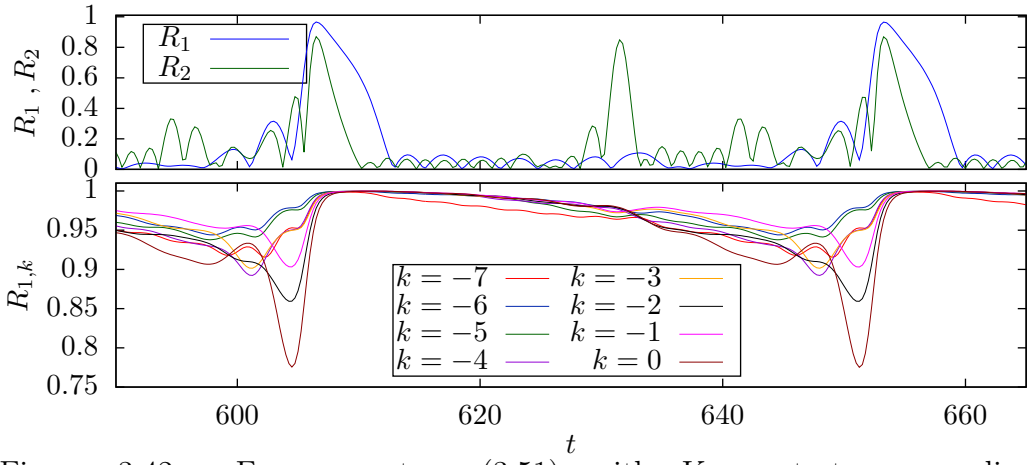

Figure 3.42: For a system (3.51) with Kuramoto-type coupling $(K, \gamma, Q) = (0.96, 1.0, 0.01)$, and $(2n + 1 = 15)$ modes consisting of $(M = 5000)$ oscillators, stable mode-locked solutions can be found from prepared initial conditions.

stresses the fact that modal synchronization is not sufficient for the emergence of mode-locked states, as the modal phases $\Psi_{1,k}(t)$ exhibit complex behavior while there is large modal synchronization overall.

3.8 Mode Locking in Optical Systems

The phenomenon of mode locking in laser systems, which has been known since the 1960s, refers to the formation of optical pulses. The diversity of mode locking laser devices is large, and even physically different mechanisms classified as active or passive are known to achieve the phenomenon [73, 74, 75, 76]. In the context of optics, light that is emitted inside the optical resonator propagates repeatedly around the cavity, where by constructive interference, a spectrum of resonant frequencies the so-called *cavity modes* emerges.

When the gain bandwidth of the laser medium is sufficiently broad, multiple cavity modes can be brought above the lasing threshold at which point the laser is in multi-modal operation. The number of amplified cavity modes can be enormous. For example, the bandwidth of a Ti:sapphire laser typically supports hundreds of thousands of modes, which in mode-locked operation results in ultra short light pulses [77, 78]. Mode locking is achieved when a sufficient number of cavity modes develop a fixed phase relationship such that they form a light pulse. In the example of the Ti:sapphire laser, mode locking is achieved by inserting a Kerr lens into the resonator that exerts a

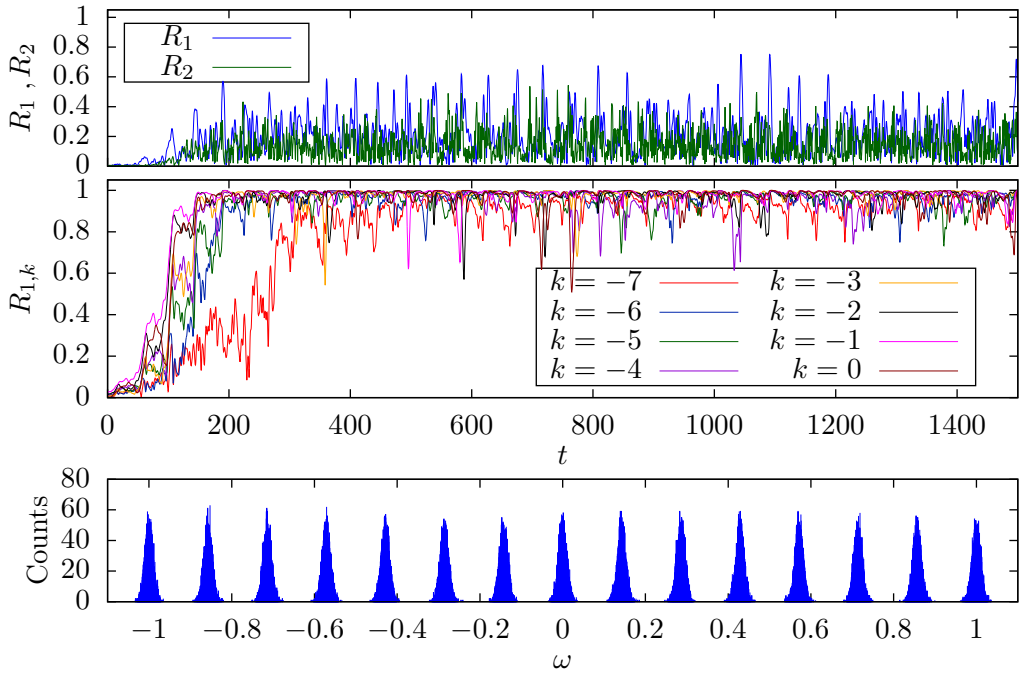

Figure 3.43: For the system used in Fig. 3.42 with the parameters $(K, \gamma, Q) = (0.96, 1.0, 0.01)$, $N = 75 \cdot 10^3$, and $2n + 1 = 15$, starting from random initial data modal synchronization is achieved ($R_{1,k}(t) \approx 1$) without locking the modes.

self-focusing effect on fields of high intensity that is in favor of the emergence of pulses.

While more traditional mode-locked lasers rely on a specific gain medium in order to produce an optical frequency comb, the so-called *Kerr frequency combs* do not share this particular limitation. The generation of a Kerr frequency comb exploits the Kerr effect inside an optical resonator to produce a frequency comb from a continuous wave pump field, which is accurately described by the Lugiato-Lefever equation [79]. The tremendous advantage of this approach is that frequency combs can be produced around almost any given pump field that does not rely on a specific gain medium [80].

3.8.1 The Phase-Reduced Lugiato-Lefever Equation

In the field of pattern formation in nonlinear optics, the *Lugiato-Lefever model* is considered a paradigm, where the formation of localized structures such as optical pulses or solitons can be described by the model. The basic setup of the model consists of a cavity with a nonlinear optical medium that is driven by an external coherent pump field [79]. The *Lugiato-Lefever equation* describes the evolution of the intracavity field that arises in the setup presented [81]

$$\frac{\partial}{\partial t}A(t,\eta) = \mathrm{i}\sum_{k\geqslant 1}^{3}\frac{\zeta_k}{k!}\left(\mathrm{i}\frac{\partial}{\partial \eta}\right)^k A(t,\eta) - \mathrm{i}\Gamma\left|A(t,\eta)\right|^2 A(t,\eta) - \frac{\Delta\omega_0}{2}A(t,\eta), \tag{3.53}$$

where $A(t) \in \mathbb{C}$ denotes the time-dependent intracavity field, ζ_k are the normalized dispersion coefficients, $\eta \in [-\pi, \pi]$ is the angle that parametrizes the cavity length, Γ is the four-wave mixing gain coefficient, and $-\Delta\omega_0/2$ is a linear loss term. Significant amplification inside the cavity is possible for frequencies that are close to resonance with the cavity length. A discrete set of resonant cavity modes leads to the ansatz

$$A(t,\eta) = \sum_{p}^{N} A_p e^{\mathrm{i}(-p\eta+\phi_p(t))}, \tag{3.54}$$

where p is the mode index, A_p are the corresponding amplitudes, and ϕ_p are phase factors that include the effects of dispersion. Following [10] by inserting the discrete modal ansatz (3.54) in both sides of (3.53) leads to equations that describe the evolution of the phases and the amplitudes of all

discrete modes

$$\dot{\phi}_p = \sum_{k\geqslant 1}^{3} \frac{\zeta_k}{k!} (p)^k - \Gamma \sum_{l,m,n}^{N} A_{mp}^{ln} \delta_{mp}^{ln} \cos(\phi_{mp}^{ln}), \tag{3.55}$$

$$\dot{A}_p = -\frac{\Delta\omega_0}{2} - \Gamma \sum_{l,m,n}^{N} A_{mp}^{ln} \delta_{mp}^{ln} \sin(\phi_{mp}^{ln}), \tag{3.56}$$

where $\phi_{mp}^{ln} = \phi_l - \phi_m + \phi_n - \phi_p$, $A_{mp}^{ln} = \sqrt{A_l A_m A_n / A_p}$, and δ_{mp}^{ln} is a generalized Kronecker symbol that gives unity for $l + n - m - p = 0$, which is a constraint that refers to the conservation of energy. Under the assumption that the amplitudes of the emerging modes reach a steady state, a reduction to a phase model can be considered [10, 82]. As can be seen from (3.55), the resulting interaction terms in accordance with four-wave mixing and the conservation of energy include not only two-phase differences, like in the Kuramoto-type coupling, but combinations of four phases, which are considerably more complicated. Pulses obtained from a dissipative optical resonator, as it is modeled by the Lugiato-Lefever equation, are important for a wide range of applications. However, it should be noted that in models of passively mode-locked lasers [73, 75, 76], the nonlinearity responsible for the self-phase modulation can also adhere to a cubic form suggesting the involvement of similar dynamics.

3.8.2 A Qualitative Comparison of the Mode-Locking Phenomena

One of the central questions to ask is whether complicated phase interactions, including three or four different phases, are necessary for mode locking in phase oscillators. As it is demonstrated, the much simpler two-phase differences of the coupling in the Kuramoto model is already sufficient. This means that from the perspective of mode-locked oscillator systems, much simpler interaction functions than the one in (3.55) can be considered. The most important similarity between both models, (3.1) and (3.55), is perhaps the global nature of the interaction.

The frequency comb, whose formation is of great importance in optics, is considered as a supplied structural part in the model (3.1). Therefore, it is clear that effects that involve the generation of frequencies, like the four-wave mixing, cannot be covered by the model.

One of the most striking similarities between mode-locking in optics and in coupled phase oscillator models is the prolongation of the period by the interaction, which refers to $\Delta\Omega < \Delta\omega$ for an equidistant mode-locked solution

Def. 1. At the pulse peak of the mode-locked solution where $R_1(t)$ is maximal, the phases are pulled strongly towards the mean phase, which causes a prolongation of the total period. Similarly, a delay in the period of an optical pulse of a passively mode-locked laser appears because of the involvement of a saturable absorber. In this case, during each round trip the absorber is first non-transparent for the initial part of the pulse while it becomes saturated, and thus transparent for the later part. This has the similar effect of an increase in the inter-pulse interval length through the nonlinearity.

Another phenomenon that is known from mode-locked lasers is *pulse jittering*, which means that the pulse peaks and the inter-pulse intervals appear with small variation. An analog of this phenomenon is the appearance of chaotic mode-locked solutions, cf. Fig. 3.20.

Among the most important characteristics of optical pulses are the width and the shape of the pulse, which are influenced by multiple different quantities. The width of an optical pulse depends primarily on the number of frequencies present in the comb and the frequency spacing which is immediately transferable to mode-locked phase oscillators.

Quenched disorder and effects of dispersion are influential in the properties of optical pulses, therefore perturbations of the natural frequencies in (3.1) are considered. It is shown that adding quenched disorder to the equidistant natural frequencies (3.38), the system loses its ability to achieve pulses. A similar effect in optical fibers is the pulse degradation through small random contributions to the chromatic dispersion along the fiber [83]. The systematic variation of the natural frequencies (3.49) with dependance on the mode index was conceived in order to emulate the effects of dispersion, which turned out to have only a small effect on the pulse shape for mode-locked phase oscillators.

The modes of an optical pulse typically have a certain spectral width. A multimodal distribution of the natural frequencies is considered (3.50) for which numerically stable mode-locked solutions are obtained. By the presence of the second harmonic and a sufficiently large spectral width Q, one observes that the pulsed solution acts as a periodic forcing that has the ability to stimulate the mode locking of a secondary frequency comb, cf. Fig. 3.41. This results in a period doubling of the mode-locked solutions, which is similar to period doubling in mode-locked lasers.

4

Coherence Echoes and Mode Locking

"The ability to perceive or think differently is more important than the knowledge gained."

– David Bohm, *New Scientist*

This chapter is dedicated to the development of the correspondence between coherence echoes and mode locking. The coherence echo phenomenon was first reported for globally-coupled phase oscillators with Kuramoto-type coupling in [3]. A brief illustration of the basic response phenomenon is shown in Fig. 2.5. As a necessary ingredient to observe coherence echoes, it was found that at least two stimuli have to be applied to the incoherent state. Although the precise shape of the action function (2.36) of the stimuli is of minor importance in order to obtain the phenomenon, it was observed that a second harmonic contribution in the stimulus action function leads to qualitatively more distinct echoes. A recent experimental realization of the phenomenon in a system of stimulated chemical oscillators emphasizes its universal character [34].

It turns out that mode locking offers an intuitive way to explain the appearance of coherence echoes. The stimulation procedure induces a partially mode-locked state within a large population of oscillators which decays over time due to the stability of the incoherent state albeit recurrent increased levels of coherence are observed. It will be shown that the system configuration established by two stimuli indeed corresponds to a frequency comb structure which is mode-locked, and that the coherence echoes are remnants of such a partially mode-locked initial condition. Idealized mode-locked initial conditions are investigated to better understand the complicated echo phenomenon where the general non-monotonic character of the magnitudes of

the coherence echoes is revealed. To bridge between the partial and the idealized mode-locked initial conditions, sequences of stimuli at regular intervals are considered that progressively increase the level of modal synchronization and show the transition from a partial to a complete stimulated mode locking.

4.1 Globally-Coupled Phase Oscillators with Instantaneous Stimulation

The system equations without stimulating pulses have the form

$$\dot{\theta}_k = \omega_k + \frac{K}{N}\sum_{j=1}^{N}\left[\gamma\sin(\theta_j-\theta_k)+(1-\gamma)\sin(2(\theta_j-\theta_k))\right], \tag{4.1}$$

where k is the oscillator index, N is the total number of oscillators, K and γ are the coupling strength and the balancing parameter, respectively, and ω_k are the natural frequencies given by

$$\omega_k = \zeta_k, \quad k \in \{1,\ldots,N\}, \tag{4.2}$$

where ζ_k are independent random numbers drawn from a uniform distribution $\mathcal{U}(-1,1)$. The coupling strength is considered below the synchronization threshold $K < K_C$ such that the system evolves incoherently exhibiting small finite-size fluctuations that scale roughly like $R_1(t) \approx \mathcal{O}(1/\sqrt{N})$. When a stimulus impacts the system at the time $t = t_p$, the state of the system is changed by the following transformation rule

$$\theta_k(t_p^+) = \theta_k(t_p^-) - h(\theta_k(t_p^-)), \tag{4.3}$$

where $\theta_k(t_p^-)$ and $\theta_k(t_p^+)$ denote the phases of the oscillator with index k immediately before and after the stimulus.

Two different types of action functions $h(\cdot)$ are considered for the stimuli. The first is similar to what has been used in [3]

$$h_1(\theta) = \varepsilon(\alpha\sin(\theta)+(1-\alpha)\sin(2\theta)), \tag{4.4}$$

where ε is the amplitude and $\alpha \in [0,1]$ is an additional balancing between the contributions from both harmonics. This type of action function is particularly interesting in order to study the impact of the form of the stimulus by varying α. For the action functions (4.4), varying α changes not only the position of the maximum, but also influences its magnitude. For $\alpha > 2/3$ the

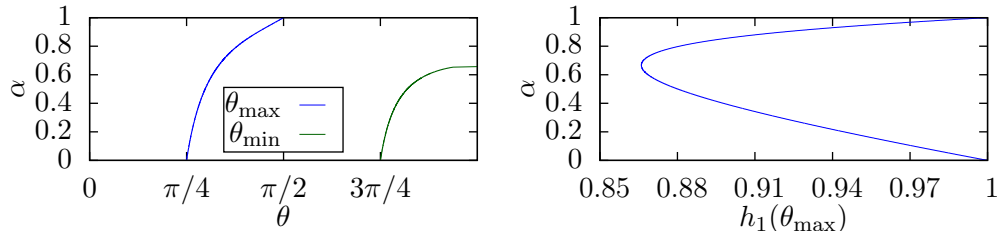

Figure 4.1: Changing the balancing α shifts the position of the maximum $\theta_{\max} = \{\theta \in [0,\pi) : \partial_\theta h_1(\theta) = 0, \max_{\theta\in[0,\pi)} h_1(\theta)\}$. For $\alpha < 2/3$ a minimum also appears at $\theta_{\min} = \{\theta \in [0,\pi) : \partial_\theta h_1(\theta) = 0, \min_{\theta\in[0,\pi)} h_1(\theta)\}$ within the interval $\theta \in [0,\pi)$. The right panel shows the corresponding value of $h_1(\alpha, \theta_{\max})$ with $\varepsilon = 1$.

function (4.4) has a single maximum at $\theta_{\max}$ within the interval $\theta \in [0,\pi]$, while for $\alpha < 2/3$ an additional minimum at $\theta_{\min}$ appears, see Fig. 4.1.

The second type of action function to be considered resets phases within a small interval of length 2ρ around $\theta = 0$ back to zero at the time of the impact

$$h_2(\theta) = \begin{cases} \theta, & |\theta| \leqslant \rho, \\ 0, & |\theta| > \rho, \end{cases} \tag{4.5}$$

where for the present formulation of $h_2(\cdot)$, θ are considered to be in interval $(-\pi,\pi]$. This particular type of stimulus synchronizes the oscillators either identically to zero, or leaves them unaffected.

4.1.1 Transport Pattern Resulting from a Single Stimulus

Applying a single stimulus to the system (4.1) at time $t = t_1$ results in a stripe pattern in the plot of (ω_k, θ_k), see Figs. 4.2 and 4.3, where the action functions (4.5) and (4.4) are used, respectively. It is necessary to understand this stripe pattern in order to explain the effect of a second stimulus at a later time.

The system with $N = 50 \cdot 10^3$ oscillators, natural frequencies according to (4.2), and $(K,\gamma) = (0.5, 1)$ is simulated, where at the time $t = t_1 = 50$, a single stimulus is applied. In both figures, the time traces $R_1(t)$, $R_2(t)$, and snapshots of (ω_k, θ_k) at the times $(t_0, t_1^+, t_2, t_3) = (0, 50^+, 53, 60)$ are presented.

Applying the action function (4.5) with $\rho = \pi/2$ results in a desolated region around a perfect phase synchronized stripe at $t = t_1^+$ immediately after the stimulus, where the oscillators that are reset to zero, those for which

$\left|\theta_k(t_1^-)\right| \leqslant \rho$, are colored in red, cf. Fig. 4.2. The stripe generated at t_1^+ has a vertical inclination and according to the natural frequencies, it tilts over time. In the case $K = 0$, the stripe's inclination β evolves according to

$$\beta(t) = \arccos(t/(t^2 + 1)), \tag{4.6}$$

which means that at any given time $t > t_1^+$, the stripe pattern is equidistant in ω with $\Delta\omega = 2\pi/(t_1 - t)$.

Note that for $K > 0$, one can observe a twisting of the stripe due to the nonlinear interaction. Although the twisting of the stripe can be strong, depending on $R_1(t_1^+)$ immediately after the stimulus and on K, as $R_1(t)$ decays rapidly, the evolution might be regarded as linear for the most part. The precise form of the twisting is due to the nonlinearity exerting a stronger effect on the oscillators that deviate more quickly from $\theta_k = 0$ after the stimulus. Over time the stripe wraps around the circle, which creates multiple stripes as depicted in the snapshot for $t = t_3$.

The effect of the nonlinear coupling is significant only shortly after the stimulus, when $R_1(t)$ is largest. This means that although there is in general some influence of the nonlinearity, at later times, the effects of the nonlinear coupling diminish and may potentially be discarded completely.

The action function h_1 (4.4) with $(\varepsilon, \alpha) = (1.0, 1.0)$ has an effect on all of the phases, which means that there will not be a completely desolated region after the stimulus. In this case, the coloring of the oscillators in the snapshots is as follows: oscillators with $\left|\theta_k(t_1^-)\right| \leqslant \theta_{\max}$ are colored in red. Especially in the snapshot at $t = t_2$, the twisting of the stripe can be identified.

4.1.2 Coherence Echoes Appearing After Two Stimuli

The coherence echo phenomenon, as presented in [3, 34], is a result of the application of two stimuli. For simplicity and in the prospect of application, the stimuli are taken to be identical. Following a first stimulus, applied at time $t = t_1^-$, a second stimulus at $t = t_2^-$ establishes the mode locking of an equidistant frequency comb within the whole oscillator population.

To identify the oscillators that are forming the frequency comb, the coloring of the oscillators is proceeded after the second stimulus. We denote an oscillator with index k as marked by a stimulus at t_1^- if $\left|\theta_k(t_1^-)\right| \leqslant \theta_{\max}$ in the case of h_1 and $\left|\theta_k(t_1^-)\right| \leqslant \rho$ in the case of h_2.

The oscillators that are marked for both stimuli create a *stimulated frequency comb* due to the presence of the equidistant stripe pattern generated after the first stimulus. The spacing of the frequency comb is $\Delta\omega = 2\pi/\tau$ with $\tau = t_2 - t_1$ being the time separation between the stimuli. The fre-

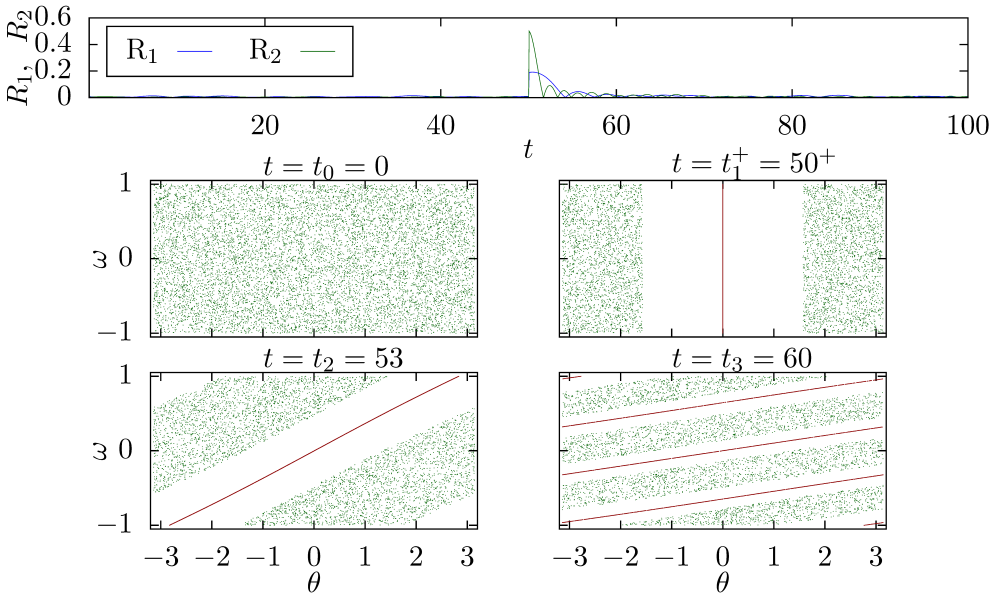

Figure 4.2: The system (4.1) with $(K, \gamma, N) = (0.5, 1.0, 50 \cdot 10^3)$ is simulated and a single stimulus h_2 (4.5) is applied with $\rho = \pi/2$ at $t_1^- = 50^-$. The time traces $R_1(t)$, $R_2(t)$, and snapshots of (ω_k, θ_k) at the times $(t_0, t_1^+, t_2, t_3) = (0, 50^+, 53, 60)$ are presented.

quency comb can be illustrated in a plot of (ω_k, θ_k) immediately after the second stimulus at $t = t_2^+$.

In the following examples with $N = 50 \cdot 10^3$ oscillators, the stimuli are applied at $t_1^- = 50^-$ and $t_2^- = 80^-$, with a coupling strength of $K = 0.5$, and only first harmonic coupling $\gamma = 1$. The stimulus types used are specified by $\rho = \pi/2$ and $(\varepsilon, \alpha) = (0.65, 0.5)$, in the respective cases for h_2 and h_1.

In Fig. 4.4 and Fig. 4.5, the time traces of $R_1(t)$ and $R_2(t)$ as well as snapshots of (ω_k, θ_k) at the times $(t_1^+, t_2^+, t_3, t_4) = (50^+, 80^+, 95, 110)$ are presented.

In the snapshot at $t = t_1^+$, the coloring is green for the unmarked and red for the marked oscillators at $t = t_1^-$. After the second stimulus at $t = t_2^+$, additional coloring is applied only to the oscillators that are marked at $t = t_2^-$, where red becomes blue and green becomes purple.

The stimulated frequency comb is now given as the set of the blue oscillators after $t = t_2^+$. Comparing the snapshots at $t = t_2^+$ for the two different stimuli h_1 and h_2, one sees that the stimulated frequency comb generated with h_2 is sharp in θ due to the phase resetting character, while for h_1, it remains connected to the initial stripe pattern.

In the snapshot at $t = t_3$, which corresponds to the time $t = t_2 + \tau/2$, one

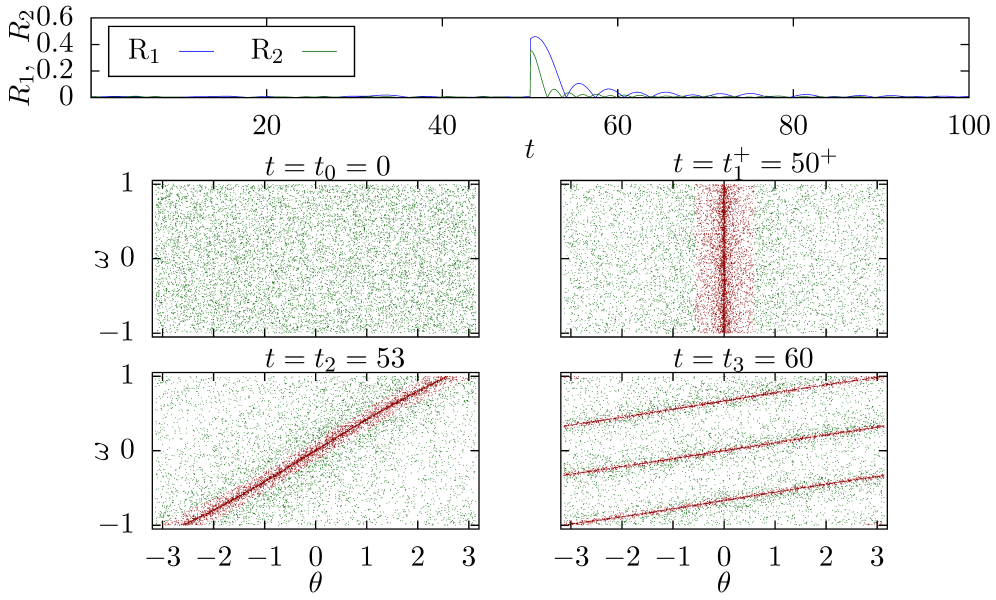

Figure 4.3: The system (4.1) with $(K, \gamma, N) = (0.5, 1.0, 50 \cdot 10^3)$ is simulated and a single stimulus h_1 (4.4) is applied with $(\varepsilon, \alpha) = (1, 1)$ at $t_1^- = 50^-$. The time traces $R_1(t)$, $R_2(t)$, and snapshots of (ω_k, θ_k) at the times $(t_0, t_1^+, t_2, t_3) = (0, 50^+, 53, 60)$ are presented.

can see that the stimulated frequency comb is the reason for the increase in $R_2(t)$. In the final snapshots at $t = t_4$, denoting the time of the first coherence echo, one sees how the blue stripes are alined in phase, independently of whether h_1 or h_2 is used. In this way, the mode-locking picture gives an intuitive explanation for the appearance of the coherence echo. When one compares the blue stripes in the snapshots at $t = t_2^+$ and $t = t_4$, one sees that a spreading occurs, which is attributed mostly to the linear dispersion.

4.2 Synthetic Mode-Locked Initial Conditions

The system state that is prepared after the two stimuli at $t = t_1$ and $t = t_2$ is only a partially mode-locked state because not all oscillators that have natural frequencies matching those of the blue group are phase synchronized at $t = t_2^+$, see snapshot Fig. 4.4.

In the following, the echo phenomenon is investigated by employing a special so-called *synthetic mode-locked initial condition*. After preparation of this initial condition, a sequence of echoes can be observed in a simulation.

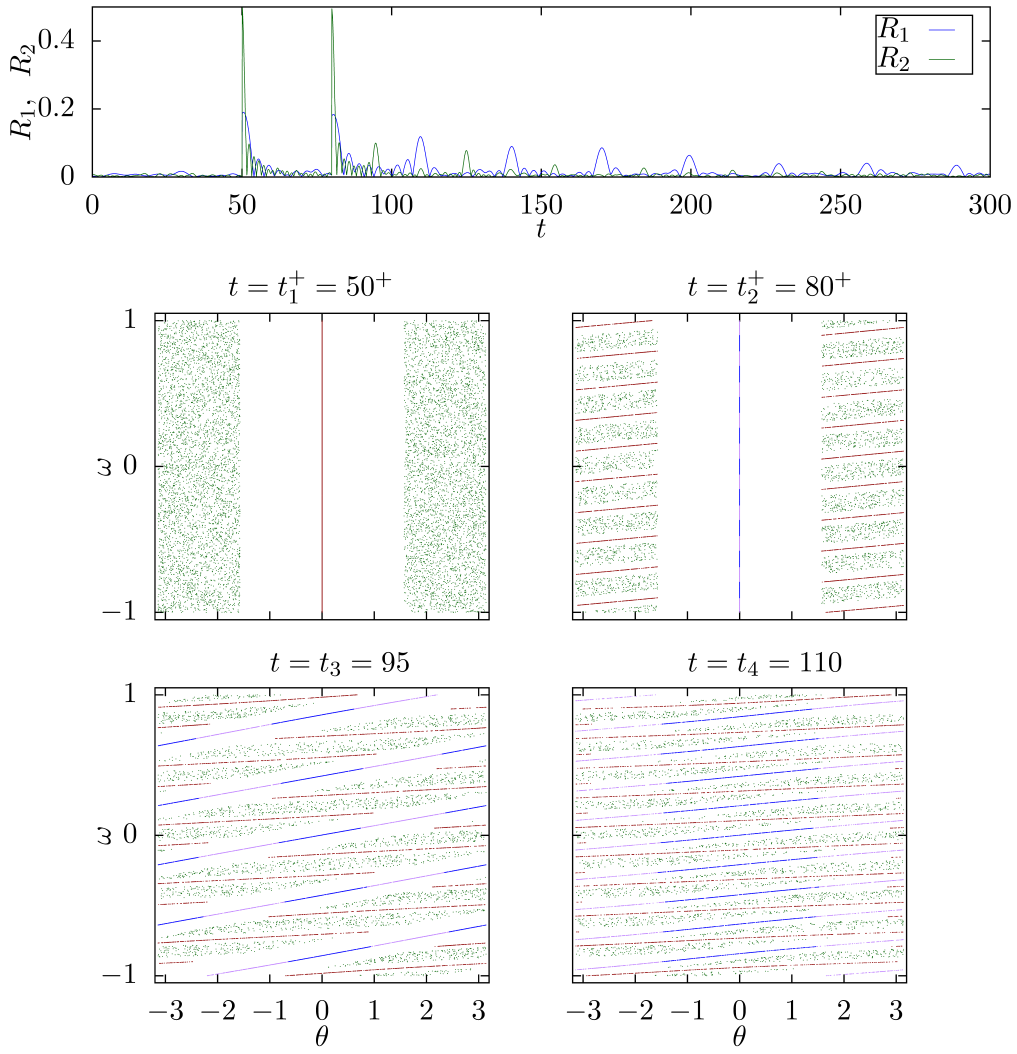

Figure 4.4: The system (4.1) with $(K, \gamma, N) = (0.5, 1.0, 50 \cdot 10^3)$ is simulated and stimuli h_2 (4.5) with $\rho = \pi/2$ are applied at $t_1^- = 50^-$ and $t_2^- = 80^-$. The time traces $R_1(t)$, $R_2(t)$, and snapshots of (ω_k, θ_k) at the times $(t_1^+, t_2^+, t_3, t_4) = (50^+, 80^+, 95, 110)$ are presented. Coloring for $t \geqslant t_2$: $\left|\theta_k(t_1^-)\right| \leqslant \rho$ and $\left|\theta_k(t_1^-)\right| \leqslant \rho$ (blue), $\left|\theta_k(t_1^-)\right| > \rho$ and $\left|\theta_k(t_1^-)\right| \leqslant \rho$ (purple).

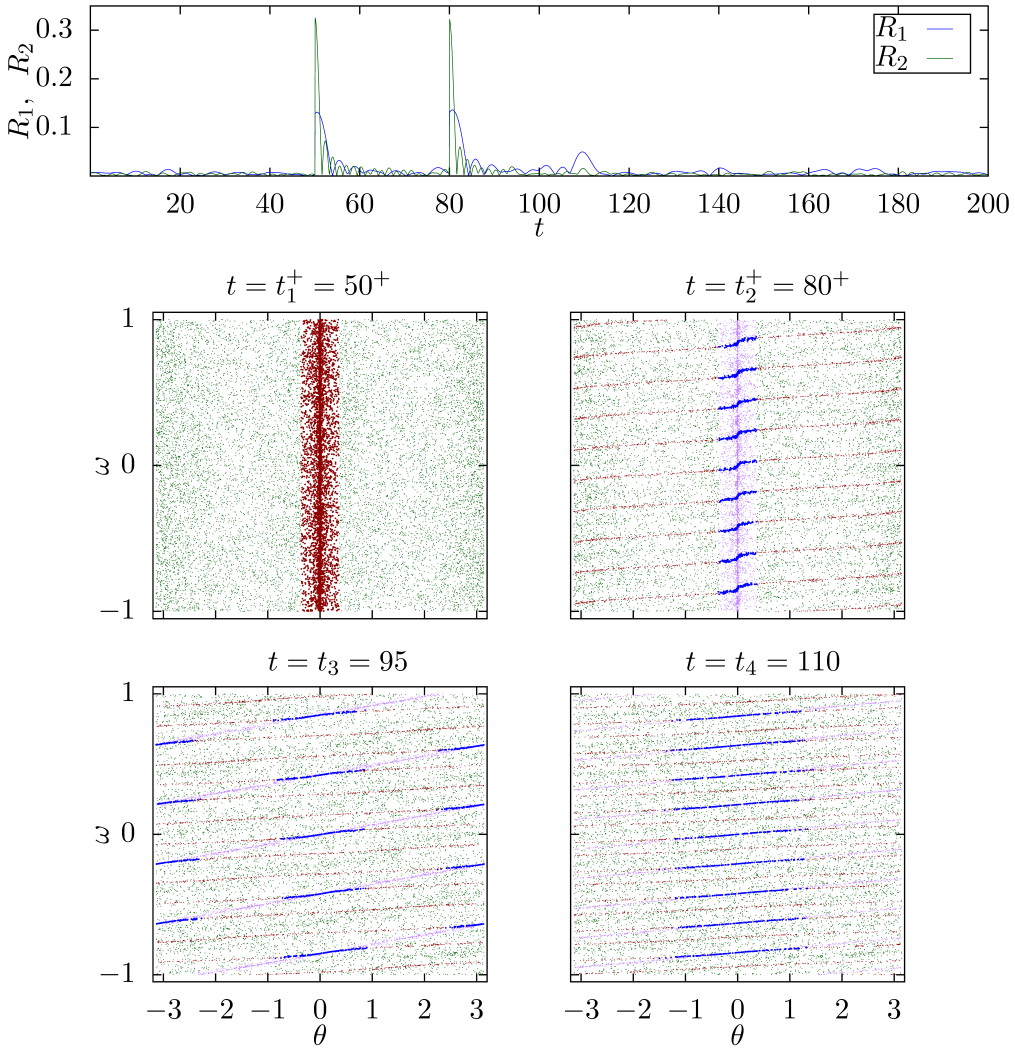

Figure 4.5: The system (4.1) with $(K, \gamma, N) = (0.5, 1.0, 50 \cdot 10^3)$ is simulated and stimuli h_1 (4.4) with $(\varepsilon, \alpha) = (0.65, 0.5)$ are applied at $t_1^- = 50^-$ and $t_2^- = 80^-$. The time traces $R_1(t)$, $R_2(t)$, and snapshots of (ω_k, θ_k) at the times $(t_1^+, t_2^+, t_3, t_4) = (50^+, 80^+, 95, 110)$ are presented. Coloring for $t \geqslant t_2$: $\left|\theta_k(t_1^-)\right| \leqslant \theta_{\max}$ and $\left|\theta_k(t_2^-)\right| \leqslant \theta_{\max}$ (blue), $\left|\theta_k(t_1^-)\right| > \theta_{\max}$ and $\left|\theta_k(t_2^-)\right| \leqslant \theta_{\max}$ (purple).

Definition 5. *The synthetic mode-locked initial conditions are given by*

$$\theta_k(0) = \begin{cases} 0, & \text{for} \quad \omega_k \in M \\ \theta_k \in [-\pi, \pi], & \text{uniform}, \end{cases} \tag{4.7}$$

where $k \in \{1, \ldots, N\}$ is the oscillator index. The oscillators with $\omega_k \in M$ form a mode comb

$$M := \cup_{j=-n}^{n} M_j, \quad \text{with} \quad M_j := [j\Delta\omega - \Delta_m, j\Delta\omega + \Delta_m], \tag{4.8}$$

where $j \in \{-n, \ldots, n\}$ is called the mode index, $\Delta\omega$ is the equidistant frequency spacing between the modes, and $2\Delta_m$ is the spectral width of each mode with $2\Delta_m < \Delta\omega$. The oscillator with index k belongs to mode j if $|\omega_k - j\Delta\omega| \leqslant \Delta_m$.

The number of oscillators present in each mode depends on the chosen frequency distribution $g(\omega)$ as well as on the comb parameters $(\Delta\omega, \Delta_m)$. The frequency distribution taken here is uniform, covering the interval $(-1.02, 1.02)$ and the comb parameters are $(\Delta\omega, \Delta_m) = (0.1, 0.02)$. The peculiar range of the frequency distribution is such that the edge modes with indices n and $-n$ are fully supported. The frequency spacing together with the range of the frequency distribution fixes the number of modes that are populated with oscillators to $2n + 1 = 21$.

An example of the time evolution of the synthetic mode-locked initial condition described with system parameters $(K, \gamma, N) = (0.95, 0.7, 5 \cdot 10^4)$ is shown in Fig. 4.6, where the time traces $R_1(t)$, $R_2(t)$ together with snapshots of (ω_k, θ_k) at the times $(t_0, t_1, t_2, t_3) = (0, 0.91, 32.48, 64.11)$ are presented. In the snapshots, the oscillators colored in red belong to the prescribed mode comb with frequencies $\omega_k \in M$.

One sees that the synthetic mode-locked initial conditions produce an echo type phenomenon in $R_1(t)$ comparable with the echoes found after stimulation. The two main differences are that the underlying linear transport pattern as a remnant of the first stimulus is not present and that the modes contain all the oscillators with matching natural frequencies.

The magnitudes of the echoes are not behaving monotonously, which is demonstrated in the example, see Fig.4.6, where the third echo is absent, while at later times, echoes appear with considerable magnitude.

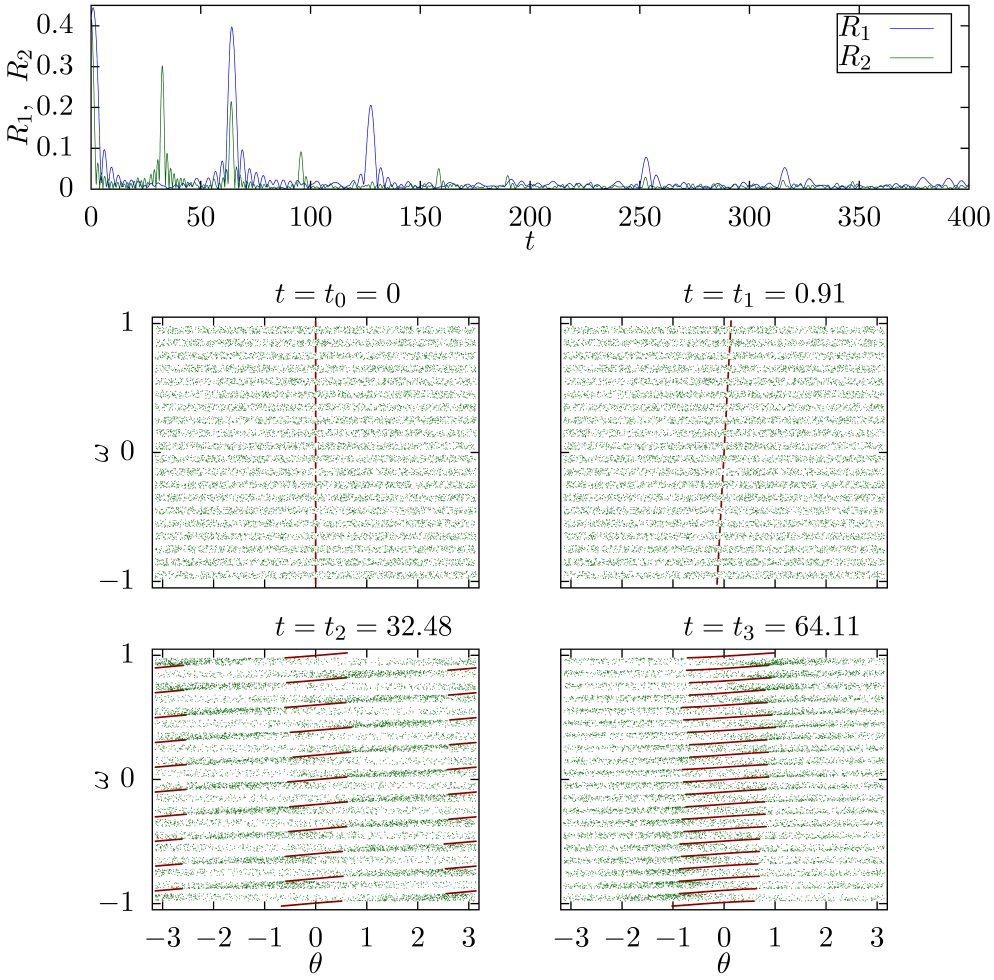

Figure 4.6: Time traces $R_1(t)$, $R_2(t)$, and snapshots of (ω_k, θ_k) at the times $(t_0, t_1, t_2, t_3) = (0, 0.91, 32.48, 64.11)$ are presented. The initial state at $t = t_0$ is a synthetic mode-locked initial condition, cf. Def. 5 with $(\Delta\omega, \Delta_m) = (0.1, 0.02)$, and the system parameters are given by $(K, \gamma, N) = (0.95, 0.7, 5 \cdot 10^4)$.

4.2.1 Non-Monotonously Decaying Echoes of the Synthetic Mode-Locked Initial Conditions

To understand the demonstrated non-monotonous behavior of the magnitude of the echoes, cf. Fig. 4.6, the uncoupled system with $K = 0$ for the same synthetic mode-locked initial conditions Def. 5 with $(\Delta\omega, \Delta_m) = (0.1, 0.02)$ is investigated here. For this purpose we define the *complex modal order parameters* as

$$\eta_{1,j}(t) = R_{1,j}(t)e^{\mathrm{i}\Psi_{1,j}(t)} := \frac{1}{N_j}\sum_{k \text{ if } \omega_k \in M_j} e^{\mathrm{i}\theta_k(t)}, \tag{4.9}$$

where N_j is the total number of oscillators in the jth mode for which it holds that $\omega_k \in [j\Delta\omega - \Delta_m, j\Delta\omega + \Delta_m]$.

In the continuum limit ($N_j \to \infty$), (4.9) can be computed explicitly as

$$R_{1,j}(t)e^{\mathrm{i}\Psi_{1,j}(t)} = \int_{-\infty}^{\infty} d\omega \int_0^{2\pi} e^{\mathrm{i}\theta} F_j(\theta, \omega, t) d\theta, \tag{4.10}$$

where $F_j(\theta, \omega, t)$ is the distribution function for the oscillators of the jth mode. The distribution function is further normalized

$$\int_0^{2\pi} F_j(\theta, \omega, t) d\theta = g_j(\omega), \tag{4.11}$$

where $g_j(\omega)$ is the frequency distribution of the jth mode that is uniform and normalized

$$g_j(\omega) = \begin{cases} \frac{1}{2\Delta_m}, & \text{for} \quad \omega \in M_j, \\ 0, & \text{else.} \end{cases} \tag{4.12}$$

The initial data at time $t = t_0 = 0$ for all oscillators of the jth mode is $\theta_k(t_0) = 0$. Because there is no interaction, one can readily write down the evolution of the distribution function on the universal cover $\theta \in \mathbb{R}$

$$F_j(\theta, \omega, t) = \begin{cases} g_j(\omega)\frac{1}{2\Delta_m t}, \text{ for } \theta \in [(j\Delta\omega - \Delta_m)t, (j\Delta\omega + \Delta_m)t], \\ 0, \quad \text{else.} \end{cases} \tag{4.13}$$

Hence, the jth complex modal order parameter becomes

$$\begin{aligned} R_{1,j}(t)e^{\mathrm{i}\Psi_{1,j}(t)} &= \int_{-\infty}^{\infty} d\omega \int_{-\infty}^{\infty} e^{\mathrm{i}\theta} g_j(\omega) \frac{1}{2\Delta_m t} d\theta \\ &= \frac{1}{2\Delta_m t}\frac{1}{\mathrm{i}}\left[e^{\mathrm{i}(j\Delta\omega+\Delta_m)t} - e^{\mathrm{i}(j\Delta\omega-\Delta_m)t}\right], \end{aligned} \tag{4.14}$$

The total complex order parameter in the continuum limit for the synthetic mode-locked initial conditions Def. 5 can be computed using (4.14)

$$R_1(t)e^{\mathrm{i}\Psi_1(t)} = A\frac{1}{2n+1}\sum_{j=-n}^{n}\frac{1}{2\Delta_m t}\frac{1}{\mathrm{i}}\left[e^{\mathrm{i}(j\Delta\omega+\Delta_m)t} - e^{\mathrm{i}(j\Delta\omega-\Delta_m)t}\right], \qquad (4.15)$$

where A corresponds to the fraction of oscillators of the system that forms the mode comb.

The results of a simulation of the synthetic mode-locked initial condition Def. 5 with $(\Delta\omega, \Delta_m) = (0.1, 0.02)$ and the system parameters $(K, N) = (0, 5 \cdot 10^4)$ are presented in Fig. 4.7. The time traces $R_1(t)$, $R_2(t)$, and $R_{1,j}(t)$ (4.9) for $j \in \{-10, -8, -6, -4, -2, 0\}$ are plotted together with the results from the continuum limit (4.15) and (4.14). One sees from (4.14) that the phases of the modal order parameters $\Psi_{1,j}(t)$ become identical at times $t = t_p = p\frac{2\pi}{\Delta\omega}$ with $p \in \mathbb{N}$ at which times the modes interfere constructively. Furthermore, phase flips of $\Psi_{1,j}(t)$ by π occur at the times $t = t_q = q\frac{2\pi}{2\Delta_m}$ with $q \in \mathbb{N}$, when (4.9) go through zero. Combining these two conditions one can explain the absence of the fifth echo in $R_1(t)$ by the coincidence of both

$$\frac{p}{q} = \frac{\Delta\omega}{2\Delta_m}, \qquad (4.16)$$

which is fulfilled by the used parameter values for the fifth echo $p = 5$ and the second phase flip $q = 2$.

That the nonlinear coupling indeed has a crucial effect on the echoes can be seen in Fig. 4.8, where $R_1(t)$, $R_2(t)$, and $R_{1,j}(t)$ are presented for the system specified by $(K, \gamma, N) = (0.95, 0.7, 5 \cdot 10^4)$. The decrease of $R_{1,j}(t)$ is radically altered by the first two echoes, where $R_1(t)$ is the largest. The rates at which the modes disperse become smaller due to the increase of the modal synchronization during the pulses. While the decrease of $R_{1,j}(t)$ varies significantly for different j, one may notice that even so the third echo vanishes the modal order parameters are of considerable magnitude. This means that the modal phases $\Psi_{1,j}(t)$ are not aligned to interfere constructively.

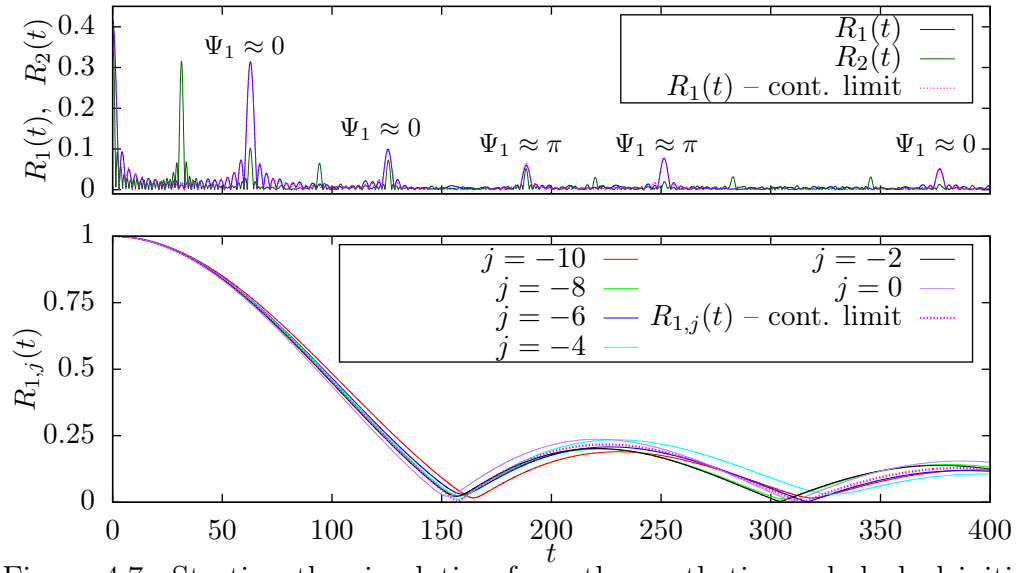

Figure 4.7: Starting the simulation from the synthetic mode-locked initial condition Def. 5 with $(\Delta\omega, \Delta_m) = (0.1, 0.02)$ and $(K, N) = (0, 5 \cdot 10^4)$, the time traces $R_1(t)$, $R_2(t)$, and $R_{1,j}(t)$ (4.9) for $j \in \{-10, -8, -6, -4, -2, 0\}$ as well as the results for the continuum limit (4.15) and (4.14) are presented.

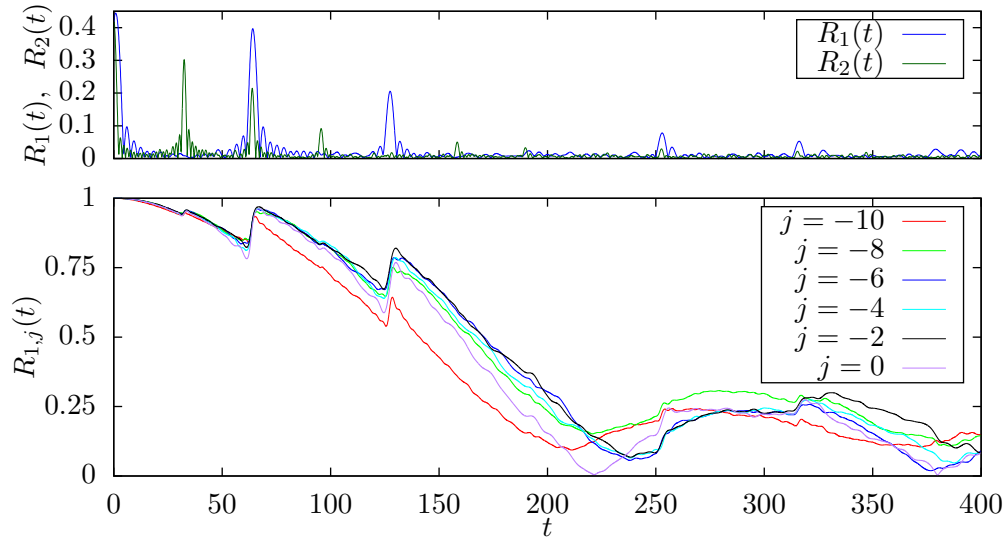

Figure 4.8: Starting the simulation from the synthetic mode-locked initial condition Def. 5 with $(\Delta\omega, \Delta_m) = (0.1, 0.02)$ and $(K, \gamma, N) = (0.95, 0.7, 5 \cdot 10^4)$, cf. Fig. 4.6, the time traces $R_1(t)$, $R_2(t)$, and $R_{1,j}(t)$ (4.9) for $j \in \{-10, -8, -6, -4, -2, 0\}$ are presented.

4.2.2 Influence of the Global Coupling on the Synthetic Mode-Locked Initial Conditions

While the complex behavior of the magnitude of the echoes has been demonstrated and fully explained for the case $K = 0$, it is shown in Fig. 4.8 that there is a significant impact by the nonlinear coupling. Simulations of the synthetic initial condition with $(\Delta\omega, \Delta_m) = (0.1, 0.02)$ are systematically performed for a system with $N = 5 \cdot 10^4$ and random independent uniform natural frequencies $g(\omega) = \mathcal{U}(-1, 1)$.

The ratio $R_1(t_1)/R_1(t_3)$ and the recurrence time $\tau = t_3 - t_1$ for varying coupling strength K and balancing factor γ are presented in Fig. 4.9. Note that the first maximum of $R_1(t)$ occurs shortly after the initialization at $t = t_1$. For fixed $\gamma = 0.7$ (top panel), a minimal ratio $R_1(t_1)/R_1(t_3)$ appears at intermediate coupling strength values ($K \approx 0.9$). For varying γ (bottom panel) at fixed $K = 0.95$, the magnitude of the echo increases considerably when both harmonics are present. The timings ($\tau = t_3 - t_1$) (right panels) are clearly depending on the coupling strength K and the balancing of the harmonics γ with a minimum at $\gamma \approx 2/3$, cf. Fig. 4.9. Although this clarifies the influence of the nonlinear coupling on the synthetic mode-locked initial conditions to a certain extent, it should be noted that such initial states are idealized in the sense that the modal order parameters are initialized to $R_{1,j}(0) = 1$. Surprisingly, one observes that the synthetic mode-locked initial conditions allow for the ratio $R_1(t_1)/R_1(t_3) < 1$, meaning that the first echo even exceeds the initial state's coherence.

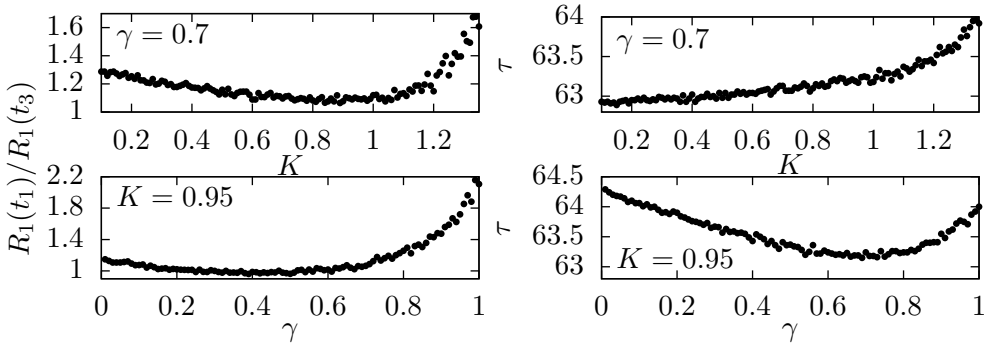

Figure 4.9: Simulations of the synthetic mode-locked initial condition Def. 5 with $(\Delta\omega, \Delta_m) = (0.1, 0.02)$ for $N = 5 \cdot 10^4$ oscillators are presented by plotting the ratio of the maximum after initialization $R_1(t_1)$ and the first echo $R_1(t_3)$, as well as recurrence times $\tau = t_3 - t_1$ for all the parameter values used.

4.3 Stimulated Mode-Locked Solutions

The synthetic mode-locked initial conditions and the initial state obtained after two stimuli are mostly different with respect to the level of modal synchronization. For the synthetic initial state, all oscillators of a prescribed mode comb Def. 5 are initially at identical phases while with two stimuli, only a partially mode-locked state is formed.

In the following, a train of stimuli is applied to the system at regular intervals of length τ, which is considered a natural extension to the application of two stimuli. The train of stimuli is implemented by applying the mapping of the phases with $h_1(\cdot)$ or $h_2(\cdot)$ at times $t = p\tau = t_p$ with $p \in \mathbb{N}$ giving

$$\theta_k((p\tau)^+) = \theta_k((p\tau)^-) + h_{1,2}(\theta_k((p\tau)^-)), \tag{4.17}$$

where $k \in \{1, \ldots, N\}$ is the oscillator index, $(p\tau)^-$, and $(p\tau)^+$ denote the times immediately before and after the stimuli, respectively.

The repetitive stimulation of the form described brings the system into a so-called *stimulated mode-locked state* where the main difference with the application of just two stimuli is the emergence of a fully locked mode comb in contrast to a partially locked mode comb. Periodically stimulated systems appear in a variety applications, which makes it particularly interesting to study the stimulated mode-locked solutions.

4.3.1 Accumulation of a Stimulated Fully-Locked Mode Comb

Periodic simulation of the system (4.1) with $(K, \gamma, N) = (0.95, 2/3, 5 \cdot 10^4)$ at times $t = p\tau = t_p$ with $\tau = 30$ for (4.5) h_2 with $\rho = \pi/8$ is performed and the simulation results are presented in Fig. 4.10. One sees that the magnitude of the stimulated pulses $R_1(t_p^+)$ increases over time and further, that the maxima synchronize with the stimulation times (dotted lines). In a series of snapshots of (ω_k, θ_k) at times $t \in \{t_1, t_5, t_{15}, t_{30}\}$ the formation of thin desolated horizontal regions is observed. The oscillators with the corresponding natural frequencies form a *stimulated mode comb* that resembles the mode comb from Def. 5.

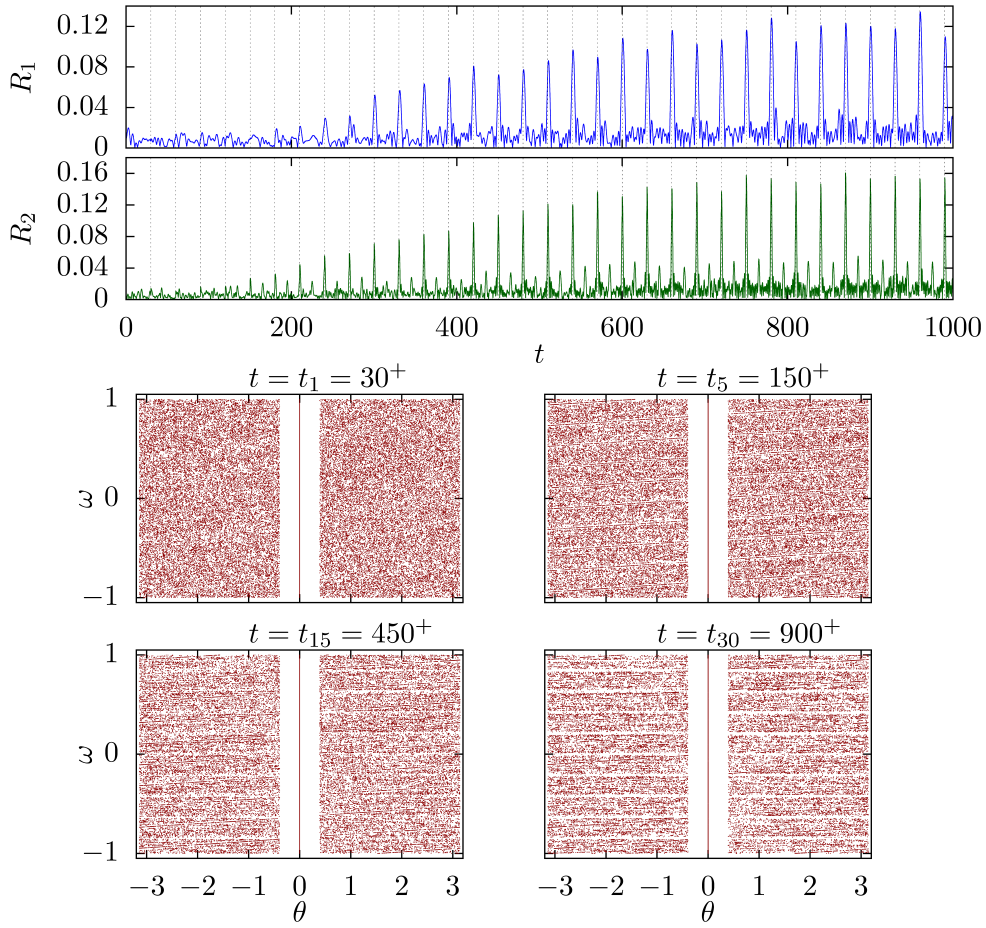

Figure 4.10: Time traces $R_1(t)$ and $R_2(t)$ of a stimulated mode-locked solution excited by a pulse train (4.5), h_2 with $\rho = \pi/8$, and $\tau = 30$. The system (4.1) with $(K, \gamma, N) = (0.95, 2/3, 5 \cdot 10^4)$ and independent random natural frequencies ω_k sampled from the uniform distribution $\mathcal{U}(-1, 1)$ are initialized at uniform initial conditions. Snapshots of (ω_k, θ_k) at four different times $t \in \{t_1, t_5, t_{15}, t_{30}\}$ demonstrate the accumulative process.

4.3.2 Stimulated Mode Locking and Circle Maps

It is of primary interest to access the magnitude of the modulus of the order parameter $R_1(p\tau^+)$ at times $t = p\tau^+$ immediately after the stimuli. In the following, the coupling strength is set to zero ($K = 0$) such that for each oscillator, the phase evolution for increasing p is given by a circle map of the form

$$\theta_k((p+1)\tau^+) = \theta_k(p\tau^+) + \omega_k\tau - h_{1,2}(\theta_k(p\tau^+) + \omega_k\tau) \mod 2\pi, \quad (4.18)$$

with $k \in \{1, \ldots, N\}$ and $h_{1,2}(\cdot)$ denoting either kind of stimulus action functions (4.4) or (4.5).

Arnold circle maps

By taking h_1 with $(\alpha, \varepsilon) = (1, \varepsilon)$ in (4.18), one obtains an Arnold circle map (2.26) for each oscillator, where ε corresponds to the strength of the nonlinearity. Therefore one can expect that in dependence on ε, Arnold tongues emerge from the set of natural frequencies that are rationally related to the forcing frequency $\omega_f = 1/\tau$.

One important observation at this point is that although the effective frequencies form a Devil's staircase independent of the initial conditions [30], see Fig. 4.11 (a), the resulting pulse pattern $R_1(p\tau^+)$ depends crucially on the chosen initial conditions. For the system (4.18) with $N = 5 \cdot 10^5$, $\tau = 30$, and h_1 with $(\alpha, \varepsilon) = (1, 0.5)$, the corresponding $R_1(p\tau^+)$ are presented starting from identical and uniform initial conditions, (b) Fig. 4.11, respectively. One sees a clear difference in the pulse heights $R_1(p\tau^+)$ and the variations depending on the chosen initial conditions. The oscillators that are subharmonically locked with the stimuli (small plateau), see inset Fig. 4.11 (a), appear at only every second stimulus with the same phase. This means that in particular, they can be in either one of the positions at the times $p\tau^+$ for uniform initial conditions while they have to be in the same for identical initial conditions, which explains the larger variations in $R_1(p\tau^+)$.

Taking a second harmonic contribution into the stimuli ($\alpha = 0.5$) results in a stronger build-up regime where the corresponding pulsation strength increases over time, see Fig. 4.12. Furthermore, one observes that the subharmonic plateaus in the staircase increase in width relative to the harmonic ones.

Discontinuous circle maps

The second stimulus type (4.5) in comparison has different characteristics because of its discontinuity, which can have important implications on the response to the stimulation. While the existence and uniqueness of the rotation number for circle maps with discontinuities was proven in [84] in the context of set-valued maps, it will be enough at this point to identify some of the features that arise due to (4.5).

The first observation one can make for applying (4.5) periodically is that when ω_k is an integer multiple of the forcing frequency $\omega_f = 1/\tau$ (harmonic resonances) after applying the first stimulus, a fixed point is reached. For rationally related ω_k such that $p\omega_k = q\omega_f$ where p, q are coprime as in (2.28)

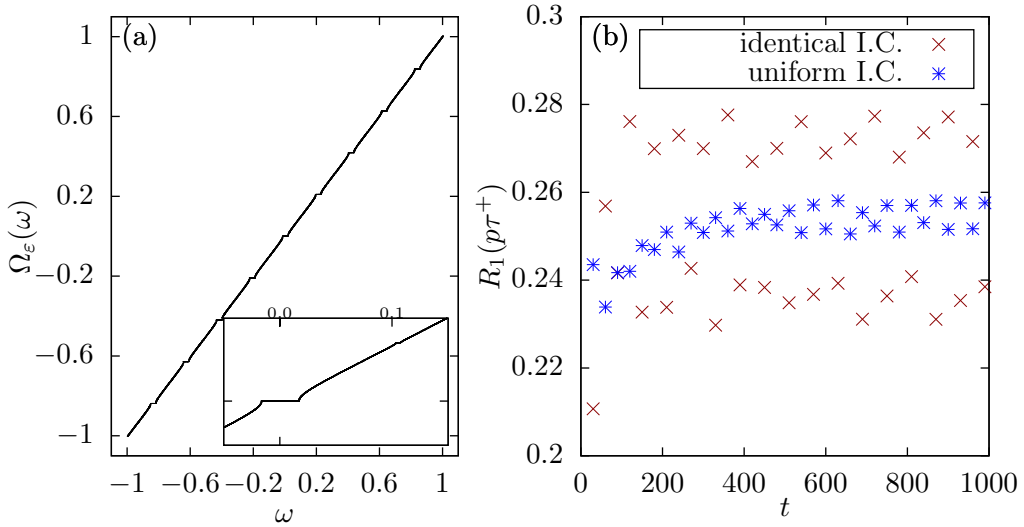

Figure 4.11: The system (4.18) with $N = 5 \cdot 10^5$, $\tau = 30$, and h_1 with $(\alpha, \varepsilon) = (1, 0.5)$ is iterated. Panel (a) shows the resulting effective frequencies $\Omega_\varepsilon(\omega)$ forming a Devil's staircase. Panel (b) shows $R_1(p\tau^+)$ for the initial iterates.

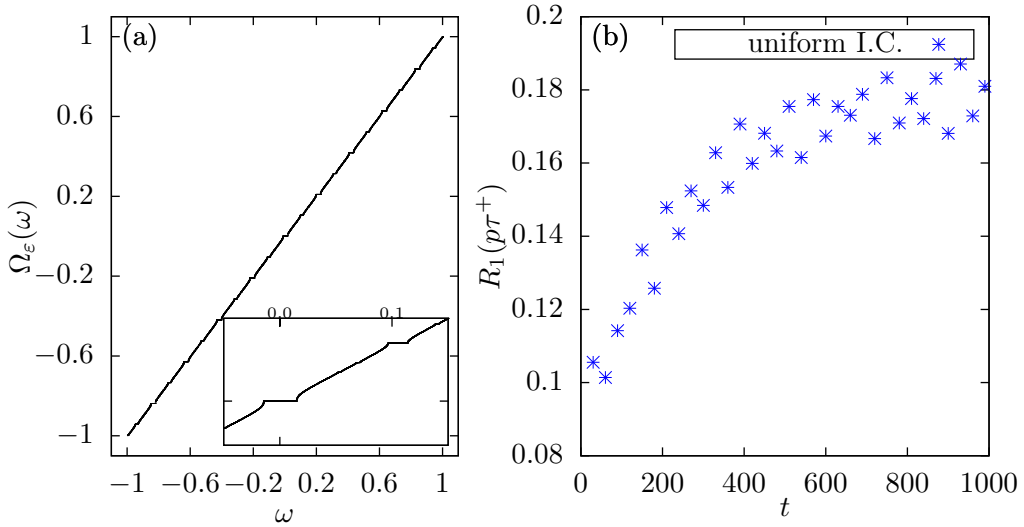

Figure 4.12: The system (4.18) with $N = 5 \cdot 10^5$, $\tau = 30$, and h_1 with $(\alpha, \varepsilon) = (0.5, 0.5)$ is iterated. Panel (a) shows the resulting effective frequencies $\Omega_\varepsilon(\omega)$ forming a Devil's staircase. Panel (b) shows $R_1(p\tau^+)$ for the initial iterates.

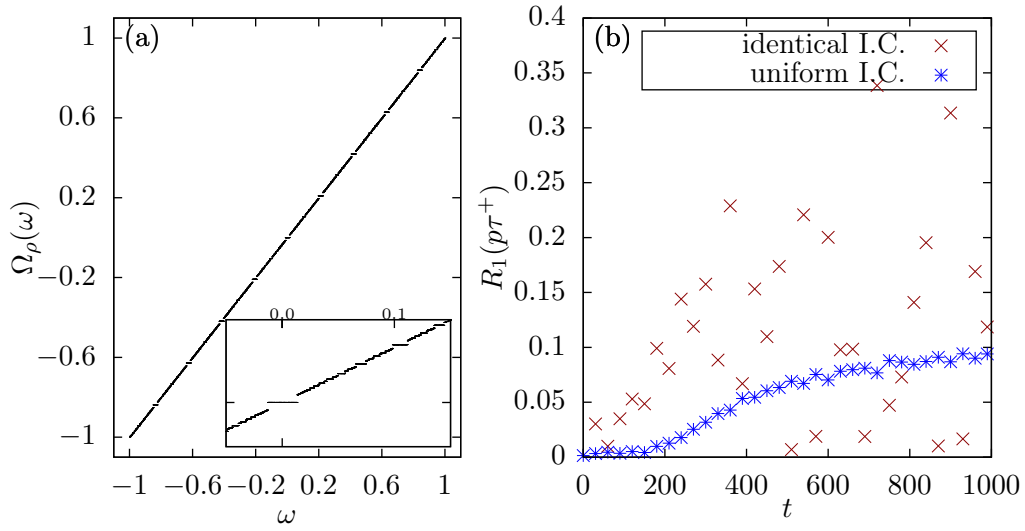

Figure 4.13: The system (4.18) with $N = 5 \cdot 10^5$, $\tau = 30$, and h_2 with $\rho = \pi/8$ is iterated. Panel (a) shows the resulting effective frequencies $\Omega_\rho(\omega)$. Panel (b) shows $R_1(p\tau^+)$ for the initial iterates.

with $p < q < i$, the periodic point of the map is reached after at most i iterates. For non-resonant ω_k the situation is different, and it depends on the initial condition $\theta_k(0^-)$ and on the exact relationship between ω_k and the forcing frequency when a periodic point will be reached first. It is clear that the non-resonant ω_k will eventually be mapped to zero, as they all correspond to rotations with irrational rotation numbers (without stimulation). This means that after an initial transient, all maps will reach a periodic orbit and there will be no irrational rotation numbers. Accordingly, $\Omega_\rho(\omega)$ becomes discontinuous. An example for h_2 with $\rho = \pi/8$, $\tau = 30$, and $N = 5 \cdot 10^5$ is given in Fig. 4.13. Here, the importance of the initial condition for $R_1(p\tau^+)$ is especially apparent from the strong variations in the pulses for identical initial conditions.

Subsequent echoes after termination of the stimulation

For the periodically forced system, it has already been demonstrated that over time, a fully mode-locked comb is developed, cf. Fig. 4.10. When the periodic stimulation is discontinued, one observes a subsequent disaggregation of the mode comb which is accompanied by echoes.

For the stimulation with (4.5), an emergent mode comb is found that adequately explains the pulsation pattern $R_1(p\tau^+)$. The oscillators that are locked in the stimulated mode comb fulfill

$$\omega_k \in M := \cup_j M_j, \quad M_j := [\Delta\omega j - \Delta_m, \Delta\omega j + \Delta_m], \tag{4.19}$$

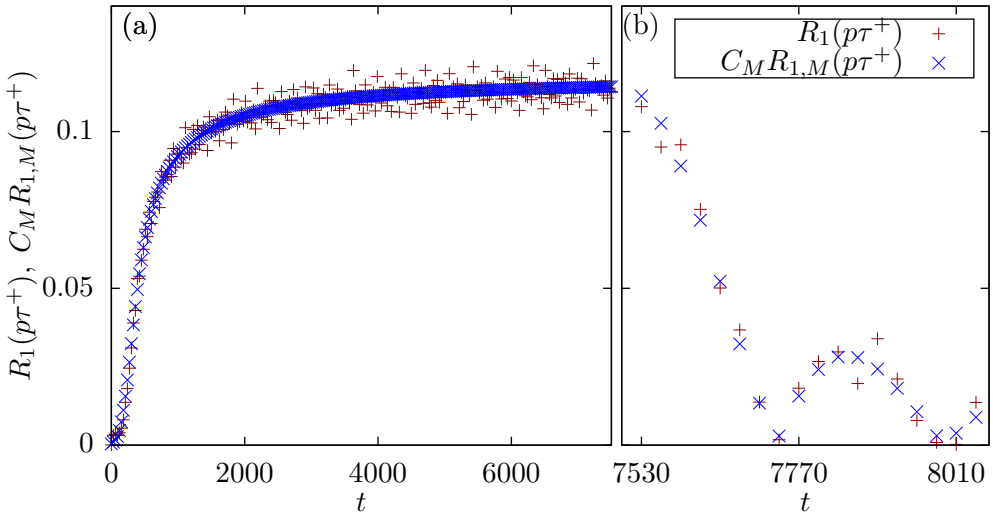

Figure 4.14: The system (4.18) with $N = 5 \cdot 10^5$, $\tau = 30$, and h_2 with $\rho = \pi/8$ is iterated. Panel (a) and (b) during and after the stimulation has ended, respectively. The normalized order parameter of (4.19) $C_M R_{1,M}(p\tau^+)$ and $R_1(p\tau^+)$ are plotted. The normalization C_M is obtained as the number of oscillators in the comb relative to system size N.

where $\Delta\omega = 2\pi/\tau$ is the equidistant spacing, $j \in \mathbb{Z}$ is the mode index, and $\Delta_m = \rho/\tau$ is the spectral width. The stimulated mode comb is similar to the one given in Def. 5.

The system (4.18) with $N = 5 \cdot 10^5$, $\tau = 30$, and h_2 with $\rho = \pi/8$ is iterated, where the stimulation is discontinued after $p = 250$. The modulus of the order parameter for the comb (4.19) $R_{1,M}(p\tau^+)$ is computed and appropriately normalized to $C_M R_{1,M}(p\tau^+)$, where C_M is obtained as the number of oscillators in the comb relative to system size N. One observes a close resemblance with the response in the total order parameter $R_1(p\tau^+)$ after the stimulation has ended, which shows that the echoes originate substantially from the stimulated mode comb, see Fig. 4.14.

4.3.3 Effect of the Global Interaction on Stimulated Mode-Locked States

In addition to the complicated structures found for $(K = 0)$, the impact of the coupling on the stimulated mode locking is investigated here. It is found that the global interaction increases the response to the stimulation.

In contrast to iterating the circle maps (4.18), studying the system (4.1) increases the time needed for adequate simulations significantly. To limit the

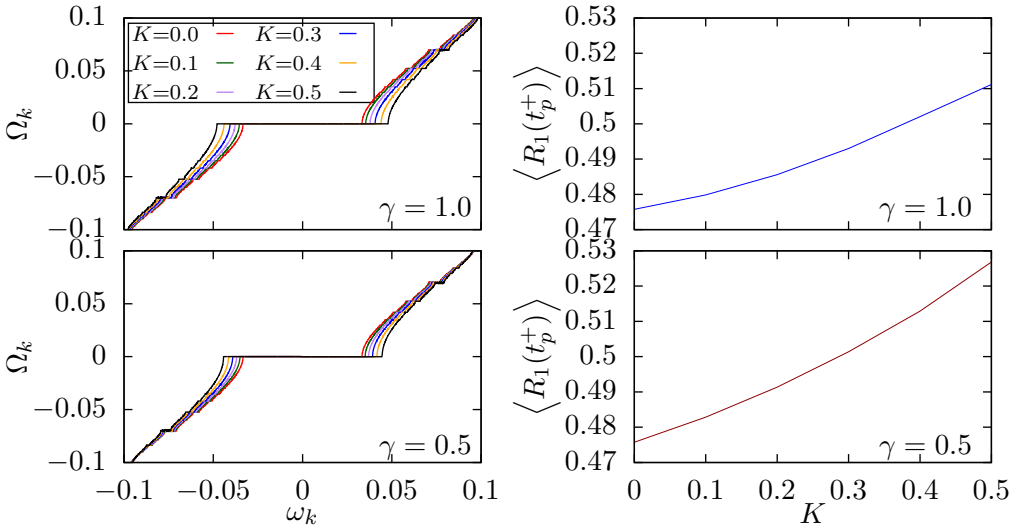

Figure 4.15: The system (4.1) with $N = 5 \cdot 10^4$, varying coupling strength K, and $\gamma \in \{0.5, 1.0\}$ is stimulated with (4.4) h_1, $(\alpha, \varepsilon) = (1, 1)$. The system is initialized for each pair (K, γ) with independent random uniform initial conditions, and an initial transient of 10^4 time units is disregarded. On the left, $\Omega_k(\omega_k)$ around $\omega_k = 0$ is shown for different coupling strength values. On the right, one finds the averaged pulse magnitudes $\langle R_1(t_p^+)\rangle$ in dependence of K.

computational efforts, the step size is increased to $h = 0.1$ and the number of oscillators is $N = 5 \cdot 10^4$. The system is set to random independent uniform initial conditions for each simulation, which, as shown in Fig. 4.13, already has a large impact on the response to the stimulation. For the natural frequencies, a fixed realization is drawn from a uniform distribution $\mathcal{U}(-1, 1)$ and taken for all simulations.

We study the impact of coupling strength K and the balancing factor γ on the average magnitude of the stimulated pulses $\langle R_1(t_p^+)\rangle$. In each simulation an initial transient of 10^4 time units is disregarded, which corresponds to a total 333 stimuli for $\tau = 30$. Afterwards, the simulation of the system is continued for at least another $5 \cdot 10^4$ time units, where the effective frequencies $\Omega_k(\omega_k)$ (3.12) and the averaged pulse heights $\langle R_1(t_p^+)\rangle$ are obtained.

System (4.1) for different K and $\gamma \in \{0.5, 1.0\}$ is stimulated by h_1 with $(\alpha, \varepsilon) = (1.0, 1.0)$. A close-up on the effective frequencies $\Omega_k(\omega_k)$ around $\omega_k = 0$ and the averaged pulse heights $\langle R_1(t_p^+)\rangle$ are presented in Fig. 4.15. For both balancing values $\gamma \in \{0.5, 1.0\}$, one observes an increase in the average pulse heights $\langle R_1(t_p^+)\rangle$ with increasing coupling strength K that is also reflected in the growth of the locking plateaus in $\Omega_k(\omega_k)$.

For the stimulus types (4.4) h_1 with $(\alpha, \varepsilon) = (0.7, 1.0)$ and (4.5) h_2 with

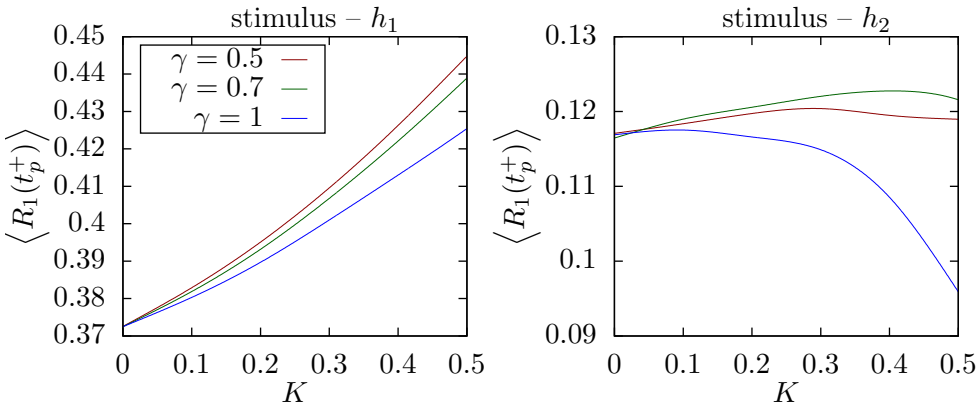

Figure 4.16: The system (4.1) with $N = 5 \cdot 10^4$, varying coupling strength K, and $\gamma \in \{0.5, 0.7, 1.0\}$ is stimulated with (4.4) h_1, $(\alpha, \varepsilon) = (0.7, 1)$ (left) and (4.5) h_2, $\rho = \pi/8$ (right). The system is initialized for each pair (K, γ) with independent random uniform initial conditions, and an initial transient of 10^4 time units is disregarded. The averaged pulse magnitudes $\langle R_1(t_p^+)\rangle$ are presented in dependence on K.

$\rho = \pi/8$, the numerical experiment is performed for $\gamma \in \{0.5, 0.7, 1.0\}$. The recorded averaged pulse heights $\langle R_1(t_p^+)\rangle$ are shown in Fig. 4.16. For both stimulus types, the pulsation becomes stronger when the second harmonic interaction is included $\gamma < 1$. The large difference in the magnitudes between the cases h_1 and h_2 is due to the large amplitude $\varepsilon = 1$. Especially for h_2 it should be noted that early on ($K > 0.1$), the magnitude of the stimulated pulsation starts to decline for $\gamma = 1$. This indicates that the second harmonic coupling which already plays a crucial role for self-organized mode locking significantly influences the appearance of stimulated mode-locked solutions.

5

Discussion

"We can only see a short distance ahead, but we can see plenty there that needs to be done."

– Alan Turing, *Computing machinery and intelligence*

Inspired by the field of laser physics, a new type of collective behavior showing sharp pulses in the coherence radius $R_1(t)$ in systems of globally coupled phase oscillators (3.1) has been discovered and classified. Analogous to optical pulses that typically exhibit extreme peak intensities, the pulses of mode-locked phase oscillators exceed the coherence values at the onset of collective synchronization.

It is found that self-organization is facilitated by the presence of a second harmonic coupling term, which is a minimal extension to the coupling in the Kuramoto model. In the Kuramoto, model mode-locked solutions and phase turbulence are found to be coexisting.

The prototypical mode-locked solution (3.17) presented reveales general features of mode locking such as the suppression of fluctuations between pulses in $R_1(t)$ and the appearance of a distinct maximum in $R_2(t)$ following half a period after each pulse. From this perspective, it is the natural first step to extend the interaction function by a second harmonic in order to support the mode-locking phenomenon. The interesting question whether mode-locked solutions with $K > 0$ are connected to the prototype presented at $K = 0$ was not confirmed. Various types of mode-locked solutions have been classified as harmonic or subharmonic by comparing the structure of the effective frequencies. The given definitions can be used as a starting point to classify mode-locked solutions in similar systems.

To gain insight into the local stability properties of the solutions, a comparison of the rates of expansion of phase space volume around different mode-locked solutions (3.30) is presented, revealing that the second harmonic

indeed gives an additional contration along the orbit. The primary mechanism that stabilizes the mode-locked solutions is identified as the episode of strong contraction during the pulses in $R_1(t)$. Especially, it should be noted that for the Kuramoto-type coupling there is a strict expansion of phase space volumes between the pulses, which means that perturbations are growing. An interesting question that is related to the field of oscillator networks is to what extent non-locally coupled systems can exhibit mode locking. It is a natural assumption that mode locking will persist in almost completely connected networks. A viable suggestion to approach this problem is to remove a fraction of the connection between oscillators at random until the mode locking breaks down.

The stability issues that appeared during the parameter scans for the system with Kuramoto-type coupling led to a small extension of the protocol for performing parameter scans, which bears the conceptual difference that the parameter perturbations are not applied at a specific time, but distributed along the trajectory. The approach is recommendable, especially for solutions with complicated stability properties such as the mode-locked solutions and in cases where parameter perturbations induce switchings between multistable states.

The classification of the transients as type-II supertransients, cf. Fig. 3.27, suggests that in the development of mode locking the solutions remains extremly complex until a suitable configuration in phase space is reached whereupon the pulsation quickly grows and saturates. The exponential growth of the average transient times with increasing system size (3.37) is also in agreement with this assessment. Interestingly, the average transient times are also found to be strongly influenced by the relative strength of the second harmonic, which is marked by the impairment of the self-organizing mechanism without the second harmonic $\gamma = 1$. Note that by including even higher harmonics in the interaction, the average transient times can be further reduced, which has been tested but not studied in more detail.

The loss of stability of mode-locked solutions is found to be accompanied by intermittency creating a bursting behavior in $R_1(t)$, as the solution switches between mode locking and phase turbulence. The scaling of the intermittent behavior depends in particular on the properties of the unstable mode-locked solution, thus one will usually find different exponents to the power law (3.35) in different parameter regimes. Although unstable mode-locked solutions most likely exist for the system with Kuramoto-type coupling, intermittency is not observed, since typically trajectories do not make close enough approaches to the mode-locked solution after phase turbulence has appeared.

In the vicinity of the stability boundaries of mode-locked solutions, low-

dimensional chaotic attractors are found on which the system maintains pulses in $R_1(t)$ while exhibiting a jittering of the inter-pulse intervals and heights. The exact recurrent phase relationship is destroyed as a result, but there is a trapping of the recurrent phase relationship in a certain region in phase space.

The investigation of randomly perturbed equidistant natural frequencies (3.38) showed that mode locking can persist under small quenched disorder, where it is also shown that the smallness can be quantified in terms of the distance to the set of equidistant frequency combs (3.39). The most important result that is indicated by the approach is that generic randomly chosen realizations of uniformly distributed frequencies are unlikely to be able to achieve mode locking. An interesting direction for furhter reseach is the stabilization of mode-locked solutions for detuned frequency combs by pulsed periodic stimulation. The way devised to search for mode-locked solutions is helpful in investigating networks of oscillators below the synchronization threshold regarding possible periodic solution or chaotic attractors that are otherwise difficult to find due to exponentially growing average transient times.

For systematically perturbed frequency combs (3.49), two different breakdown scenarios were discovered, showing a gradual degradation of mode locking for the compressed natural frequencies where the effective frequencies readjust to different subharmonic combs multiple times, and the other exhibiting an instantaneous complete breakdown for attenuated natural frequencies.

Mode locking is found to appear in large ensembles with a suitable multimodal structure in the natural frequencies (3.50). The dynamics of the order parameters for such systems (3.51) closely resemble what has been obtained for (3.1) and other features, such as the average transient time scaling that can be transfered immediately.

The self-organization of mode locking in the large ensembles follows upon the inner-modal synchronization. The introduced modal order parameters further reveal an interesting breathing behavior during the pulses.

For increasing spectral broadening Q in (3.50), the breakdown of mode locking follows as expected, and a mechanism causing a period-two modulation prior to the breakdown has been discovered. The intuitive explanation of which is that with the increased Q, oscillators start to unlock from their respective modes and are drifting. The pulsed solution acts as a forcing that stimulates the drifting oscillators, a small fraction of which again locks to a frequency comb with spacing $\Delta\Omega$ that is shifted by $\Delta\Omega/2$. The formation of the secondary comb in the example is facilitated to a large extent by the second harmonic coupling. This appears as a general mechanism for how the modulation of mode-locked solutions occurs in large ensembles.

The second harmonic coupling is again essential for self-organized mode locking such that without the second harmonic, mode-locked solutions were only found for suitable initial conditions. Unfortunately, the Ott-Antonsen ansatz cannot be applied to the system including the second harmonic, which drastically minimizes the toolbox available to studying the continuum limit. For a multimodal system with first harmonic coupling, the Ott-Antonsen ansatz in principle works such that one can obtain mode-locked solutions by following the procedure described for preparing the initial conditions. For improperly chosen initial conditions, however, one typically encounters modal turbulence, cf. Fig. 3.43.

The last chapter is concerned with coherence echoes and their relation to mode-locked solutions. The coherence echo phenomenon is attributed to the presence of a partially mode-locked state that is being formed through the application of at least two successive stimuli to a large population of oscillators with randomly chosen natural frequencies. Partial in this case refers to the fact that not all oscillators with frequencies matching those of the stimulated comb are locked. In the case of small stimuli, one might want to disregard the nonlinear effects completely as they are in [34]. In the mode-locking picture, the recurrence time between echoes is understood in a natural way as the inverse of the mode spacing of the stimulated mode-locked comb.

For the studied synthetic mode-locked initial state Def. 5, it is shown that the magnitude of the echoes behave in a non-monotonous fashion and that the interaction exerts a strong impact on the echoes with respect to the coupling strength and the second harmonic contribution. The non-monotonic behavior of the magnitude of the coherence echoes can be found for the partially mode-locked states formed by two stimuli, cf. Fig. 4.4. While the basic echo phenomenon and the non-monotonous behavior of the magnitude of the echoes can be explained on a linear level, it is also clear that for a fully mode-locked initial condition like Def. 5, the nonlinear coupling becomes more significant due to the magnitude of $R_1(0)$.

It is demonstrated that by applying a pulsed periodic stimulation to the ensembles of phase oscillators, the partially mode-locked state that is accessed by two consecutive stimuli gradually develops until a fully-locked mode comb is formed. The formation of the fully-locked mode comb is indepedent of the stimulus type, however, the precise parameters can have a great impact on the stimulated pulsed solution. It is shown that in the zero coupling limit, where the evolution for each oscillator can be reduced to a circle map, complex structures in the effective frequencies arise through stimulation. While the effective frequencies developed are independent of the initial conditions, it is clearly shown that the collective response $R_1(p\tau^+)$ varies extremely for dif-

ferent initial conditions. Here, it is especially noteworthy that stimulation of identical initial conditions results in a significant increase of the fluctuations of $R_1(p\tau^+)$ as compared to the stimulation of uniform initial conditions.

Including the global interaction as well ($K > 0$), increases the magnitude of the stimulated pulses, which directly relates to a growth of the locking plateaus. Besides the impact of the global coupling in general, it was also found that the second harmonic $\gamma < 1$ significantly increases the strength of the stimulated pulsed solutions.

The general question that stands behind mode locking is, how a large number of oscillators has to interact in order to form and sustain a recurrent phase relationship conforming to a momentary high coherence measure. Inspired by the dynamics of mode-locked lasers, global coupling schemes were chosen and found to be suitable to accomplish this task. The discovery of mode locking as a collective phenomenon in the general setup of globally-coupled phase oscillators with Kuramoto or Kuramoto-Daido type coupling gives a new perspective on the dynamics of coupled phase oscillators below the synchronization threshold $K < K_C$. The generality of the investigated phase oscillator models indicates that the phenomenon is accessible in a wide range of systems that feature a global interaction scheme and sufficiently-structured natural frequencies.

Bibliography

[1] Yoshiki Kuramoto. *Chemical Oscillations, Waves, and Turbulence*. Springer Series in Synergetics. Springer Berlin Heidelberg, 1984.

[2] Claude Baesens, John Guckenheimer, Seunghwan Kim, and Robert S. MacKay. Three coupled oscillators: mode-locking, global bifurcations and toroidal chaos. *Physica D: Nonlinear Phenomena*, 49(3):387–475, 1991.

[3] Edward Ott, John H. Platig, Thomas M. Antonsen, and Michelle Girvan. Echo phenomena in large systems of coupled oscillators. *Chaos: An Interdisciplinary Journal of Nonlinear Science*, 18(3):037115, 2008.

[4] Hiroaki Daido. Onset of cooperative entrainment in limit-cycle oscillators with uniform all-to-all interactions: bifurcation of the order function. *Physica D: Nonlinear Phenomena*, 91(1):24–66, 1996.

[5] Celso Grebogi, Edward Ott, and James A. Yorke. Fractal Basin Boundaries, Long-Lived Chaotic Transients, And Unstable-Unstable Pair Bifurcation. *Phys. Rev. Lett.*, 51:942–942, Sep 1983.

[6] John Buck. Synchronous rhythmic flashing of fireflies. II. *The Quarterly review of biology*, 63(3):265–289, 1988.

[7] Steven H. Strogatz, Daniel M. Abrams, Allan McRobie, Bruno Eckhardt, and Edward Ott. Theoretical mechanics: Crowd synchrony on the Millennium Bridge. *Nature*, 438(7064):43, 2005.

[8] Kurt Wiesenfeld and James W. Swift. Averaged equations for Josephson junction series arrays. *Phys. Rev. E*, 51:1020–1025, Feb 1995.

[9] Giovanni Filatrella, Arne Hejde Nielsen, and Niels Falsig Pedersen. Analysis of a power grid using a Kuramoto-like model. *The European Physical Journal B*, 61(4):485–491, Feb 2008.

[10] Y. Henry Wen, Michael R. E. Lamont, Steven H. Strogatz, and Alexander L. Gaeta. Self-organization in Kerr-cavity-soliton formation in parametric frequency combs. *Physical Review A*, 94(6):063843, 2016.

[11] Robert Adler. A Study of Locking Phenomena in Oscillators. *Proceedings of the IRE*, 34(6):351–357, June 1946.

[12] Arkady Pikovsky, Michael Rosenblum, Jurgen Kurths, and Jürgen Kurths. *Synchronization: a universal concept in nonlinear sciences*, volume 12. Cambridge university press, 2003.

[13] Michele Bonnin, Fernando Corinto, and Marco Gilli. Phase model reduction and synchronization of periodically forced nonlinear oscillators. *Journal of Circuits, Systems, and Computers*, 19(04):749–762, 2010.

[14] J. Guckenheimer. Isochrons and phaseless sets. *Journal of Mathematical Biology*, 1(3):259–273, Sep 1975.

[15] G. Bard Ermentrout and David H. Terman. *Mathematical foundations of neuroscience*, volume 35. Springer Science & Business Media, 2010.

[16] Hiroya Nakao. Phase reduction approach to synchronisation of nonlinear oscillators. *Contemporary Physics*, 57(2):188–214, 2016.

[17] John Guckenheimer and Philip Holmes. *Nonlinear Oscillations, Dynamical Systems and Bifurcatio of Vector Fields*. Springer, 1983.

[18] Steven H. Strogatz. From Kuramoto to Crawford: exploring the onset of synchronization in populations of coupled oscillators. *Physica D: Nonlinear Phenomena*, 143(1):1 – 20, 2000.

[19] Juan A. Acebrón, Luis L. Bonilla, Conrad J. Pérez Vicente, Félix Ritort, and Renato Spigler. The Kuramoto model: A simple paradigm for synchronization phenomena. *Reviews of modern physics*, 77(1):137, 2005.

[20] David Hansel, German Mato, and Claude Meunier. Clustering and slow switching in globally coupled phase oscillators. *Phys. Rev. E*, 48:3470–3477, Nov 1993.

[21] David Hansel, German Mato, and Claude Meunier. Phase dynamics for weakly coupled hodgkin-huxley neurons. *EPL (Europhysics Letters)*, 23(5):367, 1993.

[22] Maxim Komarov and Arkady Pikovsky. Multiplicity of Singular Synchronous States in the Kuramoto Model of Coupled Oscillators. *Phys. Rev. Lett.*, 111:204101, Nov 2013.

[23] Oleksandr V. Popovych, Yuri L. Maistrenko, and Peter A. Tass. Phase chaos in coupled oscillators. *Phys. Rev. E*, 71:065201, Jun 2005.

[24] Yuri Maistrenko, Oleksandr Popovych, Oleksandr Burylko, and Peter A. Tass. Mechanism of desynchronization in the finite-dimensional Kuramoto model. *Physical review letters*, 93(8):084102, 2004.

[25] Diego Pazó. Thermodynamic limit of the first-order phase transition in the Kuramoto model. *Phys. Rev. E*, 72:046211, Oct 2005.

[26] Hayato Chiba. A proof of the Kuramoto conjecture for a bifurcation structure of the infinite-dimensional Kuramoto model. *Ergodic Theory and Dynamical Systems*, 35(3):762–834, 2015.

[27] Helge Dietert. Stability and bifurcation for the Kuramoto model. *Journal de Mathématiques Pures et Appliquées*, 105(4):451–489, 2016.

[28] Salvatore Torquato. Hyperuniformity and its generalizations. *Phys. Rev. E*, 94:022122, Aug 2016.

[29] Leon Glass and Jiong Sun. Periodic forcing of a limit-cycle oscillator: Fixed points, Arnold tongues, and the global organization of bifurcations. *Phys. Rev. E*, 50:5077–5084, Dec 1994.

[30] Anatole Katok and Boris Hasselblatt. *Introduction to the modern theory of dynamical systems*, volume 54. Cambridge university press, 1997.

[31] Kunihiko Kaneko. Globally coupled circle maps. *Physica D: Nonlinear Phenomena*, 54(1):5 –19, 1991.

[32] Yoshiki Kuramoto and Dorjsuren Battogtokh. Coexistence of Coherence and Incoherence in Nonlocally Coupled Phase Oscillators. *Nonlinear Phenomena in Complex Systems*, 5(4):380–385, 2002.

[33] Daniel M. Abrams and Steven H. Strogatz. Chimera States for Coupled Oscillators. *Phys. Rev. Lett.*, 93:174102, Oct 2004.

[34] Tianran Chen, Mark R. Tinsley, Edward Ott, and Kenneth Showalter. Echo Behavior in Large Populations of Chemical Oscillators. *Phys. Rev. X*, 6:041054, Dec 2016.

[35] Edward Ott. Relativistic synchrontron plasma echo. *Journal of Plasma Physics*, 4(3):471–476, 1970.

[36] Boris B. Kadomtsev. Landau damping and echo in a plasma. *Soviet Physics Uspekhi*, 11(3):328, 1968.

[37] Erwin L. Hahn. Spin Echoes. *Phys. Rev.*, 80:580–594, Nov 1950.

[38] Conrad Sanderson and Ryan Curtin. Armadillo: a template-based C++ library for linear algebra. *Journal of Open Source Software, Vol. 1, pp. 26*, 2016.

[39] Boost. Boost C++ Libraries. `http://www.boost.org/`, 2018. Last accessed 2018-05-28.

[40] Leonardo Dagum and Ramesh Menon. Openmp: An industry-standard api for shared-memory programming. *IEEE Comput. Sci. Eng.*, 5(1):46–55, January 1998.

[41] Peter Deuflhard and Folkmar Bornemann. *Gewöhnliche Differentialgleichungen*. Walter de Gruyter, 2013.

[42] Arkady Pikovsky, Oleksandr Popovych, and Yuri Maistrenko. Resolving Clusters in Chaotic Ensembles of Globally Coupled Identical Oscillators. *Phys. Rev. Lett.*, 87:044102, Jul 2001.

[43] Michel Hénon. On the numerical computation of Poincaré maps. *Physica D: Nonlinear Phenomena*, 5(2):412–414, 1982.

[44] Warwick Tucker. Computing accurate Poincaré maps. *Physica D: Nonlinear Phenomena*, 171(3):127–137, 2002.

[45] Yuri A. Kuznetsov. *Elements of Applied Bifurcation Theory*. Applied Mathematical Sciences. Springer New York, 2013.

[46] Eusebius J. Doedel and Bart Oldeman. AUTO07P: Continuation and Bifurcation Software for Ordinary Differential Equations. 01 2009.

[47] Koen Engelborghs, Tatyana Luzyanina, and Giovanni Samaey. DDE-BIFTOOL v. 2.00: a Matlab package for bifurcation analysis of delay differential equations. 2001.

[48] Koen Engelborghs, Tatyana Luzyanina, and Dirk Roose. Numerical bifurcation analysis of delay differential equations using DDE-BIFTOOL. *ACM Transactions on Mathematical Software (TOMS)*, 28(1):1–21, 2002.

[49] Jan Sieber, Koen Engelborghs, Tatyana Luzyanina, Giovanni Samaey, and Dirk Roose. DDE-BIFTOOL Manual-Bifurcation analysis of delay differential equations. *arXiv preprint arXiv:1406.7144*, 2014.

[50] Valery Iustinovich Oseledets. A multiplicative ergodic theorem. Characteristic Ljapunov, exponents of dynamical systems. *Trudy Moskovskogo Matematicheskogo Obshchestva*, 19:179–210, 1968.

[51] David Ruelle. Ergodic theory of differentiable dynamical systems. *Publications Mathématiques de l'Institut des Hautes Études Scientifiques*, 50(1):27–58, 1979.

[52] Arkady Pikovsky and Antonio Politi. *Lyapunov Exponents: A Tool to Explore Complex Dynamics*. Cambridge University Press, 2016.

[53] Tamás Tél and Ying-Cheng Lai. Chaotic transients in spatially extended systems. *Physics Reports*, 460(6):245–275, 2008.

[54] Giancarlo Benettin, Luigi Galgani, and Jean-Marie Strelcyn. Kolmogorov entropy and numerical experiments. *Phys. Rev. A*, 14:2338–2345, Dec 1976.

[55] Marco Sandri. Numerical calculation of Lyapunov exponents. *Mathematica Journal*, 6(3):78–84, 1996.

[56] Isaac Goldhirsch, Pierre-Louis Sulem, and Steven A. Orszag. Stability and Lyapunov stability of dynamical systems: A differential approach and a numerical method. *Physica D: Nonlinear Phenomena*, 27(3):311– – 337, 1987.

[57] Freddy Christiansen and Hans Henrik Rugh. Computing Lyapunov spectra with continuous Gram - Schmidt orthonormalization. *Nonlinearity*, 10(5):1063, 1997.

[58] Hayato Chiba. A Center Manifold Reduction of the Kuramoto–Daido Model with a Phase-Lag. *SIAM Journal on Applied Dynamical Systems*, 16(3):1235–1259, 2017.

[59] Hayato Chiba and Diego Pazó. Stability of an [N/2]-dimensional invariant torus in the Kuramoto model at small coupling. *Physica D: Nonlinear Phenomena*, 238(13):1068 – 1081, 2009.

[60] Sebastian Eydam and Matthias Wolfrum. Mode locking in systems of globally coupled phase oscillators. *Phys. Rev. E*, 96:052205, Nov 2017.

[61] Vladimir Igorevich Arnol'd. *Mathematical methods of classical mechanics*, volume 60. Springer Science & Business Media, 2013.

[62] Paul Frederickson, James L. Kaplan, Ellen D. Yorke, and James A. Yorke. The Liapunov Dimension of Strange Attractors. *Journal of Differential Equations*, 49(2):185–207, 1983.

[63] Jean Pierre Eckmann. Roads to turbulence in dissipative dynamical systems. *Rev. Mod. Phys.*, 53:643–654, Oct 1981.

[64] Yves Pomeau and Paul Manneville. Intermittent transition to turbulence in dissipative dynamical systems. *Comm. Math. Phys.*, 74(2):189–197, 1980.

[65] Hugues Chaté and Paul Manneville. Transition to turbulence via spatio-temporal intermittency. *Phys. Rev. Lett.*, 58:112–115, Jan 1987.

[66] Edward Ott. *Chaos in Dynamical Systems*. Cambridge University Press, 2 edition, 2002.

[67] Holger Kantz and Peter Grassberger. Repellers, semi-attractors, and long-lived chaotic transients. *Physica D: Nonlinear Phenomena*, 17(1):75–86, 1985.

[68] Tamás Tél. The joy of transient chaos. *Chaos*, 25(9), 2015.

[69] Matthias Wolfrum and Oleh E. Omel'chenko. Chimera states are chaotic transients. *Phys. Rev. E*, 84:015201, Jul 2011.

[70] Edward Ott and Thomas M Antonsen. Low dimensional behavior of large systems of globally coupled oscillators. *Chaos: An Interdisciplinary Journal of Nonlinear Science*, 18(3):037113, 2008.

[71] Erik A. Martens, Ernest Barreto, Steven H. Strogatz, Edward Ott, Paul So, and Thomas M. Antonsen. Exact results for the Kuramoto model with a bimodal frequency distribution. *Phys. Rev. E*, 79:026204, Feb 2009.

[72] Bastian Pietras, Nicolás Deschle, and Andreas Daffertshofer. Equivalence of coupled networks and networks with multimodal frequency distributions: Conditions for the bimodal and trimodal case. *Phys. Rev. E*, 94:052211, Nov 2016.

[73] Hermann A. Haus. Theory of mode locking with a fast saturable absorber. *Journal of Applied Physics*, 46(7):3049–3058, 1975.

[74] H. Haus. A theory of forced mode locking. *IEEE Journal of Quantum Electronics*, 11(7):323–330, July 1975.

[75] Franz X. Kurtner, Juerg Aus der Au, and Ursula Keller. Mode-locking with slow and fast saturable absorbers-what's the difference? *IEEE Journal of Selected Topics in Quantum Electronics*, 4(2):159–168, Mar 1998.

[76] Andrei G. Vladimirov and Dmitry Turaev. Model for passive mode locking in semiconductor lasers. *Phys. Rev. A*, 72:033808, Sep 2005.

[77] Peter Moulton. Ti-doped sapphire: tunable solid-state laser. *Optics News*, 8(6):9–9, Nov 1982.

[78] David E. Spence, P. N. Kean, and Wilson Sibbett. 60-fsec pulse generation from a self-mode-locked Ti: sapphire laser. *Optics letters*, 16(1):42–44, 1991.

[79] Luigi A. Lugiato and René Lefever. Spatial Dissipative Structures in Passive Optical Systems. *Physical review letters*, 58(21):2209, 1987.

[80] Pascal Del'Haye, Albert Schliesser, Olivier Arcizet, Tom Wilken, Ronald Holzwarth, and Tobias J. Kippenberg. Optical frequency comb generation from a monolithic microresonator. *Nature*, 450(7173):1214, 2007.

[81] Yanne K. Chembo and Curtis R. Menyuk. Spatiotemporal lugiato-lefever formalism for kerr-comb generation in whispering-gallery-mode resonators. *Phys. Rev. A*, 87:053852, May 2013.

[82] Hossein Taheri, Pascal Del'Haye, Ali A. Eftekhar, Kurt Wiesenfeld, and Ali Adibi. Self-synchronization phenomena in the Lugiato-Lefever equation. *Phys. Rev. A*, 96:013828, Jul 2017.

[83] Michael Chertkov, Ildar Gabitov, and Jamison T. Moeser. Pulse confinement in optical fibers with random dispersion. *Proceedings of the National Academy of Sciences*, 98(25):14208–14211, 2001.

[84] Romain Brette. Rotation numbers of discontinuous orientation-preserving circle maps. *Set-Valued Analysis*, 11(4):359–371, Dec 2003.